ulm university universität ulm

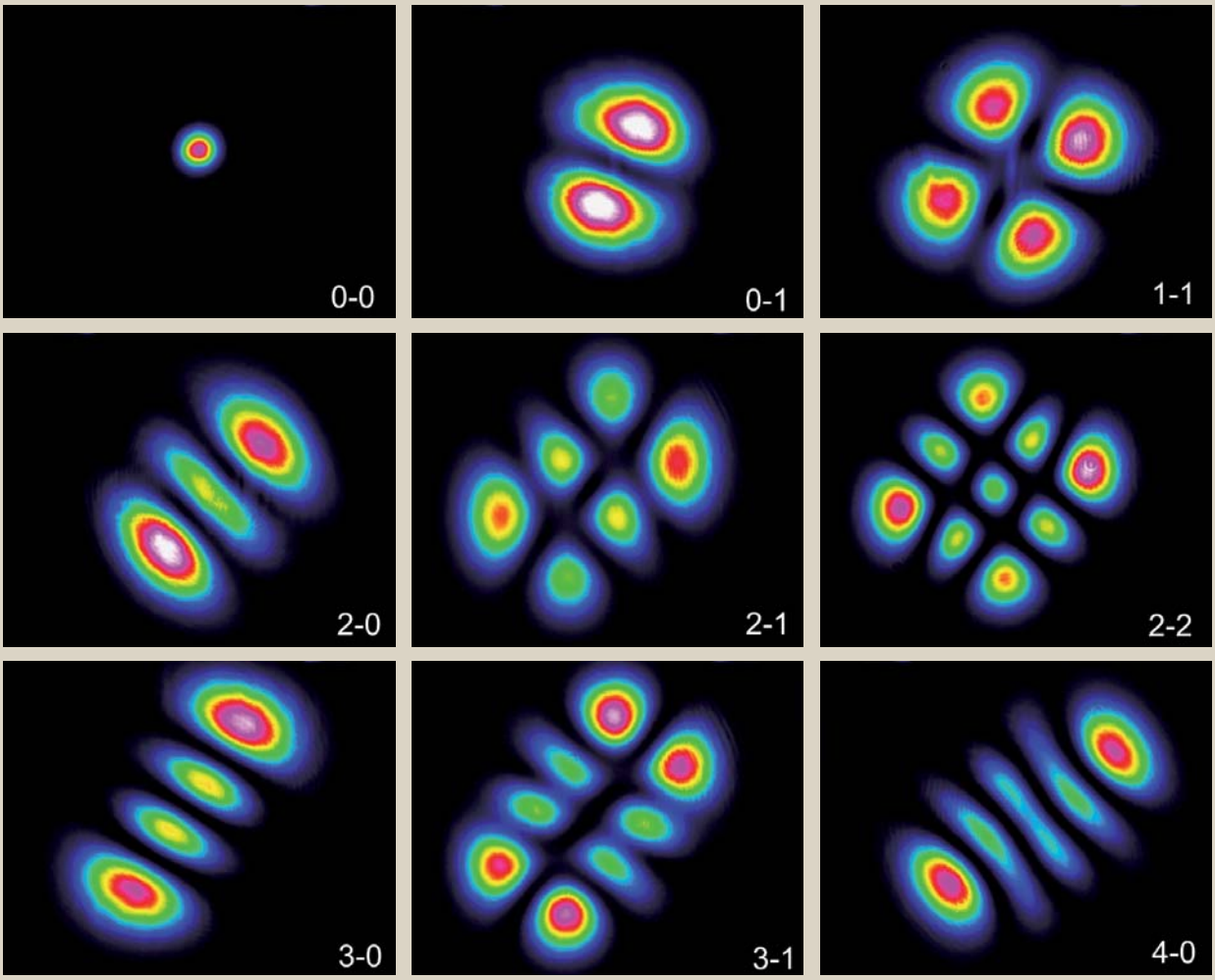

Annual Report 2008

Institute of Optoelectronics

Cover photo:
Transvers optical resonator modes of a semiconductor disk laser (see article on page 41).
The emission beam patterns have been imaged using a high-resolution
CMOS camera at different resonator lengths.
Top row: TEM00 , TEM01 , TEM11 .
Center row: TEM20 , TEM21 , TEM22 .
Bottom row: TEM30 , TEM31 , TEM40 .

Contents

Articles

Lists of Publications

1: Ilona Argut
2: Rainer Blood
3: Stephan Schwaiger
4: Thomas Wunderer
5: Christine Bunk
6: Frank Lipski
7: Ahmed Al-Samaneh
8: Mohamed Fikry
9: Peter Unger
10: Ferdinand Scholz
11: Dietmar Wahl
12: Fernando Rinaldi
13: Ihab Kardosh
14: Frank Demaria
15: Rainer Michalzik
16: Anna Bergmann
17: Rudolf Rösch
18: Alexander Kern
19: Kamran Forghani
20: Abdel-Sattar Gadallah

Missing in the picture:

Karl J. Ebeling, Sükran Kilic, Hildegard Mack, Jürgen Mähnß, Gerlinde Meixner, Susanne Menzel, Wolfgang Schwarz, Josef Theisz, Benedikt Westenfelder, Thomas Wunderer

Institute of Optoelectronics
Ulm University

Albert-Einstein-Allee 45, 89081 Ulm, Germany
URL: http://www-uni-ulm.de/opto
Fax: +49–731/50–2 60 49
Phone: +49–731/50–

Head of Department

Prof. Dr.	Peter Unger	–2 60 54	peter.unger@uni-ulm.de

Deputy Head

Prof. Dr.	Ferdinand Scholz	–2 60 52	ferdinand.scholz@uni-ulm.de

President of Ulm University

Prof. Dr.	Karl Joachim Ebeling	–2 20 00	karljoachim.ebeling@uni-ulm.de

Group Leader

Dr.-Ing. habil.	Rainer Michalzik	–2 60 48	rainer.michalzik@uni-ulm.de

Cleanroom Management

Dr.-Ing.	Jürgen Mähnß	–2 60 53	juergen.maehnss@uni-ulm.de

Secretaries

	Christine Bunk	–2 60 50	christine.bunk@uni-ulm.de
	Sükran Kilic	–2 60 59	suekran.kilic@uni-ulm.de
	Hildegard Mack	–2 60 59	hildegard.mack@uni-ulm.de

Research Staff

M.Sc.	Ahmed Al-Samaneh	–2 60 37	ahmed.al-samaneh@uni-ulm.de
Dipl.-Ing.	Anna Bergmann	–2 60 38	anna.bergmann@uni-ulm.de
Dr.-Ing.	Frank Demaria	–2 60 46	frank.demaria@uni-ulm.de
M.Sc.	Mohamed Fikry	–2 61 95	mohamed.fikry@uni-ulm.de
M.Sc.	Kamran Forghani	–2 60 39	kamran.forghani@uni-ulm.de
M.Sc.	Abdel-Sattar Gadallah	–2 60 43	abdel-sattar.gadallah@uni-ulm.de
Dipl.-Ing.	Joachim Hertkorn*	–2 61 95	joachim.hertkorn@uni-ulm.de
Dipl.-Ing.	Ihab Kardosh	–2 60 35	ihab.kardosh@uni-ulm.de
Dipl.-Ing.	Alexander Kern	–2 60 37	alexander.kern@uni-ulm.de
Dipl.-Ing.	Andrea Kroner*	–2 60 35	andrea.kroner@uni-ulm.de
Dipl.-Phys.	Frank Lipski	–2 60 39	frank.lipski@uni-ulm.de
Dr.-Ing.	Fernando Rinaldi	–2 60 46	fernando.rinaldi@uni-ulm.de
Dipl.-Ing.	Hendrik Roscher*	–2 60 44	hendrik.roscher@uni-ulm.de
Dipl.-Phys.	Stephan Schwaiger	–2 6056	stephan.schwaiger@uni-ulm.de
Dipl.-Ing.	Wolfgang Schwarz	–2 60 38	wolfgang.schwarz@uni-ulm.de
Dr.-Ing.	Georgi Stareev*	–2 64 53	georgi.stareev@uni-ulm.de
Dipl.-Ing.	Sarad Bahadur Thapa*	–2 61 95	sarad.thapa@uni-ulm.de
Dipl.-Phys.	Dietmar Wahl	–2 60 36	dietmar.wahl@uni-ulm.de
Dipl.-Phys.	Benedikt Westenfelder	–2 64 54	benedikt.westenfelder@uni-ulm.de
Dipl.-Ing.	Thomas Wunderer	–2 64 54	thomas.wunderer@uni-ulm.de

Technical Staff

Ilona Argut	–2 60 56	ilona.argut@uni-ulm.de
Rainer Blood	–2 60 44	rainer.blood@uni-ulm.de
Gerlinde Meixner	–2 60 41	gerlinde.meixner@uni-ulm.de
Susanne Menzel	–2 60 41	susanne.menzel@uni-ulm.de
Rudolf Rösch	–2 60 57	rudolf.roesch@uni-ulm.de
Josef Theisz	–2 60 30	josef.theisz@uni-ulm.de

* Member has left the institute meanwhile

Preface

During 2008, the research activities of the Institute of Optoelectronics have been continuing in the areas of optical interconnect systems, vertical-cavity surface-emitting lasers, GaN-based electronic and optoelectronic devices, and high-power optically pumped semiconductor disk lasers.

Current research topics of the VCSELs and Optical Interconnects Group are vertical-cavity lasers with polarization-stable light output, fundamental or higher-order mode selection, one-dimensional and matrix-addressable two-dimensional arrays as well as bidirectional interconnect solutions and optical microparticle trapping for biophotonics. Record-high single-mode powers have been obtained from a monolithic VCSEL with a curved output reflector. For the first time, hybrid integration of VCSEL arrays and microfluidic chips has been demonstrated.

The GaN group has put more and more efforts on the research towards non- and semipolar GaN. Funded by the Deutsche Forschungsgemeinschaft, a transregional research group project could be launched where eight German groups jointly concentrate their efforts for coming closer to a green laser diode based on such materials, co-ordinated by us. Hence, our ongoing work on facet LEDs and the successful fabrication of a polar ultra-violet GaInN laser diode set excellent corner stones for such work. On the other hand, our research now also targets the other spectral direction towards short-wavelength LEDs.

In the High-Power Semiconductor Laser Group, optically pumped semiconductor disk lasers have been further improved. Our devices show the highest absorption efficiencies, conversion efficiencies, and differential quantum efficiencies which have been reported so far.

Five members of the Institute, namely Peter Brückner, Frank Demaria, Barbara Neubert, Fernando Rinaldi, and Daniel Supper received their Ph.D. degrees. Furthermore, four Diploma Theses, six Master Theses, one Bachelor Thesis, and two Semester Projects have been carried out in 2008. In July 2008, Alexander Kern's Diploma Thesis on frequency-doubled semiconductor disk lasers was awarded by the VDI, and Johannes Michael Ostermann received the Dissertation Award of Ulm University for his thesis on surface grating VCSELs. In the same month, Rainer Michalzik had submitted his Habilitation Thesis. The procedure was concluded with a scientific presentation given in Feb. 2009.

Rainer Michalzik
Ferdinand Scholz
Peter Unger

Ulm, March 2009

Investigations of an In-situ Etching Technique of a Sacrificial ZnO Buffer Layer for the Fabrication of Freestanding GaN in Hydride Vapor Phase Epitaxy

Frank Lipski

By in-situ etching of a ZnO buffer layer freestanding GaN layers were prepared by hydride vapor phase epitaxy (HVPE). For the template growth, single crystalline ZnO buffer layers, grown by pulsed laser deposition on sapphire, were used. They were overgrown with a thin GaN layer by a multilayer growth using metal organic vapor phase epitaxy (MOVPE). The removal of the ZnO buffer during the HVPE growth allowed the fabrication of strain-free freestanding GaN layers with a full width-half-maximum of the donor bound exciton (D^0X) of 2.3 meV at a position of 3.47 eV in low temperature (15 K) photoluminescence.

1. Introduction

Unlike other established semiconductor material systems, nowadays GaN technology is based on heteroepitaxy on foreign materials due to missing GaN-substrates. For the fabrication of these demanded substrates, the hydride vapor phase epitaxy (HVPE) is considered as the most promising tool. Nevertheless HVPE growth of GaN is still a heteroepitaxial process, requiring a removal technique of the used substrate from the grown GaN layer. Many approaches towards that challenge were reported in the literature, such as laser-lift-off (LLO) [1], mechanical polishing for substrate removal [2], or growth on etchable substrates. Also good results could be achieved by the use of inserted cavernous interlayers which work as breaking points during cool-down from the growth temperature of about 1050°C [3].

Because the substrate removal is done afterwards, the growth is always carried out under strained conditions due to the lattice mismatch. Additional stress arises from different thermal expansion coefficients of GaN and the substrate while cooling down the sample. Together with the stress introduced by the separation method, this leads to a damage of the GaN layer and also can lead to a high dislocation density and strong bowing depending on the separation method. Also the GaN wafers often break during the substrate removal due to the induced high stress.

In this work we investigate an in-situ separation technique during HVPE growth that allows to avoid thermal stress during cool-down introduced by the mismatch of thermal expansion coefficients and also allows to do the growth on a strain-free quasi-substrate [4]. Therefore, we use a sacrificial interlayer made of ZnO that can be easily etched in the HVPE process. Because of its similar material properties compared to GaN, ZnO is the ideal candidate for that purpose. Especially the small lattice mismatch of only about 1.9%

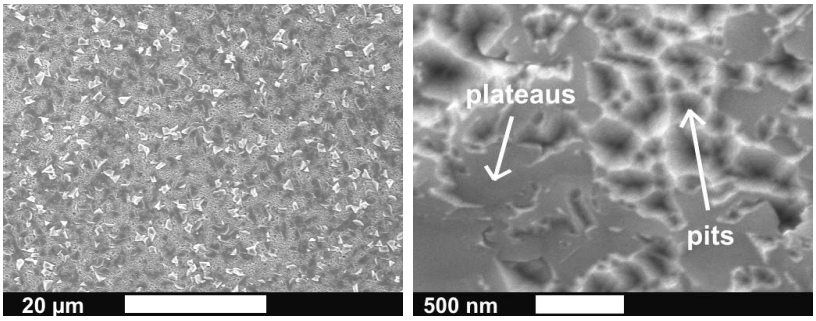

Fig. 1: SEM images of the template surface with several small crystallites (left). In higher magnification (right) a large number of pits and formed plateaus are visible.

and the fact that ZnO can be easily etched makes it very attractive. However, the extreme instability of ZnO in the HVPE atmosphere demands a protecting cover layer of GaN before growth. While other groups have successfully deposited GaN on ZnO by molecular beam epitaxy [5], we employ metal organic vapor phase epitaxy (MOVPE) as commonly used in GaN technology. The created templates can be successfully overgrown by HVPE and the ZnO buffer is removed in-situ, resulting in a free standing quasi substrate avoiding any strain from a lattice-mismatch or stress during cool-down due to a difference in thermal expansion coefficients.

2. Experimental

The templates prepared for the HVPE growth consisted of an approx. 600 nm thick ZnO layer on sapphire, grown by pulsed laser deposition as described elsewhere [6]. The samples were subsequently overgrown with a thin GaN cover layer by a multistep procedure in an AIXTRON AIX 200 RF low pressure (LP)-MOVPE system by using trimethylgallium (TMGa) and NH_3 as precursors. First, a low temperature cover layer was grown at fairly low temperature of 550°C using N_2 as carrier gas in order to protect ZnO from etching at the onset of the growth process. Afterwards, an intermediate layer at 800°C was grown to minimize the diffusion of Zn and O_2 into the finally grown top layer which was deposited at a temperature of 900°C. For this final layer and the intermediate layer H_2 and N_2 were used as carrier gas. In between these layers, different annealing steps were performed, while the pressure was kept constant at 100 mbar during the complete MOVPE process [7].

The HVPE growth was performed in a commercial Aixtron single-wafer HVPE system with a horizontal quartz-tube, heated in a furnace with five zones. Nitrogen and hydrogen were used as carrier gas. As nitrogen precursor, ammonia was applied, while for the group-III element GaCl was used, formed inside the reactor by streaming HCl-gas over a liquid Ga source heated to 850°C. For the growth a three step procedure was developed. The goal of the first step was the formation of a GaN layer, stable enough that it can act as a freestanding quasi substrate for the subsequent growth after the in-situ lift-off. In this step dissolving of the ZnO must be prevented before the GaN-layer is stable enough.

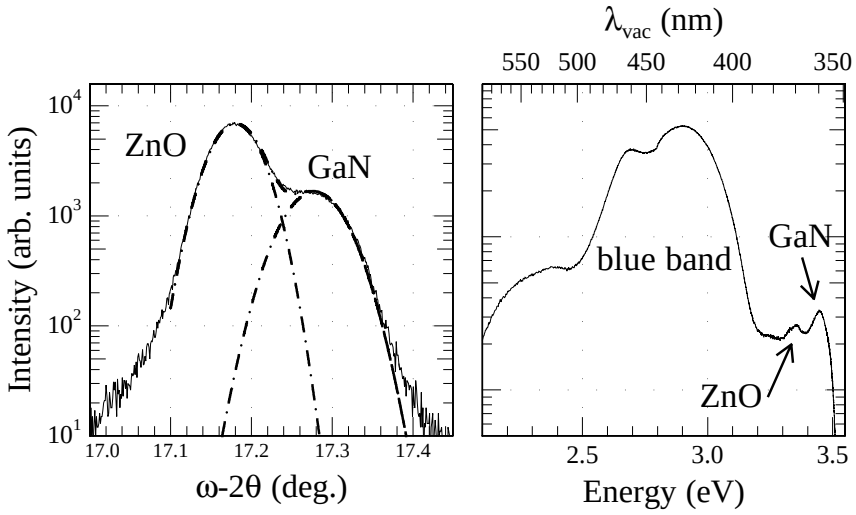

Fig. 2: MOVPE grown template: ω-2θ-scan of (0002)-reflection of HRXRD measurement (left). GaN and ZnO peak can clearly be distinguished. In the LT-PL spectrum (15 K) ZnO and GaN-peaks are visible (right).

In a second step, the etching of the sacrificial ZnO buffer was performed, while the growth rate was drastically decreased or even stopped. By increasing the hydrogen concentration of the carrier gas while slowly increasing temperature, the ZnO was completely etched. This is the most critical part of the process, since high temperature is inevitable to accelerate the etching, but is precarious as it introduces thermal stress to the sample because the thermal expansion coefficients of sapphire, ZnO and GaN are strongly different [1]. Finally a separated free-standing GaN layer is prepared for the final high-temperature growth.

After the lift-off, a thick high-temperature (HT) layer of several hundred µm was grown in the last step at optimized growth conditions [8]. Therefore, a temperature of 1050°C and a pressure of 900 mbar were chosen and the growth rate was adjusted to be about 150 µm/h.

Scanning electron microscopy (SEM) and high resolution X-ray diffraction (HRXRD) measurements were carried out to investigate surface morphology and crystal quality. The optical properties were investigated by low temperature (15 K) photoluminescence (PL) and high resolution cathodoluminescence (CL) spectroscopy.

3. Results and Discussion

3.1 MOVPE growth

The total thickness of the GaN layer grown in MOVPE was approximately 600 nm. The samples showed a light yellow color and on the surface still many pits and defects could be detected. However, the emergence of large areas of plateau-like flat surface indicates the 2D-growth of GaN. Figure 1 shows SEM pictures of the surface. The formation of

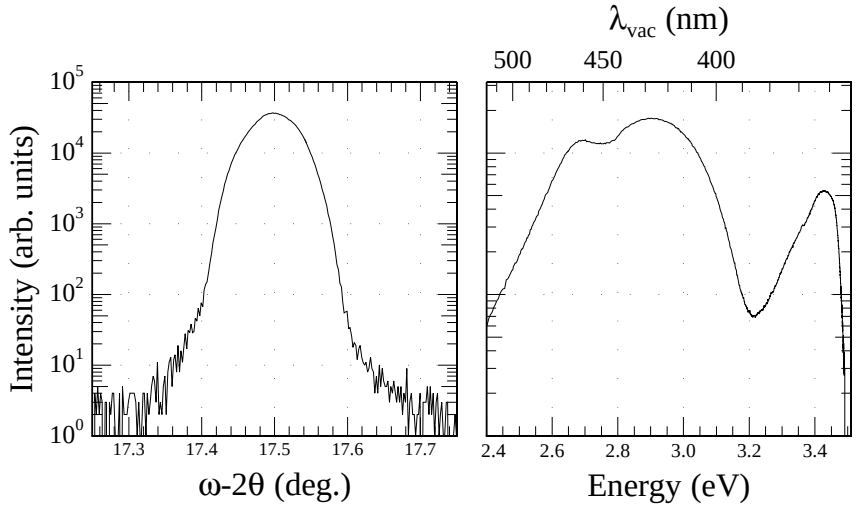

Fig. 3: The ω-2θ scan of (0002)-reflection in HRXRD- (left) and the LT-PL- (right) measurement shows the comparably low quality of the grown LT-layer in the first HVPE step. Compared to the used template, the GaN peak shows a drastically increased intensity.

small crystallites on the surface could not be completely avoided, but the density could be reduced to less than $10^7\,\mathrm{cm}^{-2}$.

The quality of the GaN layer was investigated by PL and HRXRD measurements. In the LT-PL spectrum (Fig. 2) a clear signal from the GaN at 3.44 eV could be detected, as well as a peak related to ZnO at 3.34 eV. The broad luminescence band at around 2.9 eV is typical for Zn doped GaN [9], probably a result of gas phase diffusion during growth. Also in Fig. 2 a ω-2θ-scan of the (0002)-reflection is shown. The two peaks related to ZnO and GaN can be clearly distinguished, confirming the well-ordered c-plane crystalline growth of the GaN layer on the ZnO film. More details can be found elsewhere [7, 10].

3.2 HVPE growth

In the first HVPE step, an approximately 50 µm thick GaN layer was deposited. The choice of growth parameters for this step is demanding, because etching of the ZnO must be reduced to a minimum, until a stable GaN layer is achieved. We found, that at temperatures above 900°C the ZnO layer is already completely dissolved during this first step. The ZnO is also etched, if hydrogen is present in the reactor during this LT growth. At 900°C and without H_2 in the carrier gas, a closed uncracked GaN layer of 50 µm thickness could be grown on the ZnO-GaN template. The quality of this layer is still comparably low due to the low growth temperature. So HRXRD measurements showed a full width at half maximum (FWHM) of the (0002)-reflection of about 1400 arcsec, and the PL-spectrum is still dominated by the blue luminescence band around 2.9 eV (Fig. 3). Moreover the surface is very rough after this step (Fig. 4).

After the LT layer, the growth is interrupted and the temperature is increased to 950°C to achieve a stronger dissolution of the ZnO. The moderate temperature ramp was necessary,

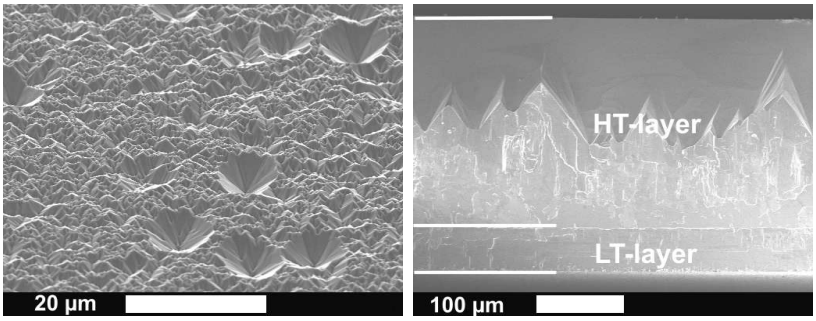

Fig. 4: The SEM picture of the LT HVPE layer shows a very rough surface (left). In the cross-section (right) the LT layer can be clearly identified. The strong contrast in the SEM picture is probably attributed to ZnO incorporation.

otherwise the ZnO dissolved too fast, resulting in many holes and cracks of the GaN layer. By adding hydrogen to the carrier gas and increasing the ammonia flow, the etching of the ZnO, starting at the sample edges, is encouraged. It also causes the formation of channels to allow the dissolved ZnO to escape (Fig. 5). The LT layer is separated from the sapphire during this step, remaining as a freestanding quasi substrate on top of the sapphire.

Finally, the temperature is further increased to 1050°C for the growth of an approximately 250 µm thick HT-layer of higher quality. Obviously, first a highly defective layer grows, probably due to some disturbance of the low temperature layer having lower quality. Additionally, we suppose that last traces of ZnO are removed during this step leading to high Zn doping which may be responsible for the brownish color of our samples. After about 150 µm growth, an abrupt change of contrast is visible in the cross section SEM picture (Fig. 4) indicating a much lower defect density in the top part of this layer. This abrupt change from defective material to good layer quality may also explain the strong bowing of our samples which has still to be reduced and currently limits their total thickness. Also the areal size of the final samples is currently limited by crack formation to about one cm^2.

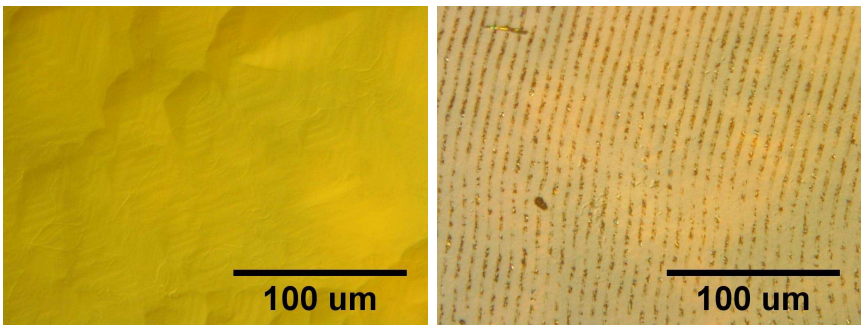

Fig. 5: Optical microscope images of the smooth surface (left) and backside (right) of the final sample. On the backside the formed channels of the dissolving ZnO are clearly visible.

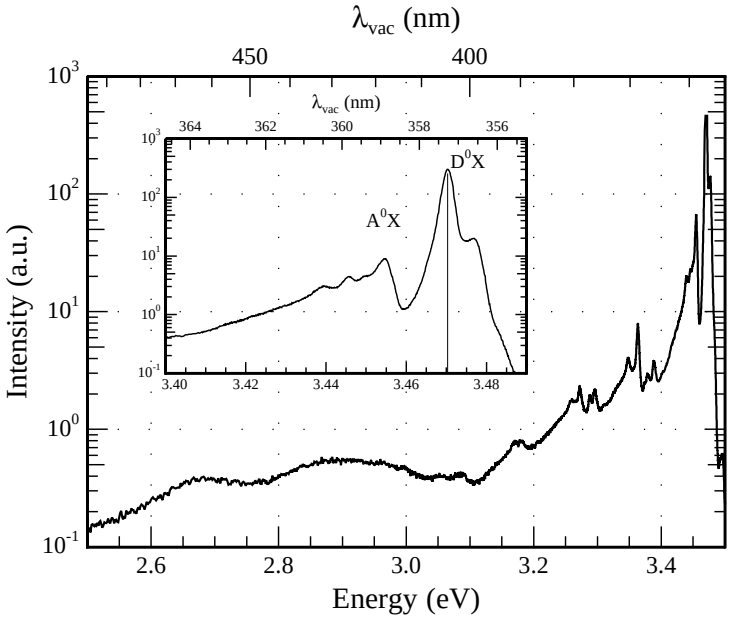

Fig. 6: Photoluminescence spectrum (15K) of the HT-GaN layer (300 µm) on top of the sample. Position of D^0X at 3.470 eV indicates a strain-free surface. The spectrum also shows an intense peak of an acceptor-bound-exciton at 3.455 eV related to Zn-incorporation. Strong phonon replica of both peaks are visible.

By low temperature (7 K) CL measurement along the cross-section (Fig. 7) we analyzed the strain situation in the samples. The first 50µm of the LT layer were grown under tensile strain due to the lattice mismatch of GaN and ZnO, what could be responsible for a shift to lower energies of the D^0X. Only the lowest regions were relaxed by the formation of some micro-cracks. After the removal of the ZnO-buffer the first HT-GaN layers were grown under compressive strain, due to the concave bowing of the sample. With increasing thickness and less incorporation of Zn, the top layers are more and more strain free.

A low-temperature (15 K) PL-spectrum of the top of the final free-standing sample with about 300 µm HT-GaN is shown in Fig. 6. The position of the donor bound exciton (D^0X) at 3.470 eV indicates a strain-free surface. The FWHM of 2.3 meV for the D^0X is still high compared to GaN on sapphire, but very narrow for GaN on ZnO. Beside the D^0X, a strong peak of an acceptor-bound exciton at 3.455 eV with strong phonon replica can be found and is related to Zn doping. A localization energy of 22 meV with respect to the free A exciton at 3.477 eV was obtained for this A^0X.

4. Summary

We successfully have overgrown a ZnO-buffer layer with GaN by MOVPE and a subsequent HVPE step. The fabrication of freestanding GaN by an in-situ etching technique in HVPE could be realised, while the lift-off occured already during growth. Unfortunately,

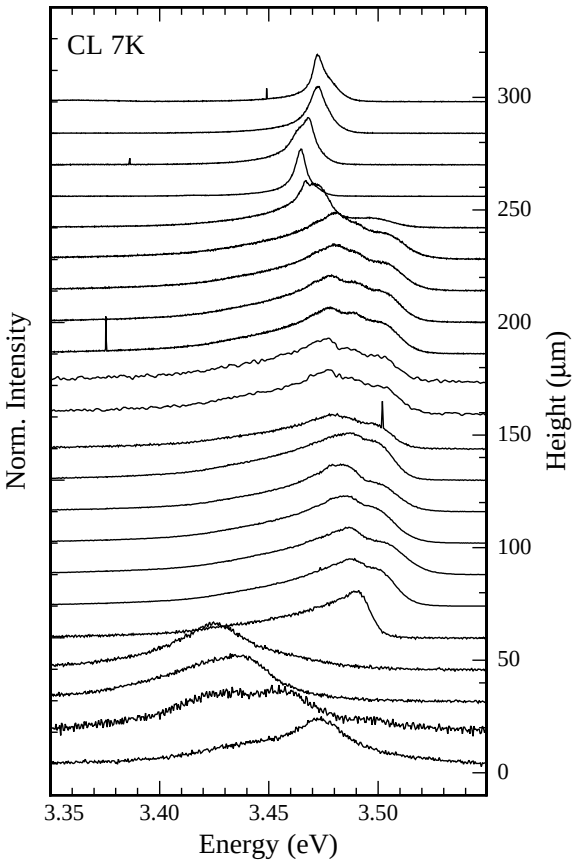

Fig. 7: Low temperature (7K) CL-measurement of the cross-section of the final sample. The first 50µm were grown at low temperature on the ZnO-GaN-template, resulting in a tensile strain. After the removal of the ZnO the first GaN-layers are compressively strained, until a unstrained situation is achieved on the top.

the poor quality of the low temperature layer results in high defect densities also in the overgrown HT-layer. However, the avoidance of stress arising from different thermal expansion coefficients during cool-down or due to a lattice mismatch of GaN and substrate makes the technique anyway very promising for future production of GaN substrates.

Acknowledgments

I would like to thank H. Hochmuth, M. Lorenz and M. Grundmann of Semiconductor Physics Group, Institute of Experimental Physics II, University of Leipzig for PLD growth of ZnO samples, S.B. Thapa for the GaN growth on ZnO by MOVPE, M. Wiedenmann and M. Feneberg, Institute of Semiconductor Physics, University of Ulm for PL and CL measurements.

This work was partly financially supported by Freiberger Compound Materials GmbH, Freiberg and the German Federal Ministry of Education and Research under contract 01BU0620.

References

[1] C.R. Miskys, M.K. Kelly, O. Ambacher, M. Stutzmann, "Freestanding GaN-substrates and devices", *phys. stat. sol. (c)*, vol. 0, pp. 1627–1650, 2003.

[2] S. Nakamura, M. Senoh, S. Nagahama, N. Iwasa, T. Yamada, T. Matsushita, H. Kiyoku, Y. Sugimoto, T. Kozaki, H. Umemoto, M. Sano, K. Chocho, "InGaN/GaN/AlGaN-based laser diodes with cleaved facets grown on GaN substrates", *Appl. Phys. Lett.*, vol. 73, p. 832, 1998.

[3] Y. Oshima, T. Eri, M. Shibata, H. Sunakawa, K. Kobayashi, T. Ichihashi, A. Usui, "Preparation of Freestanding GaN Wafers by Hydride Vapor Phase Epitaxy with Void-Assisted Separation", *Jap. J. Appl. Phys.*, vol. 42, pp. L1–L3, 2003.

[4] S.W. Lee, T. Minegishi, W.H. Lee, H. Goto, H.J. Lee, S.H. Lee, H. Lee, J.S. Ha, T. Goto, T. Hanada, M.W. Cho, T. Yao, "Strain-free GaN thick films grown on single crystalline ZnO buffer layer with in situ lift-off technique", *Appl. Phys. Lett.*, vol. 90, p. 061907, 2007.

[5] T. Suzuki, H.J. Ko, A. Setiawan, J.J. Kim, K. Saitoh, M. Terauchi, T. Yao, "Polarity control of GaN epilayers grown on ZnO templates", *Mater. Sci. Semicond. Proc.*, vol. 6, pp. 519–521, 2003.

[6] M. Lorenz, H. Hochmuth, D. Natusch, H. Börner, K. Kreher, W. Schmitz, "Large-area double-side pulsed laser deposition of $YBa_2Cu_3O_{7-x}$ thin films on 3-in. sapphire wafers", *Appl. Phys. Lett.*, vol. 68, p. 3332, 1996

[7] S.B. Thapa, J. Hertkorn, T. Wunderer, F. Lipski, F. Scholz, A. Reiser, Y. Xie, M. Feneberg, K. Thonke, R. Sauer, M. Dürrschnabel, L.D. Yao, D. Gerthsen, H. Hochmuth, M. Lorenz, M. Grundmann, "MOVPE growth of GaN around ZnO nanopillars", *J. Crystal Growth*, vol. 310, pp. 5139-5142, 2008.

[8] E. Richter, C. Hennig, M. Weyers, F. Habel, J.D. Tsay, W.Y. Liu, P. Brückner, F. Scholz, Y. Makarov, A. Segal, J. Kaeppeler, "Reactor and growth process optimization for growth of thick GaN layers on sapphire substrates by HVPE", *J. Crystal Growth*, vol. 277, pp. 6–12, 2005.

[9] H. Teisseyre, P. Perlin, T. Suski, I. Grzegory, J. Jun, S. Porowski, "Photoluminescence in doped GaN bulk crystal", *J. Phys. Chem. Solids*, vol. 56, pp. 353–355, 1995.

[10] S.B. Thapa, E. Angelopoulos, J. Hertkorn, F. Scholz, A. Reiser, K. Thonke, R. Sauer, H. Hochmuth, M. Lorenz, M. Grundmann, *Proc. 12th European Workshop on MOVPE*, pp. 135, Bratislava, Slovakia, June 3-6, 2007.

Growth of Nonpolar a-plane GaN Templates for HVPE Using MOVPE on r-plane Sapphire

Stephan Schwaiger

In order to establish the growth of nonpolar GaN templates for subsequent overgrowth via hydride vapor phase epitaxy (HVPE) or subsequent device epitaxy we studied the growth of a-plane oriented samples on r-plane sapphire via metal organic vapor phase epitaxy (MOVPE). The growth parameters like reactor pressure, growth temperature and V/III-ratio for the nucleation layer as well as for the GaN main layer grown on top were systematically investigated. A 2 step growth procedure and SiN interlayers were introduced for defect reduction yielding to improved photoluminescence and x-ray rocking curve measurements. This also resulted in reduced in-plane anisotropy and surface roughness values. Hence we achieved high quality nonpolar a-plane GaN layers suitable for subsequent processes.

1. Introduction

GaN-based devices like light emitting diodes (LEDs) are usually grown in c-direction, which is (0001) in crystal notation. Due to the polar character of the group-III nitrides in this particular direction and the biaxial strain induced in InGaN quantum wells having a certain lattice mismatch to the GaN barriers, huge piezoelectric fields develop. Hence the so called quantum confined Stark effect (QCSE) leads to a spatial separation of the wave functions of electrons and holes [1]. Optoelectronic devices therefore suffer from a reduced recombination probability, a red shift of the emission wavelength and a backshift to higher energies for higher drive current [2].

A way to overcome (or to reduce) these negative effects is to grow in nonpolar (or at least semipolar) direction. Nonpolar is every direction perpendicular to the c-axis like for example $[11\bar{2}0]$ (a-plane) and $[10\bar{1}0]$ (m-plane). Because of the lack of real bulk GaN the structures have to be grown either on foreign substrates like r-plane sapphire leading to a-plane GaN [3], or m-plane SiC [4] or $LiAlO_2$ [5] which results in m-plane GaN. However, such unusual growth directions typically lead to highly defective material. Alternatively, sliced pieces from hydride vapor phase epitaxial (HVPE) grown GaN can be used as substrates [6], where such defect formation is drastically reduced. However, only small areas of a few square millimeters of such substrates are nowadays available for exremely high prices. To cut a long story short the perfect substrate is still missing.

Therefore we are currently investigating the optimized growth of nonpolar / semipolar templates which can be used for subsequent device epitaxy. Such quasi substrates should be preferably grown by hydride vapor phase epitaxy (HVPE) to make use of its huge

growth rates of several 10 to 100 µm/h. As the nucleation on foreign substrates is usually quite challenging and requires a wide range of optimization parameters, we have investigated the growth of nonpolar GaN templates for the subsequent HVPE process by the more flexible method of metal organic vapor phase epitaxy (MOVPE).

2. Experimental Procedure

All samples studied here are grown on 2 inch epi-ready r-plane sapphire wafers resulting in a GaN growth in $(11\bar{2}0)$ direction. For the MOVPE growth a commercial horizontal flow Aixtron AIX-200/4 RF-S reactor with the standard precursors trimethylgallium (TMGa), trimethylaluminum (TMAl) and high purity ammonia (NH_3) was used. As carrier gas we used Pd diffused hydrogen. The process temperature was controlled by a pyrometer at the backside of the rotation tray so that all temperatures given in the text are not the real temperatures but only the pyrometer read-out. Before starting growth the substrates were exposed to an in-situ desorption step at 1200°C for 10 min in hydrogen atmosphere [7].

First, we have systematically varied the growth parameters of the AlN nucleation layer (NL) while keeping the growth parameters of the main GaN layer the same as for standard c-plane growth (pressure of 150 hPa, temperature of 1120°C, V/III-ratio of about 2475, growth rate of approx. 2.4 µm/h and a thickness of 2.2 µm [7]). Then the growth parameters of the nonpolar GaN layer itself have been investigated. These studies led to the idea of a two step growth process and to the introduction of in situ SiN interlayers for defect reduction. Applying a constant flow of silane (SiH_4) and ammonia (NH_3), SiN_x is deposited and acts as a nanomask [8,9]. The surface is fractionally covered with SiN that influences the morphology of the overgrown layer resulting in a defect reduction. For this purpose the optimum deposition time and position of that SiN interlayer(s) have been evaluated.

For all these steps we used the crystal quality of the main GaN layer as the figure of merit. This was analysed by x-ray diffraction (XRD) rocking curve measurements (XRC) as well as low temperature (14 K) photoluminescence (PL) spectra. The latter enabling the qualification of typical defects in non-polar layers like basal plane stacking faults (BSFs) or prismatic stacking faults (PSFs) [10,11]. The surface quality was evaluated by scanning electron microscopy (SEM), optical phase contrast microscopy (OM) and atomic force microscopy (AFM).

3. Results and Discussion

3.1 MOVPE grown nucleation layers

Different NLs have been tested (i.e. AlN-NL, LT-GaN-NL), but only the AlN-NL yields to a $(11\bar{2}0)$–oriented surface. For this nucleation different growth temperatures ranging from 1010°C to 1200°C have been investigated. XRCs were recorded for both symmetrical $(11\bar{2}0)$–reflections along and perpendicular to the in-plane c-direction and for the asymmetrical $(10\bar{1}2)$ reflection (Fig. 1). The latter is known to be sensitive to edge and screw

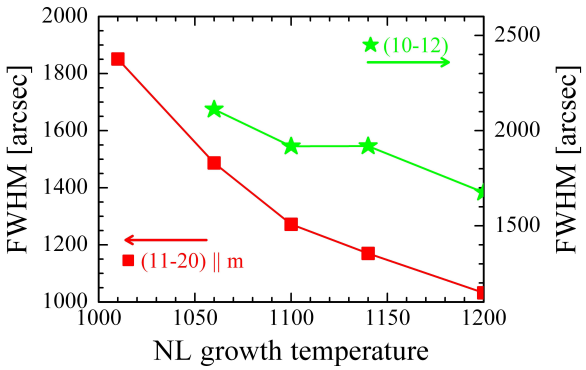

Fig. 1: FWHM of XRD rocking curve measurements of GaN layers with different temperatures during nucleation: $(11\bar{2}0)$–reflection along m-plane (squares, left axis) and $(10\bar{1}2)$–reflection (stars, right axis).

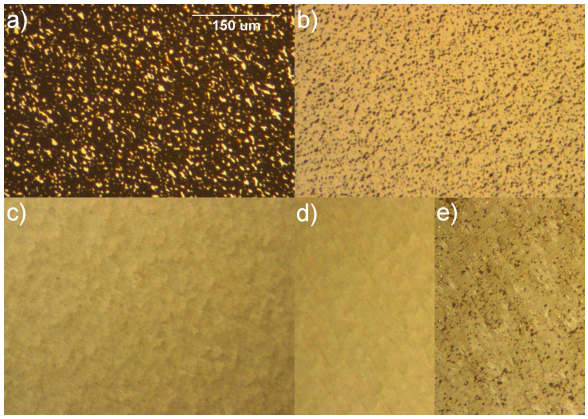

Fig. 2: Optical micrographs from GaN layers with different temperatures during nucleation: a) 1010°C, b) 1100°C, c) 1140°C, d) 1200°C (edge of wafer), e) 1200°C (center of wafer).

dislocations [12]. Obviously, the crystal quality increases with temperature as all FWHM values decrease. In parallel, the surface morphology improves (Fig. 2). At the lowest temperature of 1010°C, only a porous GaN layer was formed, while at 1100°C the layer is closed but suffers from lots of pits. For higher temperatures the pits decrease in number and size. R. Kröger reported that BSFs are generated at the interface to the nucleation layer [13]. It is also known that the crystal quality of AlN increases with increasing growth temperature. Therefore one can assume that the growth of good quality AlN as NL favors growth of good a-plane GaN. Unfortunately for too high temperatures the layers start to become inhomogeneous (see Fig. 2 d and e) probably due to wafer bending during growth. So the optimum temperature has been fixed at 1140°C.

Another challenge in AlN epitaxy (and therefore for this nucleation) are parasitic prereactions of TMAl and ammonia. They can be minimized by lowering the pressure, increasing the total flow and lowering the V/III-ratio resulting in a slight improvement of the surface morphology [14]. Moreover, the growth time of the NL has been varied between 5 min and 15 min without any obvious change in GaN quality. Hence, it has been set to 10 min, which results in a NL thickness of about 20 nm.

3.2 MOVPE grown GaN layers

After having optained reasonable conditions for the nucleation layer, the growth parameters of the main GaN layer were investigated. First, the *reactor pressure* was varied between 100 hPa and 200 hPa: At higher pressure, many pits develop on the surface (Fig. 3). By lowering the pressure, they can be reduced in size and density until they eventually vanish. In parallel, the PL intensity (Fig. 4) of the peak around 3.31 eV is decreasing with decreasing pressure. Paskov et al. [11,15] associated this peak to pyramidal stacking faults (PSFs) and partial dislocations (PDs). Hence lowering the reactor pressure reduces some structural defects. However for a too low pressure the XRD-FWHM values are increasing, while being constant on a fairly low level for higher pressure [16]. In parallel, the surface

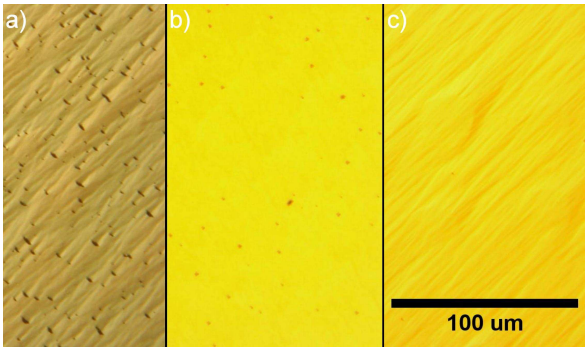

Fig. 3: Optical micrographs from GaN layers grown at different reactor pressure: a) 200 hPa, b) 150 hPa, c) 100 hPa. One can see the increased pit number and size with decreasing pressure.

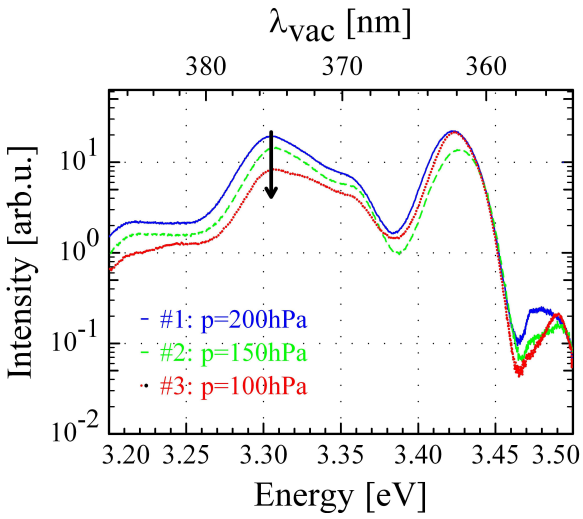

Fig. 4: Photoluminescence of GaN layers with different reactor pressure during growth. 100 hPa (dotted), 150 hPa (dashed), 200 hPa (solid).

gets roughened and develops a stripe like pattern at lower pressures. 150 hPa seems to be the best compromise between crystal quality and surface morphology.

The investigations on the *growth temperature* lead to an optimized temperature at about 1120°C. For lower values the widths of the XRCs increase as well as the PL intensity decreases. If the temperature is too high, the number and size of the pits increase as well as their luminescence [16].

Moreover, a series of samples has been grown with different *V/III-ratio*s ranging from 540 to 2180. The XRC measurements (Fig. 5) do not exhibit a clear trend on the first glance. We just notice a weak tendency to lower FWHM values of the asymmetrical reflections for increasing V/III ratio. In contrast to the crystal quality accessed by XRD, surface morphology is best for the lowest V/III-ratio (Fig. 6). This is confirmed by AFM measurements [16] where we found a root mean square (RMS) roughness of about 1.4 nm for a 5 µm × 5 µm scan of the respective sample.

3.3 2 step growth and introduction of SiN interlayers

The above described studies showed that for best bulk properties a high V/III-ratio and high temperatures are needed, whereas for best surface properties a low V/III-ratio and low pressure are favorable. Therefore we combined these two conditions by adopting a 2 step growth procedure. Best results were achieved for a variation of the V/III ratio only, from 2180 in the first layer with a thickness of approx. 1 µm to 540 in the second layer (thickness approx 1.2 µm) while holding constant the pressure at 150 hPa at a temperature of 1120°C. XRC FWHM values are plotted in Fig. 7 as dashed lines as reference for the following investigations. In order to further reduce the defect density, we studied in-situ

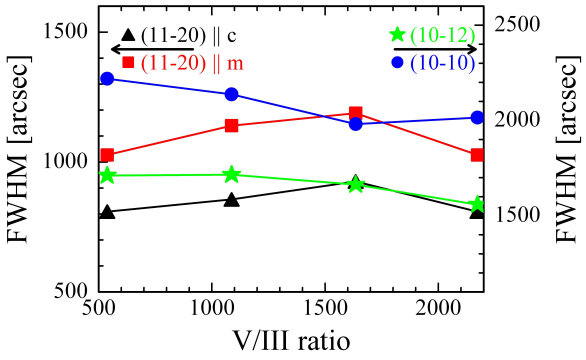

Fig. 5: FWHMs of XRC of GaN layers with different V/III ratio during growth. Symmetrical reflections are plotted on the left axis, asymmetrical ones on the right axis.

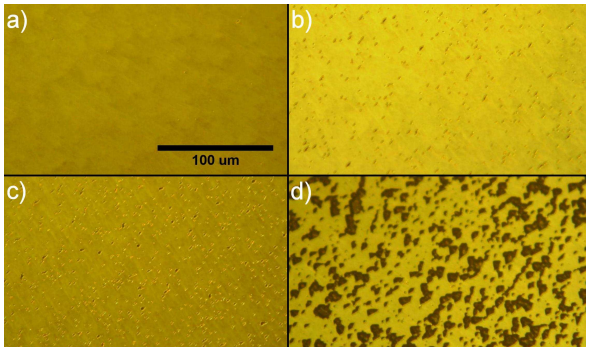

Fig. 6: Optical micrographs from GaN layers with different V/III-ratio during growth: a) 540, b) 1090, c) 1635, d) 2180. One can see the increased pit number and size with increasing flow of ammonia.

deposited SiN interlayers. We used standard conditions for SiN deposition as described elsewhere, showing that SiN can act as a defect reduction layer in c-plane oriented GaN [9]. When varying the SiN position within the GaN layer, we observed that a deposition directly on the nucleation does not help at all (Fig. 7). When shifting the interlayer towards the surface of the GaN, a fast decrease of the FWHM can be observed. Obviously, the blocking layer should be at least 150 nm above the NL with a weak optimum at about 300 nm. As most defects are created at the nucleation layer, we conclude that the SiN needs a certain distance to the defects to act as blocking layer.

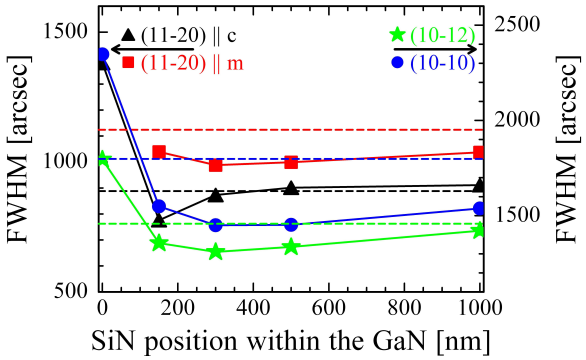

Fig. 7: FWHMs of XRC of GaN layers with introduced SiN interlayers plotted versus the SiN position within the GaN layer. The total thickness was kept constant at ≈ 2.2 µm.

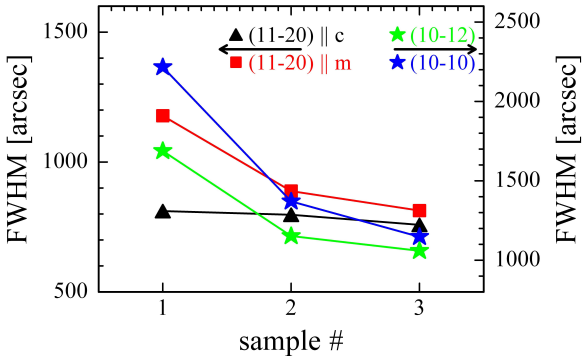

Fig. 8: FWHMs of XRC of a "simple" GaN layer (# 1) and samples with one (# 2) and two (# 3) SiN interlayers after 0.3 µm and 0.3/1.0 µm, respectively.

Evaluations of the influence of the deposition time on the crystal quality were also made. By increasing the deposition time the XRC FWHMs decrease owing to a better crystal quality. However, at the same time the surface gets more and larger pits. By optimizing the growth parameters again and in particular increasing the thickness of the top GaN layer to about 2.3 µm, it was possible to achieve nearly pit-free surfaces.

Figure 8 shows a comparison of the XRC data from three different samples, without

and with one and two SiN interlayers, respectively. The improvement in crystal quality is obvious, the FWHMs are drastically reduced down to values below 750 arcsec for the symmetrical $(11\bar{2}0)$ reflection and around 1050 arcsec and 1150 arcsec for the asymmetrical $(10\bar{1}2)$ and $(10\bar{1}0)$ reflections, respectively. The in-plane anisotropy, which seems to be undesirable for nonpolar growth [17] was reduced as well. This advancement in crystal quality was also confirmed by PL (Fig. 9). For GaN with one and two interlayers, not only the total intensity increases but also the near band edge emission (NBE) above 3.47 eV improves, while the luminescence from BSFs ($\approx$ 3.42 eV, [11]) and other defects ($\approx$ 3.30 – 3.35 eV, [11]) decreases relatively to the NBE. Additionally the surface roughness,

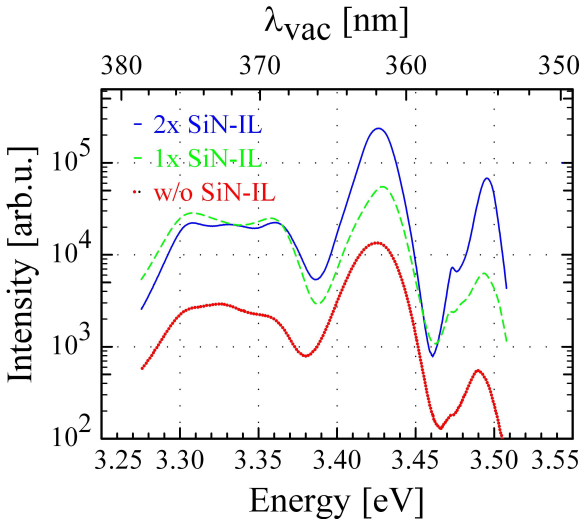

Fig. 9: PL of a "simple" GaN layer (dotted) and samples with one (dashed) and two (solid) SiN interlayers after 0.3 µm and 0.3/1.0 µm, respectively.

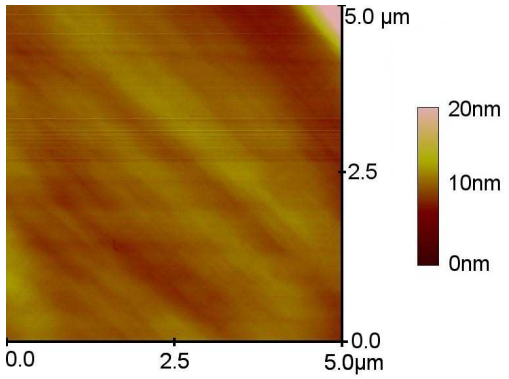

Fig. 10: 2D AFM measurement showing the smooth surface of an optimized a-plane GaN layer with two inserted SiN interlayers for defect reduction.

measured by AFM (Fig. 10) was reduced to values around 1.0 nm for a 5 µm × 5 µm scan.

4. Summary

By carefully optimizing the NL and the bulk GaN layer, we could achieve the growth of high quality nonpolar a-plane GaN. This was evidenced by small XRD FWHM values below 750 arcsec for the symmetrical $(11\bar{2}0)$ reflection and around 1050 and 1150 arcsec for the asymmetrical $(10\bar{1}2)$ and $(10\bar{1}0)$ reflections, respectively. Additionally, the PL of the NBE could be drastically improved by introducing a 2 step growth procedure and in particular by inserting SiN defect reducing interlayers. Furthermore, very smooth surfaces could be optained with an AFM RMS around 1.0 nm for a (5×5) µm^2 scan. In conclusion, we produced high quality nonpolar GaN templates suitable for subsequent overgrowth in HVPE.

5. Acknowledgments

This work was financially supported by the Deutsche Forschungsgemeinschaft within the research group "Polarization Field Control in Nitride Light Emitters (PolarCoN)" under contract no. Scho 393/22–1. The sample characterization by Wenshan Pang is gratefully acknowledged.

References

[1] F. Bernardini, V. Fiorentini and D. Vanderbilt, "Spontaneous polarization and piezoelectric constants of III-V nitrides", *Phys. Rev. B*, vol. 56, pp. R10024, 1997.

[2] T. Takeuchi, C. Wetzel, S. Yamaguchi, H. Sakai, H. Amano, and I. Akasaki "Determination of piezoelectric fields in strained GaInN quantum wells using the quantum confined Stark effect", *Appl. Phys. Lett.*, vol. 73, pp. 1691, 1998.

[3] M.D. Craven, S.H. Lim, F. Wu, J.S. Speck and S.P. DenBaars "Structural characterization of nonpolar $(11\bar{2}0)$ a-plane GaN thin films grown on (1102) r-plane sapphire", *Appl. Phys. Lett.*, vol. 81, pp. 469–471, 2002.

[4] B. Imer, F. Wu, M.D. Craven, J.S. Speck and S.P. DenBaars "Stability of $(1\bar{1}00)$ m-plane GaN Films Grown by Metalorganic Chemical Vapor Deposition", *Jap. J. Appl. Phys.*, vol. 45, no. 11 pp. 8644–8647, 2006.

[5] A-T. Cheng, Y-K. Su, W-C. Lai and Y-Z. Chen "Metalorganic Vapor Phase Epitaxy Growth of m-plane GaN Using $LiAlO_2$ Substrates", *Jap. J. Appl. Phys.*, vol. 47, no. 4 pp. 3074–3076, 2008.

[6] T. Paskova, R. Kroeger, S. Figge, D. Hommel, V. Darakchieva, B. Monemar et al. "High-quality bulk a-plane GaN sliced from boules in comparison to heteroepitaxially grown thick films on r-plane sapphire", *Appl. Phys. Lett.*, vol. 89, pp. 051914, 2006.

[7] J. Hertkorn, P. Brückner, S.B. Thapa, T. Wunderer, F. Scholz, M. Feneberg, K. Thonke, R. Sauer, M. Beer and J. Zweck "Optimization of nucleation and buffer layer growth for improved GaN quality", *J. Crystal Growth*, vol. 308, pp. 30–36, 2008.

[8] A. Chakraborty, K.C. Kim, F. Wu, J.S. Speck, S.P. DenBaars and U.K. Mishra "Defect reduction in nonpolar a-plane GaN films using in situ SiN_x nanomask", *Appl. Phys. Lett.*, vol. 89, pp. 041903, 2006.

[9] J. Hertkorn, F. Lipski, P. Brückner, T. Wunderer, S.B. Thapa, F. Scholz, A. Chuvilin, U. Kaiser, M. Beer and J. Zweck "Process optimization for the effective reduction of threading dislocations in MOVPE grown GaN using in situ deposited SiN_x masks", *J. Crystal Growth*, vol. 310, pp. 4867–4870, 2008.

[10] R. Liu, A. Bell, F.A. Ponce, C.Q. Chen, J.W. Yang and M.A. Khan "Luminescence from stacking faults in gallium nitride", *Appl. Phys. Lett.*, vol. 86, pp. 021908, 2005.

[11] P.P. Paskov, T. Paskova, B. Monemar, S. Figge, D. Hommel, B.A. Haskell, P.T. Fini, J.S. Speck and S. Nakamura "Optical properties of nonpolar a-plane GaN layers", *Superlattices and Microstructures*, vol. 40, pp. 253–261, 2006.

[12] B. Heying, X.H. Wu, S. Keller, Y. Li, D. Kapolnek, B.P. Keller, S.P. DenBaars and J.S. Speck "Role of threading dislocation structure on the x-ray diffraction peak widths in epitaxial GaN films", *Appl. Phys. Lett.*, vol. 68, pp. 643–645, 1996.

[13] R. Kröger, "Defects and Interfacial Structure of a-plane GaN on r-plane Sapphire", Chap. 11 in *Nitrides with Nonpolar Surfaces. Growth, Properties and Devices.*, T. Paskova (Ed.), pp. 287–318. Weinheim: Wiley-VCH Verlag GmbH & Co., 2008.

[14] S. Schwaiger and F. Scholz "Heteroepitaxial Growth of a-plane GaN on r-plane Sapphire" talk at *Kick-Off-Meeting DFG FOR 957 (PolarCoN)*, Ulm, 2008

[15] P.P. Paskov, R. Schifano, B. Monemar, T. Paskova, S. Figge and D. Hommel "Emission properties of a-plane GaN grown by metal-organic chemical-vapor deposition", *J. Appl. Phys.*, vol. 98, pp. 093519, 2005.

[16] S. Schwaiger, F. Lipski, T. Wunderer and F. Scholz "Growth studies about nonpolar a-plane GaN via MOVPE and HVPE" talk at *DGKK Workshop*, Braunschweig, 2008

[17] H. Wang, C. Chen, Z. Gong, J. Zhang, M. Gaevski, M. Su, J. Yang and M. Asif Khan "Anisotropic structural characteristics of $(11\bar{2}0)$ GaN templates and coalesced epitaxial lateral overgrown films deposited on $(10\bar{1}2)$ sapphire", *Appl. Phys. Lett.*, vol. 84, pp. 499–501, 2004.

3D GaN Structures with Reduced Piezoelectric Fields For Efficient Quantum Well Emission

Thomas Wunderer

A fabrication method for the formation of 3D GaN structures with reduced piezoelectric field is presented. Via optimized selective epitaxy the surface is just composed of hexagonally patterned semipolar $\{1\bar{1}01\}$ *or* $\{11\bar{2}2\}$ *planes. GaN growth with less* NH_3 *at a higher growth speed, a doubled effective area and good light outcoupling properties compared to c-plane growth are additional advantages of this effective technique. The high material quality is confirmed via PL and CL measurements (FWHM of* D^0X*: 2.6 meV). No defect related optical transitions, often observed in non- and semipolar GaN, were found. An InGaN QW grown on these semipolar planes showed efficient green (522 nm) light emission in spite of a reduced influence of the quantum confined Stark effect (QCSE).*

1. Introduction

In recent years, much attention has been paid to group III-nitrides due to their properties suited for the fabrication of efficient optoelectronic devices. High-performance InGaN/GaN based light emitting diodes (LEDs) with an emission wavelength in the blue/violet spectral region or in combination with phosphors for white light sources are commercially available nowadays [1]. However, for longer wavelengths the efficiency of those devices grown in the commonly used c-direction of GaN is continuously decreasing with increasing indium content in the active region [2]. This fact is thought to be in large part caused by strong built-in electrical fields as a result of the biaxially compressively stressed InGaN QWs. Those piezoelectric fields lead to a local separation of electrons and holes within the quantum wells (QWs) and consequently to less efficient device structures due to a reduced overlap of electron and hole wave functions.

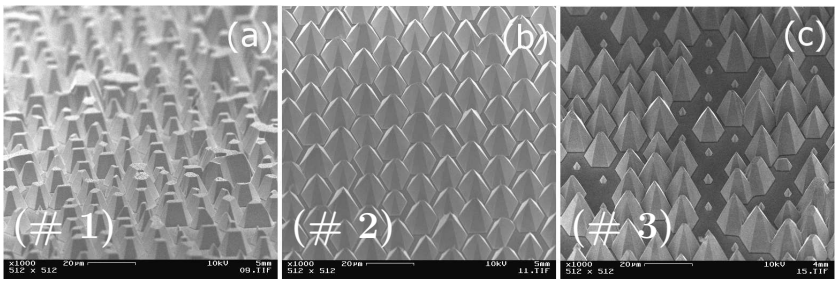

Fig. 1: Bird's eye view of normal pyramids grown with f_{TMGa} = 51 µmol/min (a), f_{TMGa} = 102 µmol/min (b), and f_{TMGa} = 153 µmol/min (c).

By suppressing these strong piezoelectric fields it is expected that the efficiency of nitride-based devices can be drastically improved. That is the reason why many groups are currently dealing with the investigation of GaN and GaN-based devices in non- and semipolar growth directions, as it could be demonstrated experimentally that the piezoelectric fields are reduced for QWs grown along these crystal directions [3].

Nevertheless, the competition between material quality and sample size is still limiting the use of non- or semipolar material for industrial production. On the one hand on foreign substrates with a conventional size just inferior material quality compared to c-plane growth can be achieved up to now. Non-radiative recombination is then compensating the advantage of the reduced fields and leads to the bad performance of such devices [4,5]. On the other hand high quality material of non- and semipolar GaN can be obtained by cutting small pieces from c-plane grown HVPE GaN. Those substrates provide a very low threading dislocation and stacking fault density which seem to be the key factors for the remarkable device performance [6, 7]. However, the sample size in the range of 3 x 20 mm^2 [7] and its high price are still limiting factors for any mass production [8].

In this study we present a method for the fabrication of semipolar GaN planes with high material quality and the possibility for large area production. Selective epitaxy is used to grow three dimensional (3D) GaN structures providing semipolar $\{1\bar{1}01\}$ and $\{11\bar{2}2\}$ GaN surfaces in hexagonal patterns. By optimized growth conditions for the second epitaxial step the surface is just composed of semipolar planes with reduced piezoelectric fields which are useful for efficient light emitters.

2. Experimental

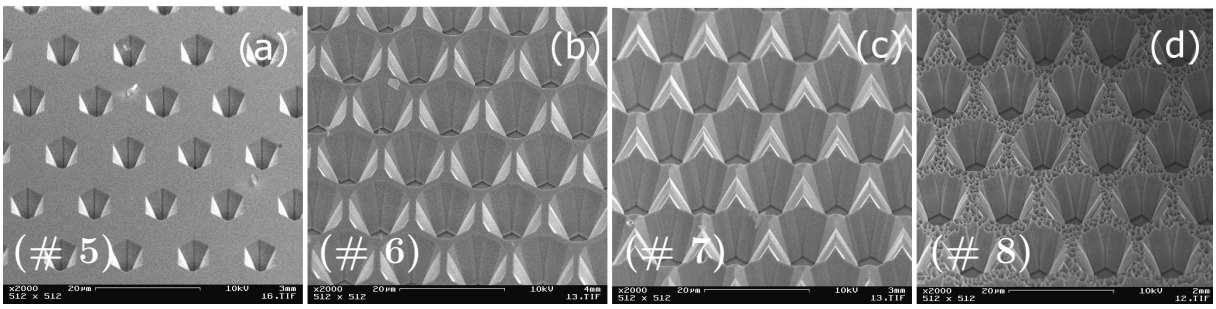

Fig. 2: 45° view on inverse pyramids (3 µm opening, 10 µm mask) grown at T = 1120°C (a), 1060°C (b), 950°C (c), and 850°C (d).

The samples were grown by low pressure metalorganic vapor phase epitaxy (MOVPE) using trimethylgallium (TMGa), triethylgallium (TEGa), trimethylindium (TMIn), and ammonia (NH_3) as precursors. First, about 2 µm thick high quality GaN templates were fabricated. The well known and established c-plane growth was performed on c-plane sapphire substrates including an in-situ SiN interlayer for efficient defect reduction [9]. After the deposition of 200 nm SiO_2 mask material via plasma enhanced chemical vapor

Table 1: Growth parameters of different samples

sample no.	T [°C]	f_{TMGa} [µmol/min]	f_{NH3} [mmol/min]	p [hPa]
# 1	1120	51	90	150
# 2	1120	102	90	150
# 3	1120	153	90	150
# 4	1120	102	90	250
# 5	1120	102	45	150
# 6	1060	102	45	150
# 7	950	102	45	150
# 8	850	102	45	150

deposition (PECVD) different hexagonally shaped patterns were formed using standard photolithography and reactive ion etching (RIE).

One part of the test pattern consists of hexagonal openings (3 µm), whereas the masked areas were fixed to a width of 3 µm and 10 µm. This design allows the formation of ordered pyramids with $\{1\bar{1}01\}$ facets (in the following text called 'normal'), similar to the epitaxial lateral overgrowth (ELOG) technique that is normally used for defect reduction in GaN growth, see e.g. [10]. The counterpart of the mask pattern consists of hexagonal masked areas surrounded by open stripes with a width of 3 µm. The diameter of the masked areas is set to 3 µm and 10 µm. This pattern allows the growth of inverse pyramids where predominantly $\{11\bar{2}2\}$ facets are formed (in the following text called 'inverse'). The formation of normal and inverse pyramids can be understood by the different growth speed in a- and m-direction. The growth in $\langle 11\bar{2}0\rangle$-direction is found to be faster than in $\langle 1\bar{1}00\rangle$-direction. That is the reason why one can find $\{1\bar{1}0x\}$ facets (normal pyramids) if the mask is designed for divergenting growth and $\{11\bar{2}x\}$ facets for convergenting growth (inverse pyramids).

In order to achieve homogeneously distributed structures in combination with a high material quality and good optical properties, systematic variations of the GaN growth parameters were investigated in the second epitaxial step. On top of these structures an InGaN single quantum well (SQW) was grown and then capped with undoped GaN. The properties of the QW emission act as a direct monitor for the semipolar InGaN/GaN material quality. Whereas the QW emission for the first series had a moderate wavelength of about 470 nm it was pushed into the green spectral region after the optimization of the underlayer 3D semipolar GaN structures. Up to 522 nm were measured by adjusting the growth parameters of the active region.

For the study of the structural and optical properties optical and scanning electron microscopy (SEM) investigations were performed, combined with photoluminescence (PL) and locally resolved cathodoluminescence (SEM-CL) measurements.

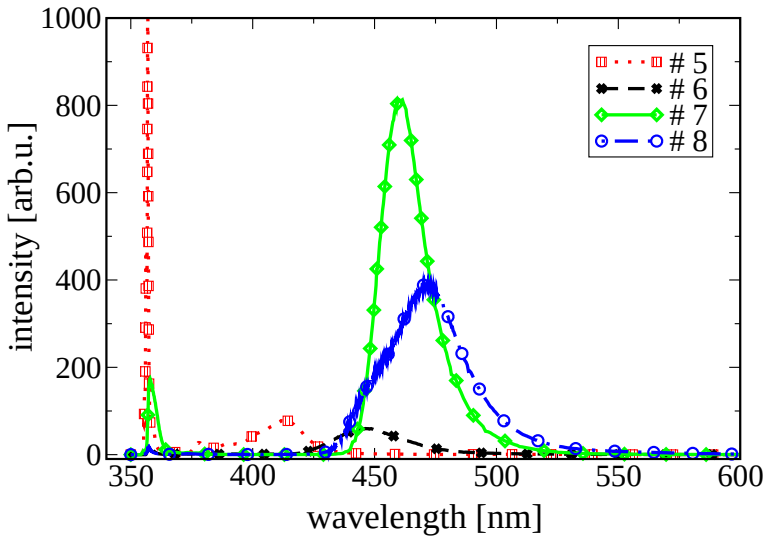

Fig. 3: PL measurement of inverse pyramids (3 µm opening, 10 µm mask) grown at $T = 1120°C$ (# 5), 1060°C (# 6), 950°C (# 7), and 850°C (# 8).

3. Results and Discussion

First, our standard c-plane GaN growth parameters applied to the masked template (sample # 1, see table 1). Fig. 1(a) shows the resulting structures of an area where normal pyramids are expected. As can be seen 3D structures developed, but their distribution is inhomogenious and no distinct facet type is dominating. On areas where inverse pyramids are expected just a completely closed layer was found for all geometries. Obviously, our standard growth conditions are not applicable for the formation of 3D structures with semipolar surfaces. Different parameters are well known to reduce the lateral (2D) and force the vertical (3D) growth mode: A low V/III ratio, a low growth temperature, and a high reactor pressure. In sample # 2 the V/III ratio was lowered by a doubled TMGa flow. The normal pyramids are now well ordered and developed $\{1\bar{1}01\}$ facets as the most stable surface (see Fig. 1(b)). The symmetry of each pyramid is good but not perfect. At the relatively sharp apex of the pyramids defect formation is visible. By further increasing the TMGa flow to $f_{\mathrm{TMGa}} = 153\,\mu\mathrm{mol/min}$ (sample # 3) following situation can be recognized (see Fig. 1(c)): Besides well ordered structures similar to sample # 2 stochastically distributed areas can be found with pyramids just as big as the mask opening (3 µm). Similar behavior was found for sample # 5 with a TMGa flow of $f_{\mathrm{TMGa}} = 102\,\mu\mathrm{mol/min}$, but with reduced NH_3 of $f_{\mathrm{NH3}} = 45\,\mathrm{mmol/min}$ (not shown). Obviously a too low V/III leads to a inhomogenious growth for the individually growing pyramids.

Looking to the results of the PL measurements performed for sample # 1 to # 3, also # 2 is favored due to the highest intensity and the longest wavelength for the QW emission (not shown).

Based on # 2 the reactor pressure is now increased to $p = 250\,\mathrm{hPa}$ in sample # 4 to further enhance the 3D growth mode. But because the PL intensity was reduced and no big changes in the pyramids' shape could be observed (not shown), the pressure was kept

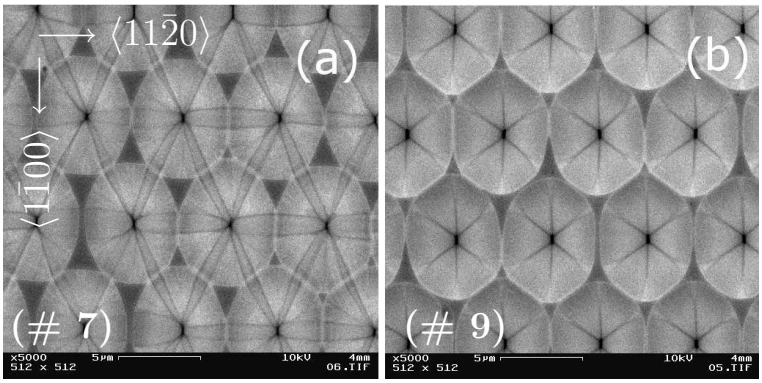

Fig. 4: Top view on inverse pyramids (3 µm opening, 3 µm mask) grown without (a) and with (b) smoothing step.

at $p = 150$ mbar for the following experiments.

As already mentioned, sample # 5 was grown with a reduced NH_3 of $f_{NH3} = 45$ mmol/min. Although this low V/III ratio (at high growth temperature) is not favored for the growth of normal individually grown pyramids due to their inhomogenious distribution, the optical properties of the GaN as well as of the InGaN QWs grown on the inverse pyramids were drastically improved. This is the reason why in the following temperature series the V/III ratio was kept as in # 5.

Based on sample # 5 ($T = 1120$°C) the reactor temperature during the GaN growth was gradually reduced. The temperature was set to $T = 1060$°C (# 6), $T = 950$°C (# 7) and $T = 850$°C (# 8). Due to the fact that inverse pyramids show a stronger influence on these changes and their homogeneity is basically better, we concentrate on them in the following investigations. Fig. 2 shows the SEM pictures of inverse pyramids with a mask width of 10 µm for this temperature series. The c-plane surface which is present on a big area in sample # 5 is strongly reduced in # 6 and almost vanished in # 7. When the temperature was further reduced to $T = 850$°C a rough c-plane surface is observed. Under these conditions the temperature is too low for defect-free growth. Hence, the favored temperature is set to $T = 950$°C. PL measurements also confirm this trend. Sample # 7 shows the best QW emission for inverse as well as for normal grown pyramids (Fig. 3).

Having a closer look to the geometrical properties of the inverse pyramids of # 7 (Fig. 2(c)), besides six rectangular shaped $\{11\bar{2}2\}$ facets one can also find six triangular shaped $\{1\bar{1}01\}$-facets. These properties also exist for the small mask geometry, (Fig. 4(a)). In this case two distinct QW peaks can be observed in PL measurements (Fig. 5). Determined by SEM-cathodoluminescence the two peaks can exclusively be assigned to the two facet types where the $\{1\bar{1}01\}$ facets show the longer emission (not shown). This fact leads to an additional step in the growth procedure. By ramping the temperature up to $T = 1120$°C prior to the QW growth (# 9) a smoothing of the surface is desired. As can be seen in Fig. 4(b) this step is helpful to force the $\{11\bar{2}2\}$ facets and minimize its counterpart which were even dominating previously. Hence, the PL QW emission just shows one transition

(Fig. 5).

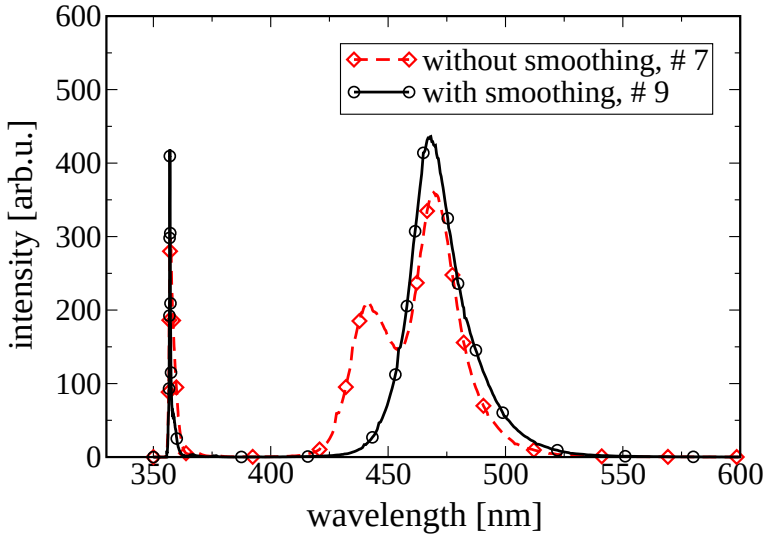

Fig. 5: PL measurement of inverse pyramids (3 µm opening, 3 µm mask) grown with (# 9) and without (# 7) smoothing step.

Sample # 9 is now the base for pushing the QW emission into the green region. Due to the reduced piezoelectric field on the semipolar planes the influence of the quantum confined Stark effect (QCSE) is also reduced. Consequently, for the same wavelength more indium and/or thicker QWs are needed in comparison to c-plane growth. Adjusting the growth parameters of the active region to an In incorporation of about 30 %, efficient green (522 nm) QW emission could be realized on semipolar pyramids. In Fig. 6 the PL spectra of inverse pyramids with the small geometry (see Fig. 4(b)) of sample # 10 are depicted. At $T = 14$ K unstained GaN related transitions are observed without any hint for defect related transitions, as often observed from non- and semipolar grown GaN [11]. Furthermore, the slight drop of the QW intensity at $T = 295$ K gives evidence for a high internal quantum efficiency (IQE).

4. Conclusion

We presented a fabrication method for the formation of 3D GaN planes with reduced piezoelectric field. The 3D structures double the effective area, provide semipolar surfaces and allow good light outcoupling. Additionally, the low NH_3 at high growth speed can reduce fabrication costs. Efficient green (522 nm) QW emission on these structures could be demonstrated.

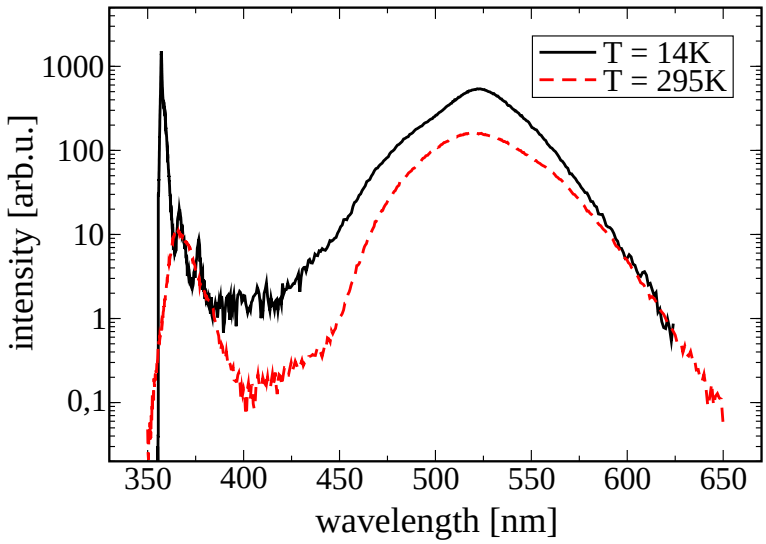

Fig. 6: PL measurement of inverse pyramids (3 µm opening, 3 µm mask) with long emission wavelength (# 10) at $T = 14\,\mathrm{K}$ and $T = 295\,\mathrm{K}$.

References

[1] Y. Narukawa, M. Sano, T. Sakamoto, T. Yamada, and T. Mukai, "Successful fabrication of white light emitting diodes by using extremely high external quantum efficiency blue chips", *phys. stat. sol. (a)*, vol. 205, no. 5, pp. 1081–1085, 2008.

[2] G. Chen, M. Craven, A. Kim, A. Munkholm, S. Watanabe, M. Camras, W. Götz, and F. Steranka, "Performance of high-power III-nitride light emitting diodes", *phys. stat. sol. (a)*, vol. 205, no. 5, pp. 1086–1092, 2008.

[3] M. Feneberg, F. Lipski, R. Sauer, K. Thonke, T. Wunderer, B. Neubert, P. Brückner, and F. Scholz, "Piezoelectric fields in GaInN/GaN quantum wells on different crystal facets", *Appl. Phys. Lett.*, vol. 89, pp. 242112–1–3, 2006.

[4] A. Chakraborty, B. Haskell, H. Masui, S. Keller, J. Speck, S. DenBaars, S. Nakamura, and U. Mishra, "Nonpolar m-plane blue-light-emitting diode lamps with output power of 23.5 mW under pulsed operation", *Jpn. J. Appl. Phys.*, vol. 45, pp. 739–741, 2006.

[5] B. Liu, R. Zhang, Z. L. Xie, C. X. Liu, J. Y. Kong, J. Yao, Q. J. Liu, Z. Zhang, D. Y. Fu, X. Q. Xiu, H. Lu, P. Chen, P. Han, S. L. Gu, Y. Shi, and Y. D. Zheng, "Nonpolar m-plane thin film GaN and InGaN/GaN light-emitting diodes on $LiAlO_2$ (100) substrates", *Appl. Phys. Lett.*, vol. 91, pp. 253506–1–3, 2007.

[6] M. Schmidt, K.-C. Kim, H. Sato, N. Fellows, H. Masui, S. Nakamura, S. DenBaars, and J. Speck, "High power and high external efficiency m-plane InGaN light emitting diodes", *Jpn. J. Appl. Phys.*, vol. 46, pp. L126–128, 2007.

[7] K.-C. Kim, M. Schmidt, H. Sato, F. Wu, N. Fellows, M. Saito, K. Fujito, J. Speck, S. Nakamura, and S. DenBaars, "Improved electroluminescence on nonpolar m-plane InGaN/GaN quantum wells LEDs", *phys. stat. sol. (RRL)*, vol. 1, pp. 125–127, 2007.

[8] U. Schwarz and M. Kneissel, "Nitride emitters go nonpolar", *phys. stat. sol. (RRL)*, vol. 1, pp. A44–46, 2007.

[9] J. Hertkorn, F. Lipski, P. Brückner, T. Wunderer, S.B. Thapa, F. Scholz, A. Chuvilin, U. Kaiser, M. Beer, and J. Zweck, "Process optimization for the effective reduction of threading dislocations in MOVPE grown GaN using in situ deposited SiN_x masks", *J. Cryst. Growth.*, vol. 310, pp. 4867–4870, 2008.

[10] T. Zheleva, O.-H. Nam, M. Bremser, and R. Davis, "Dislocation density reduction via lateral epitaxy in selectively grown GaN structures", *Appl. Phys. Lett.*, vol. 71, pp. 2472–2474, 1997.

[11] P. P. Paskov, R. Schifano, B. Monemar, T. Paskova, S. Figge, and D. Hommel, "Emission properties of a-plane GaN grown by metal-organic chemical-vapor deposition", *J. Appl. Phys.*, vol. 98, pp. 093519–1–3, 2007.

Investigations of Processing Methods for GaN-Based Laser Diodes

Mohamed Fikry

The development of an optimized recipe for the processing of a MQW AlGaInN based oxide stripe laser diode grown on c-plane sapphire has been investigated. Two processing sequences involving Reactive Ion Etching (RIE) were compared. The first relied on the use of SiO_2 *as a dry etch-mask, whereas in the second, the use of nickel was utilized. The critical step of smooth and vertical mirror formation played a significant role in dictating the choice of the dry-etch mask material. A facet inclination angle of 80° was achieved. Under pulsed electrical current injection, we measured a threshold current density of 6.1 kA/cm*^{2} *on the laser device.*

1. Introduction

Lately, laser diodes based on the group-III nitirde material system have been receiving a large attention along with the rapid emerge of short wavelength optoelectronics. They can be considered as promising candidates for a wide variety of applications including high density information storage on optical media, projection displays in addition to possible treatments in the medical field [1].

One critical parameter that can greatly influence the performance of the lasing device is the facet or mirror quality of the resonator, which can directly influence the percentage of optical feedback. The smoothness and degree of anisotropy of the facet can thus play a significant role. For III-nitrides grown on c-plane sapphire substrates, mirror formation by cleavage gets very difficult due to a 30 ° rotation of the GaN layer with respect to the sapphire wafer [2]. Furthermore, due to the high chemical stability of the nitrides, the use of wet etching techniques becomes more challenging.

A number of dry etching techniques can be applied for the afore-mentioned material system including Reactive-Ion-Etching (RIE), Chemically Assissted Ion Beam Etching (CAIBE) as well as Inductively Coupled Plasma (ICP). The choice of the mask material in the dry etch process (selectivity between mask material and material to be etched), along with the etching conditions inside the reactor (pressure, power and the choice of gases), can significantly influence the final etched facet profile [3]. In addition, there exists a very high degree of sensitivity to any minor alterations to the lithography conditions that would dictate the pattern to be transferred to the etched feature.

In this work, we present a comparison of two processing sequences based on RIE using two different mask materials (SiO_2 and nickel) for an MOCVD grown laser structure on c-plane sapphire substrate. In addition, characterization of the laser device under pulsed current injection is reported.

2. Epitaxial Structure

The MOVPE growth sequence for the investigated samples is shown in a simplified manner in Fig. 1. The detailed growth sequence is described as follows. Starting from a c-plane oriented sapphire substrate, an undoped GaN buffer layer of 1.3 µm involving AlN nucleation and a SiN monolayer for defect reduction is grown [4]. After that, two subsequent layers of silicon doped GaN with doping concentrations of $5 \times 10^{18}\,\mathrm{cm}^{-3}$ and $1 \times 10^{19}\,\mathrm{cm}^{-3}$ and thicknesses of 750 nm and 300 nm are used for providing n-doping and improving the carrier injection at the n-contacts. Then 410 nm of $Al_{0.09}Ga_{0.91}N$:Si together with 100 nm GaN:Si are grown for the optical confinement of the laser mode (Separate Confinement Heterostructure). The multi-quantum well (MQW) active region consists of 2 quantum wells of 2.6 nm $In_{0.09}Ga_{0.91}N$ separated by 12 nm GaN barriers. A spacer layer of 20 nm followed by a highly doped $Al_{0.2}Ga_{0.8}N$: Mg (p-AlGaN) electron barrier layer of 10 nm comes directly above the MQWs. The layer sequence starting from the n-AlGaN to the start of the MQWs is approximately mirrored to the p-side directly above the afore-mentioned carrier confinement layer. The top most two layers are a 60 nm highly doped p-GaN (around $6 \times 10^{19}\,\mathrm{cm}^{-3}$) followed by a 20 nm p-cap doped as high as $1 \times 10^{20}\,\mathrm{cm}^{-3}$ for the formation of a good ohmic contact.

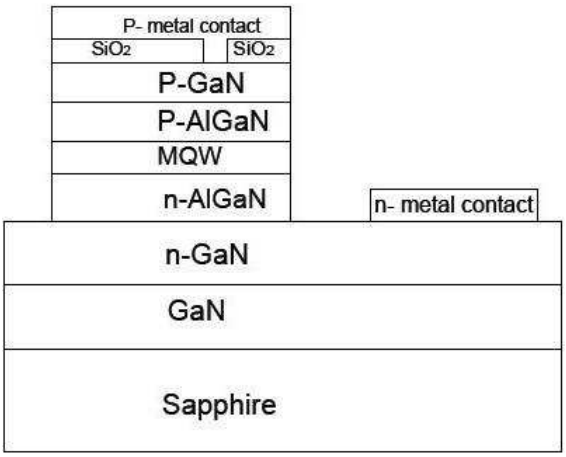

Fig. 1: Epitaxial structure and layout of laser device after processing.

3. Laser Processing Using a SiO_2 Dry-Etch Mask

The process sequence that has been followed as a starting point for the investigations is summarized as follows: (1) Thermal activation of the Mg dopant atoms for generation of holes at 750 °C for 1 minute, (2) PECVD deposition of SiO_2 as a passivation layer, (3) defining the SiO_2 mesa dimensions using photolithography and RIE involving CF_4 plasma, (4) dry etching of the GaN resonator using Cl_2, BCl_3 and Ar plasma RIE, (5) dry etching of the oxide stripe in a CF_4 plasma RIE, and finally, (6) p- and n- contact

formation using electron beam evaporation of the necessary metals and Rapid Thermal Annealing (RTA).

A number of problems have been observed for the use of SiO_2 as a direct dry-etch mask in the Cl_2 based plasma RIE. First, we observed the formation of highly dense micro-pillars (also referred to as surface grass) on the etched n-GaN layer (Fig. 2). These micro-pillars can be removed by a subsequent step of KOH crystallographic wet etching. However, the removed grass leaves a very rough surface morphology (Fig. 3) that is assumed to considerably degrade the contact resistance for the n-contact.

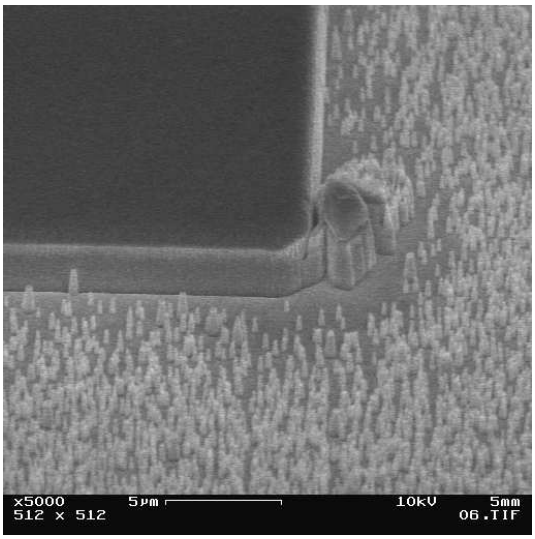

Fig. 2: Dense grass formation after GaN dry etching.

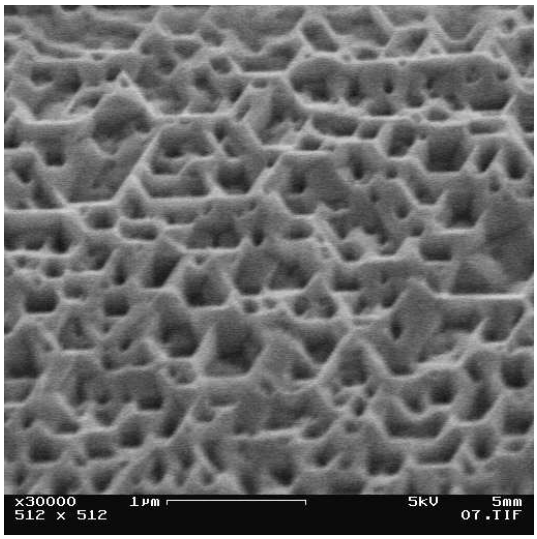

Fig. 3: Rough n-GaN floor after removal of grass pillars using hot KOH solution.

Obviously, small SiO_2 particles sputtered from the mask material as well as from the quartz substrate holder acted as micro-masking particles during dry etching. As the etch rate of SiO_2 is a factor of 6 to 7 less than that of GaN, the GaN directly underneath the micro-SiO_2 particles is not etched, thus revealing a pillar shape [5].

Another problem related to the SiO_2 masking properties was the generation of etched facets with highly rough surfaces (Fig. 4). Such a high degree of facet roughness is expected to degrade the mirror reflectivity needed for lasing action.

Finally, it was also observed that the etched facet exhibited a two-sloped sidewall profile (mask facetting effect). In other words, the upper part of the etched feature exhibit a smaller slope as compared to the lower one (Fig. 5). This phenomenon could be explained as a lateral shrinkage of the mask material as explained in [5] and [3]. The solution to this problem is either to use a higher thickness of the mask material and hence mask facetting would not reach the GaN mesa top edge within the etching time, or to use another mask material that is more resistant to the employed etch conditions. However, using a thicker mask would cause more difficulties for the fore-coming step of stripe opening etching [5].

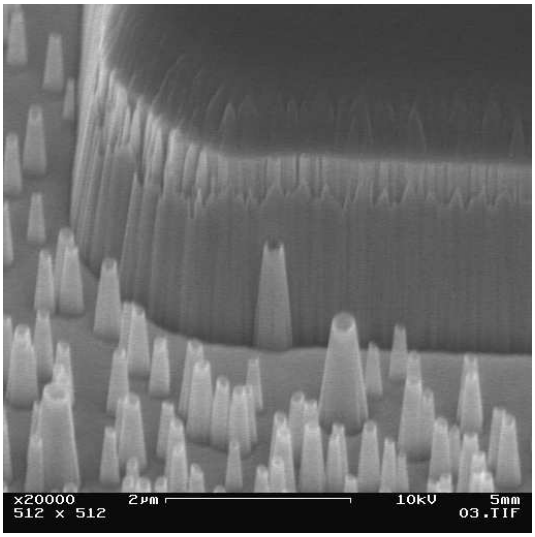

Fig. 4: Rough sidewall surfaces generated using a Sio_2 dry-etch mask.

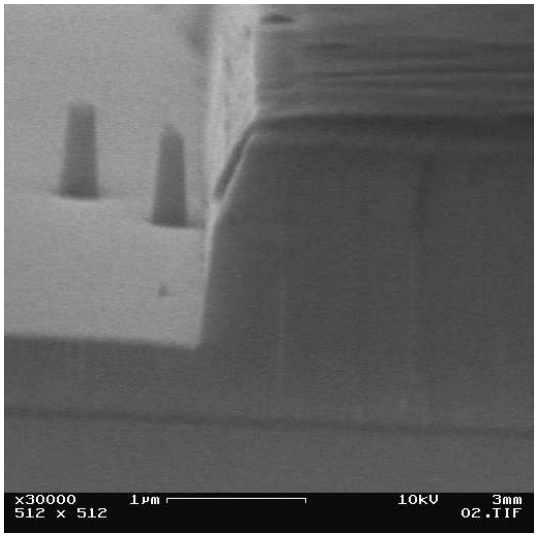

Fig. 5: A two-sloped sidewall profile generated due to mask facetting effect.

4. Optimization of Resonator Formation

As a counter measure for the afore-mentioned problems, investigations for optimization of the dry etching using a different mask material were performed. According to [3] and [6], the resulting sidewall inclination angle is directly influenced by the original mask sidewall profile and the selectivity of the mask material to the etched material. Nickel was chosen as it possesses a higher selectivity to GaN than SiO_2 with the respective values of 18 and 6 [7]. Hence, it is more etch resistant and can generate higher slopes of the etched facet. Additionally, nickel has a lower sputter yield in comparison to amorphous SiO_2 due to the different material structure and chemistry. This reduces the effects of grass as well as mask facetting. Thus the necessary mask thickness during dry etching can be reduced. Finally, process sensitivities during RIE are reduced leading to a higher degree of reproducibility.

First, we investigated a nickel film of 100 nm thickness for an etch time of 20 minutes using a graphite substrate holder (as the formerly used quartz holder proved to contribute to further grass formation [5]). Indeed, now the formation of grass pillars was completely suppressed at the etched n-GaN layer (Fig. 6 left). Additionally, the generated profiles were characterized by relatively smooth facet surfaces (Fig. 6 right).

We thus investigated an alternative mirror processing sequence using nickel as a dry etch mask. Moreover, it should exhibit a lower degree of RIE process sensitivities (such as fluctuations in substrate temperature or reactor pressure) and impose less limitations for other critical steps (such as oxide stripe etching) [5]. The new processing sequence involved the use of a double dry etch mask of nickel on top of sputter deposited SiO_2. The latter was deposited in a structured manner allowing for an already open oxide stripe (thus eliminating the need for an extra processing step). The generated laser facets were characterized by an average angle of 79 to 80 ° (Fig. 7 left). Nevertheless, laser action was achieved. A detailed description for the steps of our new suggested processing sequence

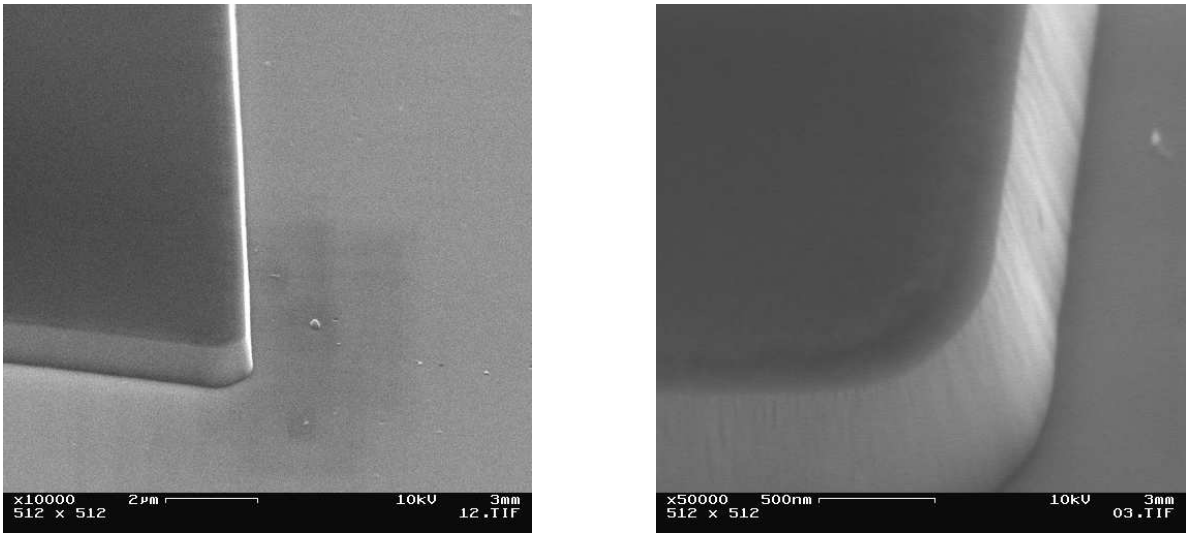

Fig. 6: Clean n-GaN surfaces (left) and smooth etched sidewalls (right) after the use of nickel as a mask material with a graphite plate.

can be found in [5].

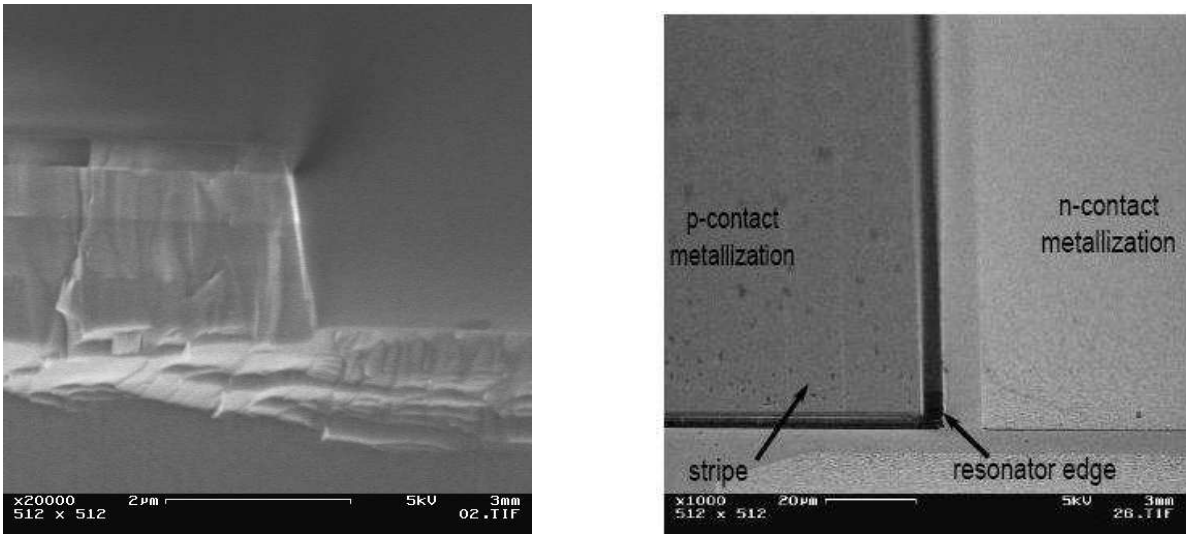

Fig. 7: Sidewall inclination of the resonator edges (angle 79-80 °) (left). SEM image of a complete fabricated device (right).

Contact formation for the n-contact was achieved for a metal stack of Ti/Al/Ni/Au with thicknesses of 15, 220, 40 and 50 nm, respectively, annealed in a nitrogen environment at 500 °C for 5 minutes. The resulting contact resistivity (ρ_c) was evaluated to be $9 \times 10^{-6}\,\Omega\text{cm}^2$ using the Circular Transmission Line Method model for contact characterization [8]. P-contact optimization was achieved using a metallization scheme involving a 20 nm palladium layer followed by a 100 nm gold layer, where the optimized alloying parameters are the same as for the n-contact. The resulting p-contact resistivity was calculated to be $1 \times 10^{-3}\,\Omega\text{cm}^2$. Furthermore, an additional gold cap layer of 800 nm

was evaporated after annealing for better current conduction. A SEM picture of a fully processed device is depicted in Fig. 7 (right).

5. Characterization

Measurements involving current-voltage (I-V) and power-current (P-I) characteristics for the laser device were undergone using pulsed current injection at a pulse width of 100 ns (Fig. 8). We measured a threshold current density of 6.1 kA/cm^2 and a voltage at threshold of 10 V. Measurements took place on wafer, where no direct non-obstructed light paths from the facet to the detector existed. Moreover, the aforementioned characterization values where recorded without any mirror coatings. Spectral analysis under stimulated emission revealed a peak wavelength of 393 nm (Fig. 9).

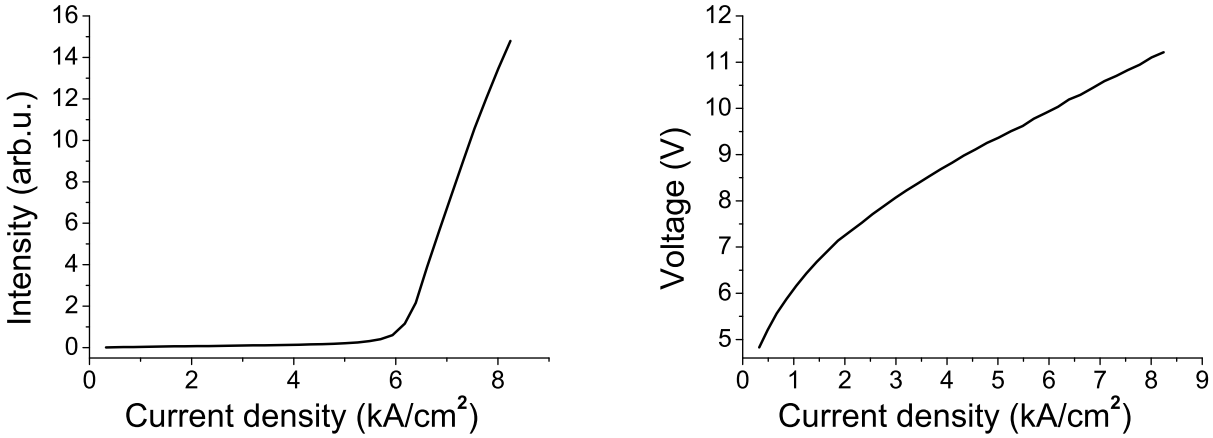

Fig. 8: Scaled optical power (per facet) vs current density (Left). Measured voltage-current characteristics for the laser device (Right). Stripe length: 800 µm. Stripe width: 12 µm. Pulse frequency: 10 kHz.

6. Conclusion

A number of problems characterizing the use of SiO_2 as dry etch mask for mirror formation in a GaN based oxide stripe laser diode have been studied. The use of nickel has proven to eliminate appearance of grass pillars and to reveal smooth etched feature. The final sidewall angle of 79 to 80 ° revealed a threshold current density of 6.1 kA/cm^2 under pulsed operation.

7. Acknowledgments

We would gratefully acknowledge the cooperation of M.Sc. H.C. Xu for his introductory training with the fabrication tools and his previous work on the same topic, Dipl.-Ing. W. Schwarz for his help with sputter coating, Mr. R. Rösch for his help with RIE and Ms. S. Menzel for her help with experiments involving wet etching.

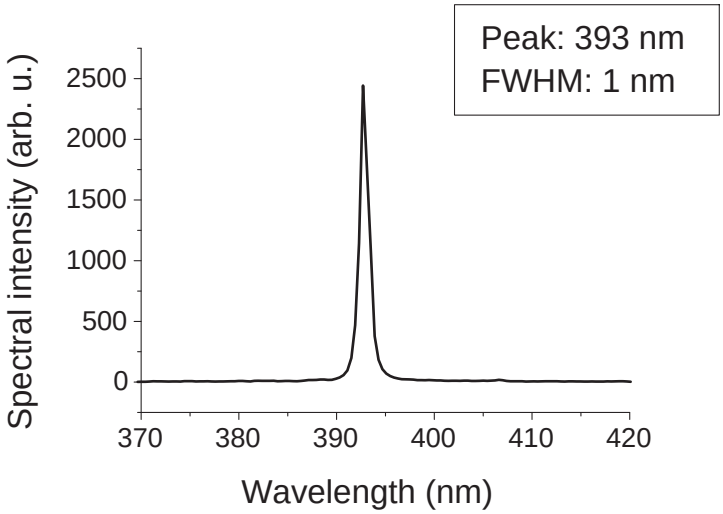

Fig. 9: Spectral analysis under stimulated emission for the laser device.

References

[1] S. Nakamura. "Laser Diodes", *Optoelectronic properties of semiconductors and superlattices*, Vol. 7, *GaN and Related Materials II*, Stephan J. Pearton (Ed.) pp. 1–44, 2000.

[2] H.Z. Xiao, N.E. Lee, R.C. Powell, Z. Ma, L.J. Chou, L.H. Allen, J.E. Greene and A. Rockett, "Defect ordering in epitaxial α-GaN(0001)" *J. Appl. Phys.* vol. 76, no. 12, 1994.

[3] M.J. Madou. *Fundamentals of Microfabrication: The Science of Miniaturization*, (2nd ed.), 2002.

[4] J. Hertkorn, P. Brueckner, S.B. Thapa, T. Wunderer, F. Scholz, M. Feneberg, K. Thonke, R. Sauer, M. Beer and J. Zweck. "Optimzation of nucleation and buffer layer growth for improved GaN quality", *J. Crystal Growth*, vol. 308, pp. 30–36, 2007.

[5] M. Fikry, *Epitaxy and processing of AlGaInN heterostructures for light emitting diode applications*. Master thesis, Institute of Optoelectronics, University of Ulm, August 2008.

[6] H.C. Xu. *Investigations of RIE processing for the controlled characterization of optoelectronic properties of nitride based devices*. Master thesis, Institute of Optoelectronics, University of Ulm, August 2007.

[7] M. Dineen. Oxford Instruments Ltd. Private communication, 2007.

[8] A. Weimar, A. Lell, G. Bruederl, S. Bader and V. Haerle. "Investigations of Low-Resistance Metal Contacts on p-Type GaN using the Linear and Circular Transmission Line Method", *phys. stat. sol. (a)* vol. 183, no. 169, 2001.

Epitaxial Growth of ZnO-GaN Hetero-Nanorods and GaN Nanotubes

S. B. Thapa, F. Scholz†

We report about the successful realization of a coaxial hetero structure grown by MOVPE around ZnO nanocolumns. At higher overgrowth temperatures, the ZnO cores completely dissolved leaving GaN nanotube structures with excellent properties. Such tubes could be sheathed by a GaInN-GaN single quantum well structure, as confirmed by photoluminescence and transmission electron microscopy.

1. Introduction

Various methods to grow high quality and perfectly arranged ZnO nanorods have been reported over the recent years (see, e.g., [1, 2] and references therein). However, due to the material properties of ZnO and its related compounds, there are many restrictions in designing more complex heterostructures or even devices based on such nanorods. In particular p-type doping of ZnO is still a big, yet unsolved challenge. On the other hand, GaN and its related compounds, having similar band gap and lattice constant as ZnO, have been successfully used for the realization of a huge number of various devices owing to the fact that many issues related to heterostructures and to n- and p-type doping could be successfully solved. However, for this material class, the deposition of ordered low-dimensional structures like nanorods is very difficult, typically leading only to a very disordered growth of nanowires in contrast to the above mentioned highly ordered ZnO nanorod structures. Therefore, we have investigated the combination of these two material approaches by growing GaN epitaxially around ZnO nanorods. Similar studies have been reported by An et al. [3].

One significant obstacle for this approach is the high sensitivity of ZnO in GaN growth environment: At elevated temperatures, ZnO decomposes by reacting with hydrogen or ammonia (NH_3). Therefore, we have established a multi-layer growth process (MGP) based on our experience about the growth of GaN layers on ZnO templates by metalorganic vapor phase epitaxy (MOVPE) [4–6]. However, even then the ZnO may easily dissolve leaving GaN nanotubes on the wafer [7]. In the current studies, we investigated whether such nanotubes can be used as templates for coaxial GaInN quantum well structures.

†in cooperation with J. Hertkorn, T. Wunderer, F. Lipski (Institute of Optoelectronics, Ulm University), A. Reiser, Y. Xie, M. Feneberg, K. Thonke, R. Sauer (Institute of Semiconductor Physics, Ulm University), M. Dürrschnabel, L. D. Yao, D. Gerthsen (Laboratory for Electron Microscopy, University of Karlsruhe).

2. Experimental

The ZnO nanopillars used as templates in these studies have been grown catalyst-free by a vapor-solid process on a-plane sapphire wafers. This process started with a ZnO nanocrystal nucleation layer using zink acetate as precursor. The nanorods were deposited at 845°C with Ar as carrier gas following a carbo-thermal method [8]. We could achieve perfectly vertically aligned ZnO nanorods with good homogeneity (Fig. 1) with typical diameters and heights of 100 – 300 nm and 1 – 2 µm, respectively. They showed mostly perfect hexagonal shape with flat side facets. These templates have then been transferred to our AIXTRON AIX 200 RF low pressure (LP) MOVPE system. Here, the precursors were trimethylgallium (TMGa), and NH_3. The In containing layers including the adjacent GaN barrier layers have been grown in our 2nd MOVPE system in order to make use of the respective experience for the deposition of GaInN. The shape of the grown nanopillars was mainly investigated by scanning electron microscopy (SEM), whereas transmission electron microscopy (TEM) was applied to measure the dimensions of single rods and to evaluate the heterostructure details. Photoluminescence carried out at room and low temperature was applied to investigate the band gaps of the grown multi-layer nanostructures.

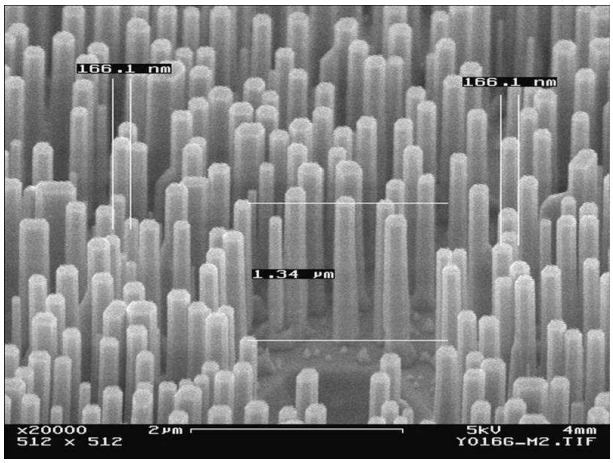

Fig. 1: ZnO nanorods grown on a-plane sapphire.

3. ZnO-GaN Coaxial Nanorods

Following our experience for the growth of GaN layers on ZnO templates [4,6], the growth was started with a low temperature covering layer of GaN grown at 550°C using N_2 as carrier gas to protect ZnO from being etched at the onset of the growth process. Then, the temperature was raised to 800°C, still using N_2 as a carrier gas. This resulted in a lightly yellow colored sample indicating that the grown GaN is not completely defect-free. SEM micrographs showed that the outer surface of the overgrown sheath layer of GaN is not as smooth as that of the original ZnO nanopillar. Low temperature photoluminescence spectra revealed a peak of ZnO with a GaN related shoulder (Fig. 2). From TEM images, the thickness of the GaN sheath was evaluated to be about 30 nm thick.

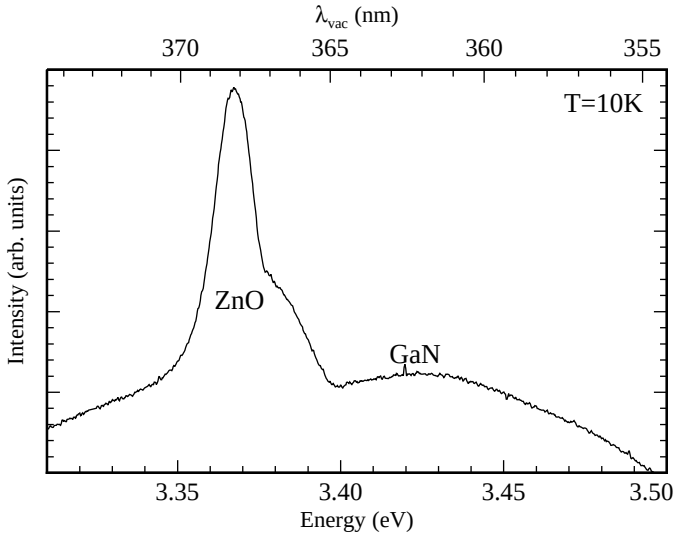

Fig. 2: Low temperature photoluminescence of GaN-ZnO coaxial nanorods.

4. GaN Nanotubes

In order to improve the GaN quality, we have investigated the sheathing growth at higher temperatures. After growing the thin GaN covering layer at 550°C, we deposited three thin intermediate layers of GaN at 800°C, 900°C, 1000°C, and finally a layer at 1050°C using H_2 as carrier gas. In contrast to the previous samples, the color of this sample was transparent white. The SEM micrograph (Fig. 3) shows very smooth well-defined facets of the structures. The top view (Fig. 3, right) reveals hollow tubes with large diameters. In low temperature PL, a sharp near-band-edge GaN related peak at around 3.47 eV without yellow band luminescence is observed (Fig. 4) demonstrating the high quality of the GaN crystal. Obviously, the ZnO nanopillar cores disappeared completely during the high temperature overgrowth leaving perfectly aligned GaN nanotubes. The latter still reflect the arrangement of the original ZnO nanopillars, which hence acted as templates for the GaN nanotubes. The wall thickness of the nanotubes was analyzed by transmission electron microscopy (TEM) to be about 40 nm. This thickness is fairly uniform along the full length of the tubes. It fits to the growth data taking into account the surface area of the tubes as compared to the areal size of a normal flat layer. High-resolution TEM images confirmed the high crystalline quality of the GaN tubes. Moreover, we could not find any evidence for remaining ZnO inside the tubes by EDX analysis in TEM.

5. Coaxial GaInN Quantum Well

As mentioned above, we then transferred the samples to our 2nd MOVPE machine for the deposition of a GaInN quantum well. Here, the growth was re-established by growing a thin GaN layer (about 7 nm) at 885°C with triethylgallium (TEGa) as Ga precursor and N_2 as carrier gas. Then, the trimethylindium (TMIn) flow was switched to the reactor to grow a GaInN quantum well with nominally about 10 % In at a temperature of 830°C.

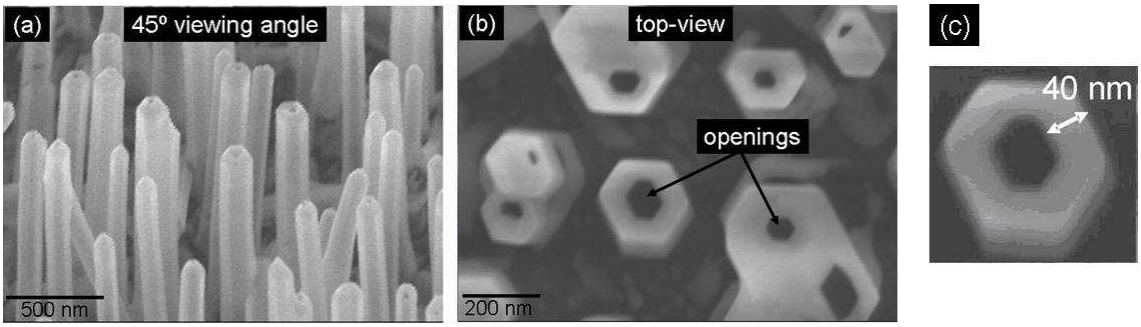

Fig. 3: GaN nanotubes grown around ZnO nanorods which dissolved during the MOVPE process: (a) bird eye's view, (b) top view, (c) determination of wall thickness.

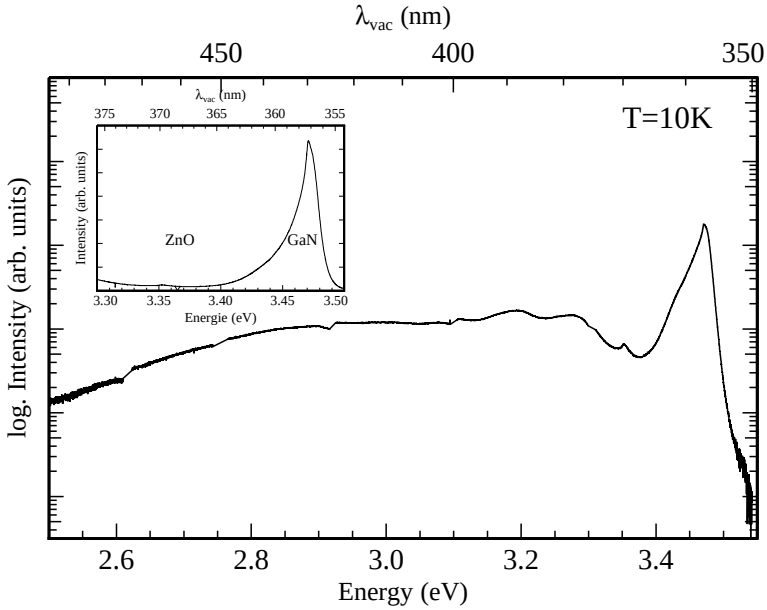

Fig. 4: Low temperature photoluminescence of GaN nanotubes.

Finally, the temperature was set back to 885°C for the growth of the outer GaN barrier layer under H_2 as carrier gas.

SEM inspection showed that the diameters of the nanotubes have significantly increased (Fig. 5). Obviously, most material was deposited at the top of the tubes, indicating a less pronounced precursor diffusion down to the template surface. This may be a consequence of the fairly densely packed nanotubes and of the lower diffusivity of TMIn and TEGa as compared to TMGa, being even further pronounced by the lower growth temperature.

In photoluminescence, we could determine a fairly sharp and intense peak at about 3 eV, the position expected for the GaInN quantum well (Fig. 6). This interpretation was confirmed by a local EDX analysis of the chemical composition in TEM (Fig. 7): No In can be found in spectrum (A), whereas (B) and (C) show a weak In signal. Moreover, the thicknesses of the inner GaN tube, the GaInN quantum well and the outer GaN barrier could be determined by high resolution TEM to be about 40 nm, 4 nm, and 20 nm, respectively.

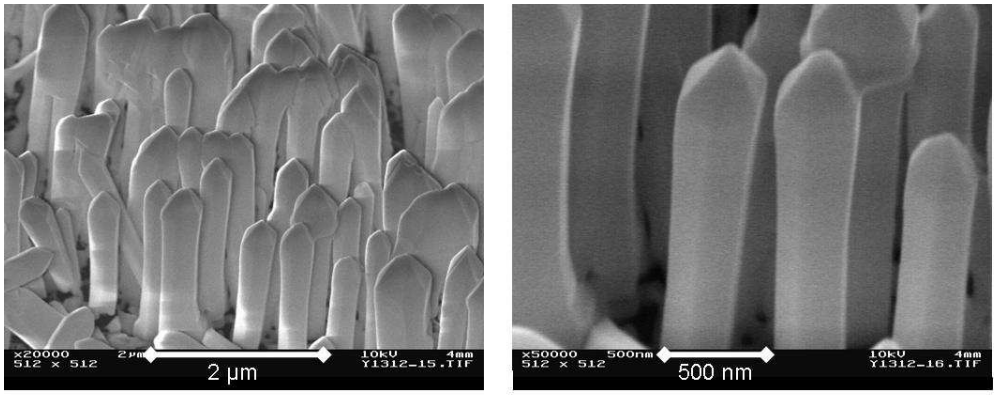

Fig. 5: GaInN GaN coaxial nanotube structures: Overview (left), close-up (right).

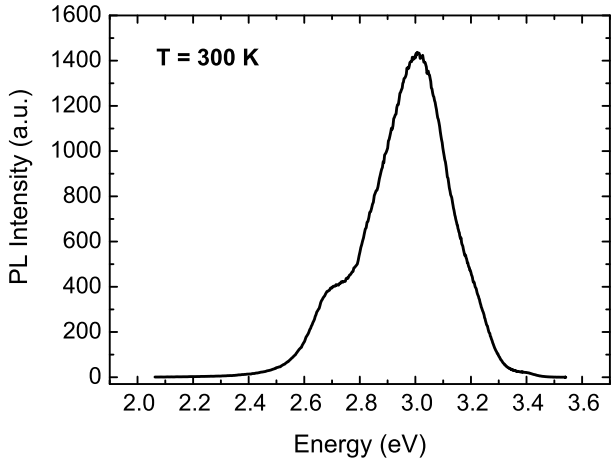

Fig. 6: Room temperature photoluminescence of GaInN GaN coaxial nanotube structures.

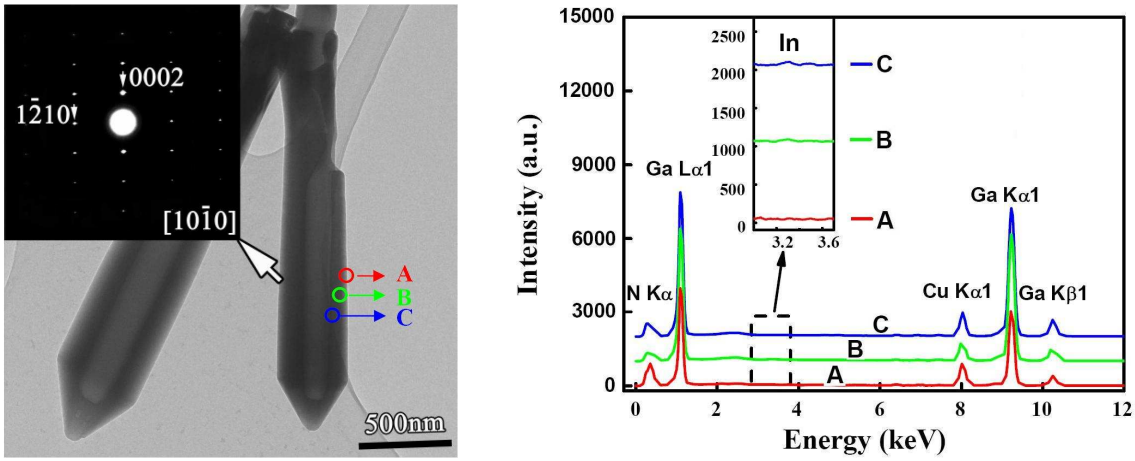

Fig. 7: TEM analysis (left) and related EDX analysis of a GaInN GaN coaxial nanotube structure. The inset (left) shows an electron diffraction signal taken along the [10$\bar{1}$0] zone axis of the nanocolumn confirming its crystalline character.

6. Summary

When growing GaN around ZnO nanocolumns by MOVPE at elevated temperatures, the ZnO core could completely be dissolved leaving well arranged GaN nanotubes. These tubes could be overgrown by a GaInN-GaN double hetero structure resulting in a coaxial GaInN quantum well of about 4 nm thickness. Photoluminescence and transmission electron microscopy studies confirmed the very good properties of these novel nanostructures.

References

[1] J.Y. Park, Y.S. Yun, Y.S. Hong, H. Oh, J.-J. Kim, and S.S. Kim, "Synthesis, electrical and photoresponse properties of vertically well-aligned and epitaxial ZnO nanorods on GaN-buffered sapphire substrates," *Appl. Phys. Lett.*, vol. 87, p. 123108, 2003.

[2] F.C. Tsao, J.Y. Chen, C.H. Kuo, G.C. Chi, C.J. Pan, P.J. Huang, C.J. Tun, B.J. Pong, T.H. Hsueh, C.Y. Chang, S.J. Pearton, and F. Ren, "Residual strain in ZnO nanowires grown by catalyst-free chemical vapor deposition on GaN/sapphire (0001)," *Appl. Phys. Lett.*, vol. 92, p. 203110, 2008.

[3] S.J. An and G.-C. Yi, "Near ultraviolet light emitting diode composed of n-GaN/ZnO coaxial nanorod heterostructures on a p-GaN layer," *Appl. Phys. Lett.*, vol. 91, p. 123109, 2007.

[4] S.B. Thapa, E. Angelopoulos, J. Hertkorn, F. Scholz, A. Reiser, K. Thonke, R. Sauer, H. Hochmuth, M. Lorenz, M. Grundmann, "Heteroepitaxial Growth of GaN on ZnO by MOVPE", poster at *12th European Workshop on MOVPE*, Bratislava, Slovakia, 2007.

[5] S.B. Thapa, J. Hertkorn, T. Wunderer, F. Lipski, F. Scholz, A. Reiser, Y. Xie, M. Feneberg, K. Thonke, R. Sauer, M. Dürrschnabel, L.D. Yao, D. Gerthsen, H. Hochmuth, M. Lorenz, and M. Grundmann, "MOVPE growth of GaN around ZnO nanopillars," *J. Cryst. Growth*, vol. 310, p. 5139, 2008.

[6] E. Angelopoulos, "Heteroepitaxial Growth of GaN on ZnO by MOVPE," master thesis, Universität Ulm, 2007.

[7] J. Goldberger, R. He, Y. Zhang, S. Lee, H. Yan, H.-J. Cho, and P. Yang, "Single-crystal gallium nitride nanotubes," *Nature*, vol. 422, p. 599, 2003.

[8] A. Reiser, A. Ladenburger, G.M. Prinz, M. Schirra, M. Feneberg, A. Langlois, R. Enchelmaier, Y. Li, R. Sauer, and K. Thonke, "Controlled catalytic growth and characterization of zinc oxide nanopillars on a-plane sapphire," *J. Appl. Phys.*, vol. 101, p. 054319, 2007.

Layer Design of Highly Efficient Optically Pumped Semiconductor Disk Lasers

Frank Demaria

A carefully elaborated layer design for optically pumped disk lasers is presented. Its goal is to achieve a high optical conversion efficiency by an effective pump light absorptance and an uniform supply of the multiple quantum wells with carriers generated in the surrounding barriers. Experimental results support the appropriateness of the described approach.

1. Introduction

Optically pumped semiconductor disk lasers (OPSDLs) with extended cavities are surface-emitting laser devices which efficiently convert the low-beam-quality emission of a pump laser to a high-beam-quality circular non-astigmatic laser emission. Furthermore, the extended cavity can be utilized for intra-cavity second harmonic generation by insertion of nonlinear optical crystals. By that way, the range of usable wavelengths is drastically expanded from the near infrared to the visible range of the optical spectrum [1–5].

Like in common semiconductor lasers, the gain of OPSDLs is provided by quantum wells. To obtain sufficient modal gain, in surface emitting lasers, multiple quantum wells are positioned in a way that supports a lasing field intensity with its antinodes as close as possible to the wells. This is usually realized by a periodical gain structure wherein a series of quantum wells is spaced at an optical distance of half the design wavelength [6]. The composition of the quantum wells ideally determines the peak-gain wavelength in laser operation which fits the design wavelength. Such a structure was also implemented in the pioneering OPSDLs of Kuznetsov et al. [7] where it was combined with an epitiaxially-grown back-side Bragg reflector having its stopband centered near the emission wavelength. However, without any further design features, the carrier generation rate in the barriers of the lower quantum wells of such a single-pass pump-light-absorbing structure suffers from the decay of the pump intensity resulting from the absorption in the barriers of the upper quantum wells. This is unfavorable, as high optical conversion efficiencies and slope efficiencies require a uniform distribution of the carriers over the quantum wells [8]. One possible design strategy which can be pursued to overcome this is to separate the gain structure and the absorbing barriers into sections with unequal absorbing volumes and (or) an unequal number of quantum wells to establish approximately constant carrier generation per well [9]. Our approach which shall be described here is different. It consequently takes advantage from the implementation of a back-side double-band Bragg reflector (DBBR) which provides not only high reflectivity for the actual laser resonance but also for the incident pump beam. That way, in combination with the reflecting surface

interfaces of the laser chip, a Fabry-Pérot microcavity is established also for the pump light which supports high absorptance. This also leads to an uniform carrier distribution over the quantum wells and thus highest conversion efficiencies.

2. Layer Design

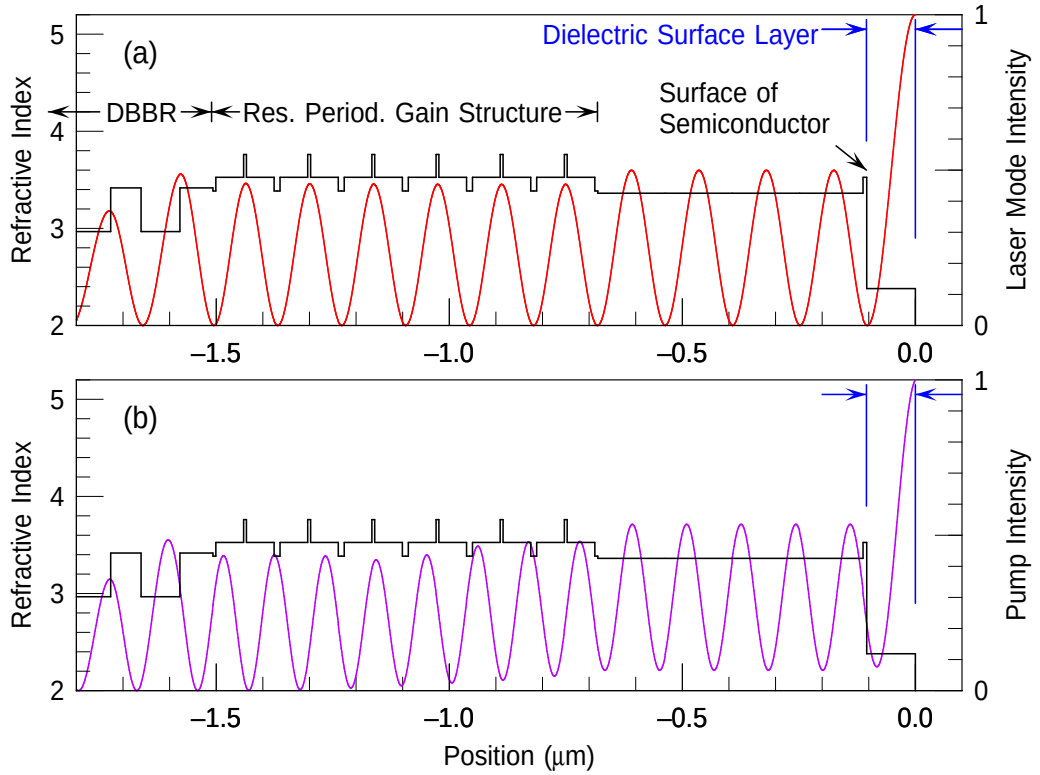

Fig. 1: Design of the top region of the semiconductor disk laser, visualized by the index of refraction, beginning from the surface layer on the right side to the first layers of the rear DBBR on the left. In (a), the electric field intensity for the design wavelength $\lambda_e = 980\,\text{nm}$ in case of perpendicular propagation is shown and in (b) for unpolarized pump radiation with a wavelength $\lambda_p = 808\,\text{nm}$ at an angle of incidence $\theta_i = 25°$.

Figure 1 shows the top region of a OPSDL layer structure, represented by the index of refraction. It is designed for an emission wavelength of $\lambda_e = 980\,\text{nm}$ and for pumping with a wavelength of $\lambda_p = 808\,\text{nm}$ under an angle of incidence $\theta_i = 25°$. The structure consists of the following functional regions:

- *Surface Layer:* The semiconductor structure is covered by a dielectric TiO_2 coating with the optical thickness of $\lambda_e/4$.
- *Resonant Periodic Gain (RPG) Structure:* Six 6.2 nm-thick $In_{0.155}Ga_{0.845}As$–GaAs quantum wells are arranged at a distance that corresponds to an optical thickness of $\lambda_e/2$. Strain compensation is realized by $GaAs_{0.74}P_{0.26}$ layers which are located at a central position between the QWs and at the boundaries of the structure. These

layers have a higher bandgap as the surrounding barriers and therefore also act as carrier diffusion barriers.

- *Rear Reflector:* 66 epitaxially-grown layers build up the double-band Bragg reflector which is supported by the rear metallization. The structure is numerically optimized to provide high reflectivity at the emission wavelength as well as for the pump light. The spectral reflectivity function which is shown in Fig. 2 was calculated by the matrix formulation for isotropic layered media and monochromatic plane waves [11].

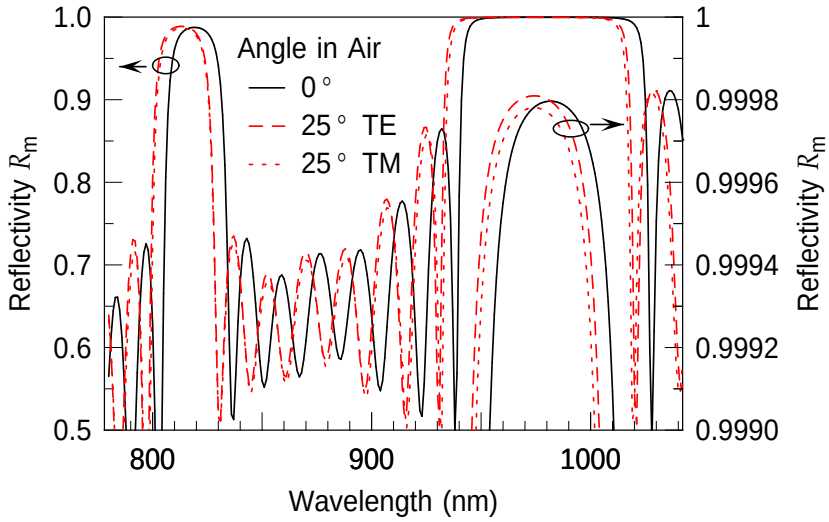

Fig. 2: Calculated internal reflectivities of the DBBR in combination with the rear metalization for normal incidence ($\theta_i = 0°$) and an incidence angle of $\theta_i = 25\,°$.

The dielectric surface layer results in a reflectivity of 6 % at 980 nm and 8 % for unpolarized 808 nm pump radiation at an incident angle of $\theta_i = 25°$. Hence, an internal cavity with a length of few microns is established in combination with the DBBR for both the pump and emission wavelength. On the wavelength scale of the internal cavity's Fabry-Pérot resonances, the mode spectrum of the extended cavity becomes quasi-continuous because the distance of the external mirror exceeds the internal cavity length by an order of at least three magnitudes. For this reason the influence of the extended cavity on the field distribution of the resonant laser mode can be neglected, even though in principle a three-mirror cavity has to be considered. The emitting resonance in Fig. 1 (a) shows antinodes at the QW positions and at the surface of the structure. The surface of the semiconductor is located at the interface to the dielectric surface layer at $x \approx$-0.105 µm, where a node of the field is located.

Also, the pump resonance in Fig. 1 (b) exhibits a minimum close to the semiconductor surface which leads to a reduced absorption in that region. This design strategy was also applied to a disk laser which was designed for direct pumping of the QWs and led to high efficient emission at wavelengths around 860 nm [12]. Unlike the emitting resonance, the standing wave pattern of the resonant pump intensity is significantly superimposed by a ground level, which decreases towards the DBBR. This is due to the fraction of pump

energy which is absorbed in the QWs and the surrounding barriers. However, compared to single-pass pump light absorbing structures, the contribution of the periodic fraction which is built up by the resonant reflection at the DBBR and the surface layer of the structure is much higher and results in a much more homogeneous pumping of the QWs. The efficient and homogeneous supply of the QWs with carriers that are generated in the barriers by the pump intensity is also supported by the high-bandgap strain compensation layers which are located in the center between the QWs and at the edges of the RPG structure. They define a clear direction of the longitudinal diffusion and confine the absorbing volume which provides the embedded QW with carriers. The thickness of the absorbing volume equals the distance between two QWs reduced by the thickness of the strain compensation layers, thereby it is adapted to the periodicity of the pump intensity distribution. The overall carrier generation rate of the absorbing volume which supports one QW is approximately proportional to the integral of the pump intensity distribution over its thickness. This results in a decoupling of the pump rate and the phase of the periodic fraction of the pump field for a single QW since the definite integral over one period is independent from the position of the maximum within the boundaries.

3. Device Fabrication and Mounting

The layer structure has been grown by molecular beam epitaxy on GaAs substrate. The direction of growth is reverse to the laser emission. Hence, the wafer structure ends with the DBBR on top. On top of the DBBR, a metalization layer is applied for proper soldering and reflectivity enhancement. To facilitate the fabrication of laser chips with a size of $1.2 \times 1.7\,\mathrm{mm}^2$ by cleaving, the substrate is thinned to a thickness of approximately $140\,\mu\mathrm{m}$ by wet chemical polishing. The chips are then bonded upside-down onto 3-mm-thick gold-plated copper heat spreaders or with 0.3-mm-thick diamond heat spreaders onto microchannel heat sinks for water cooling [10]. This approach allows entire substrate removal and efficient heat extraction by extra-cavity heat spreaders. After the residual substrate has been removed by selective wet chemical etching, the surface layer is applied by ion-beam sputter depositionin a final fabrication step.

4. Reflectivity Spectra

Valuable information on the performance of layer designs and realized OPSDL structures can be extracted from calculated and measured reflectivity spectra. Also, the performance of isolated components of the structure can be calculated to support a modular construction approach. An example is given by the reflectivity spectrum of an isolated DBBR in Fig. 2. It also shows clearly how the spectral characteristics is shifted towards shorter wavelengths for an increasing angle of incidence. This has to be considered as the angle of the incident pump beam differs from the direction of emission at large.

Reflectivity spectra of a whole OPSDL structure are shown in Fig. 3, for an incidence angle $\theta_\mathrm{i} = 5\,^\circ$ at room temperature. For comparison measured and calculated curves are plotted. The calculations where performed for different wavelength ranges by the same method as for the rear reflector in Fig. 2.

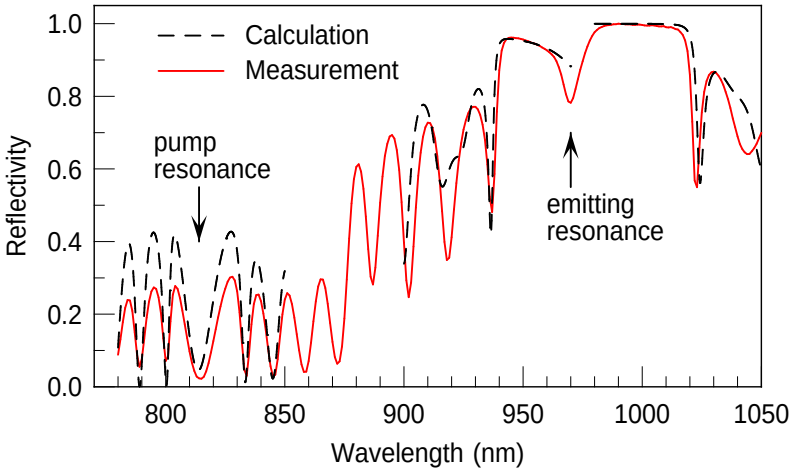

Fig. 3: Measured and calculated reflectivity spectra of the whole structure at an incidence angle $\theta_i = 5\,°$.

For 780–850 nm, a constant absorption coefficient of 9500 cm^{-1} is assumed for the QWs and the surrounding barriers as well as 9000 cm^{-1} for the 8 nm-thick GaAs anti-oxidation layer. For 900–970 nm only the QWs have been taken into account with an absorption of 6800 cm^{-1}. Above 980 nm no absorption is considered. The mentioned values have been extracted from the graphical representation of gain calculations, performed by Corzine et al. [13].

Both, measurement and calculation reveal distinct dips at the labeled positions at 813 nm and 970 nm which originate from resonant absorption in the laser's Fabry-Pérot microcavity. Often, within the long wavelength stop-band, two different reflectivity dips can be distinguished, originating from the resonance of the microcavity and the absorption peak of the QWs which is related to the gain peak in laser operation [3, 14]. Here, both peaks overlap at room temperature giving evidence that the resonance of the microcavity and the maximum of the gain spectrum are matched.

For an incident angle of about 25 °, the pump resonance shifts to a value that equals the pump wavelength of about 808 nm. By means of adjusting the angle of incidence, absorptance values up to 96 % have been achieved for 805 nm pump wavelength with 3 nm linewidth (10 dB drop). Comparison with Fig. 2 shows that the pump resonance is located in the center of the short wavelength stopband where maximum reflectivity is provided. Hence the absorption of the pump light takes place nearly exclusively in the designated regions, which are rather the QWs and their surrounding barriers than the metalization underneath the DBBR.

5. Output Characteristics

The output power and absorption characteristics of the device with the reflectivity spectrum presented in Fig. 3 are shown in Fig. 4. In this case the laser chip was mounted on a water-cooled microchannel heat sink with a 0.3 mm-thick diamond heat spreader in between. An extended cavity with a simple hemispherical resonator configuration was

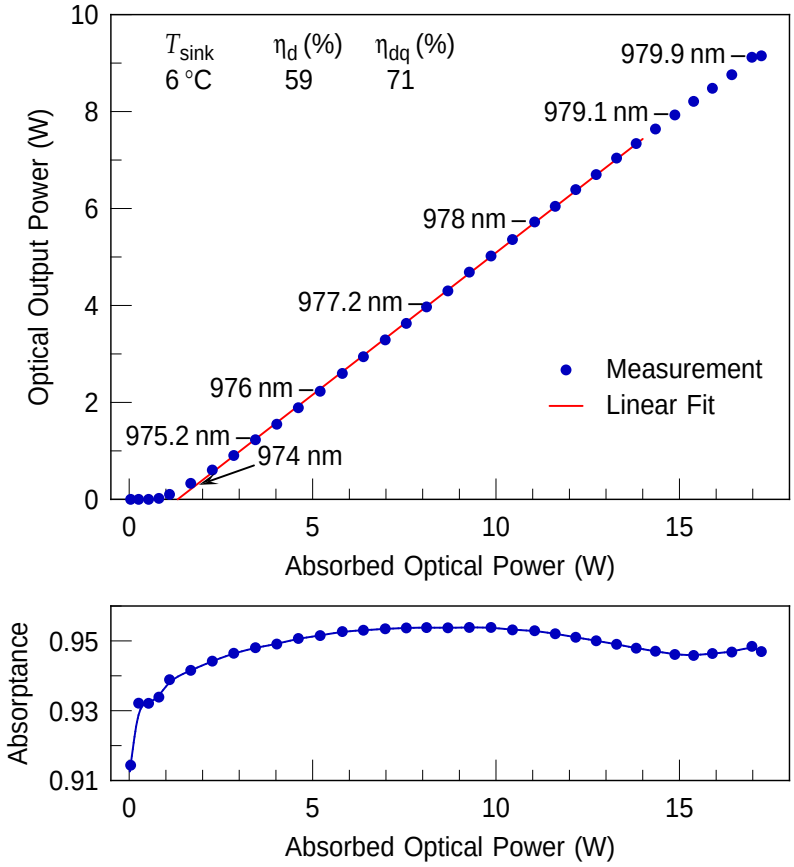

Fig. 4: The upper graph shows the measured output characteristics versus absorbed pump power of the laser device with the reflectivity spectrum shown in Fig. 3. The related absorption efficiency is shown in the lower graph. To achieve sufficient cooling, the laser chip is mounted on a water cooled microchannel heat sink with a 0.3 mm-thick diamond heat spreader and a temperature of the cooling water T_{sink}. Also shown are the extracted slope conversion efficiency η_d and the differential quantum efficiency η_{dq}. Some measurement points are labeled with the emission wavelength.

established by an external mirror of $R_c = 100$ mm radius of curvature and 3.6 % transmittance for the emission wavelength. The laser was pumped at an angle of 28 ° with a pump-spot area of 310 µm × 330 µm. With increasing pump power, the temperature of the OPSDL structure increases and therefore the reflectivity spectrum is displaced towards longer wavelengths. The maximum absorptance of over 95 % is achieved at a pump power of about 9 W for which the minimum of the Fabry-Pérot resonance dip of the microcavity overlaps with the pump wavelength of 808 nm. At an incident pump power of 17.9 W, a fraction of 17.2 W is absorbed and an optical power of 9.1 W is emitted. This corresponds to conversion efficiencies of 51 % and 53 %. From the linear fit of the curve a slope efficiency of 59 % can be extracted which corresponds to a differential quantum efficiency of 71 %. A similar structure which was mounted on simple gold-plated copper heat sinks led to an output power of 13.2 W at a heat sink temperature of -5 °C [15]. The related conversion efficiency is 54 % referred to the absorbed pump power and a differential quantum efficiency of 73 % has been achieved.

6. Conclusion

A layer design for OPSDLs that leads to optimized longitudinal field distributions of the resonantly pumped devices has been described. The approach is substantiated by experimental results from such devices which reveal the highest absorption efficiency, conversion efficiency, and differential quantum efficiencies which so far have been reported for OPSDLs to the best knowledge of the author.

References

[1] E. Schielen, M. Golling, and P. Unger, "Diode-pumped semiconductor disk laser with intracavity frequency doubling using lithium triborate (LBO)," *IEEE Photon. Technol. Lett.*, vol. 14, no. 6, pp. 777–779, 2005.

[2] E. Gerster, I. Ecker, S. Lorch, C. Hahn, S. Menzel, and P. Unger, "Orange-emitting frequency-doubled GaAsSb/GaAs semiconductor disk laser," *J. Appl. Phys.*, vol. 94, no. 12, pp. 7397–7401, 2003.

[3] J.-Y. Kim, S. Cho, J. Lee, G. B. Kim, S.-J. Lim, J. Yoo, K.-S. Kim, S.-M. Lee, J. Shim, T. Kim, and Y. Park, "A measurement of modal gain profile and its effect on the lasing performance in vertical-external-cavity surface-emitting lasers," *IEEE Photon. Technol. Lett.*, vol. 18, no. 23, pp. 2496–2498, 2006.

[4] J. Rautiainen, A. Härkönen, V.-M. Korpijärvi, P. Tuomisto, M. Guina, and O. G. Okhotnikov, "2.7 W tunable orange-red GaInNAs semiconductor disk laser," *Opt. Express*, vol. 15, no. 26, pp. 18 345–18 350, 2007.

[5] M. Fallahi, L. Fan, Y. Kaneda, C. Hessenius, J. Hader, H. Li, J. Moloney, B. Kunert, W. Stolz, S. Koch, J. Murray, and R. Bedford, "5-w yellow laser by intracavity frequency doubling of high-power vertical-external-cavity surface-emitting laser," *IEEE Photon. Technol. Lett.*, vol. 20, no. 20, pp. 1700–1702, 2008.

[6] M. Y. A. Raja, S. R. J. Brueck, M. Osiński, C. F. Schaus, J. G. McInerney, T. N. Brennan, and B. E. Hammons, "Resonant periodic gain surface-emitting semiconductor lasers," *IEEE J. Quantum Electron.* **25**, pp. 1500–1512, 1989.

[7] M. Kuznetsov, F. Hakimi, R. Sprague, and A. Mooradian, "High-power >0.5-W cw diode-pumped vertical-external-cavity surface-emitting semiconductor lasers with circular TEM_{00} beams," *IEEE Photon. Technol. Lett.*, vol. 9, no. 8, pp. 1063–1065, 1997.

[8] O. Casel, *Experimentelle Untersuchung und Modellierung des Einflusses der Epitaxiestruktur auf die physikalischen Eigenschaften optisch angeregter Halbleiterscheibenlaser.* Ph.D. thesis, University of Kaiserslautern, Göttingen: Culliver, 2005.

[9] S. Giet, H.D. Sun, S. Calvez, M.D. Dawson, S. Suomalainen, A. Harkonen, M. Guina, O. Okhotnikov, and M. Pessa, "Spectral narrowing and locking of a vertical-external-cavity surface-emitting laser using an intracavity volume Bragg grating," *IEEE Photon. Technol. Lett.*, vol. 18, no. 16, pp. 1786–1788, 2006.

[10] E. Gerster, "Semiconductor Disk Laser on Microchannel Cooler," *Annual Report 2004*, pp. 79–84, Ulm University, Institute of Optoelectronics.

[11] P. Yeh, *Optical Waves in Layered Media*, John Wiley & Sons, 1988.

[12] S.-S. Beyertt, F. Demaria, U. Brauch, N. Dhidah, A. Giesen, T. Kübler, S. Lorch, F. Rinaldi, and P. Unger, "Efficient gallium-arsenide disk laser," *IEEE J. Quantum Electron.*, vol. 43, no. 10, pp. 869–875, 2007.

[13] S. W. Corzine, R.-Y. Yan, and L. A. Coldren, "Optical gain in III-V bulk and quantum well semiconducors," in P. S. Zory, Jr. (Editor), *Quantum Well Lasers, Quantum Electronics–Principles and Appications*, Academic Press Inc., San Diego, 1993.

[14] S. Cho, G. B. Kim, J.-Y. Kim, K.-S. Kim, S.-M. Lee, J. Yoo, T. Kim, and Y. Park, "Compact and efficient green VECSEL based on novel optical end-pumping scheme," *IEEE Photon. Technol. Lett.*, vol. 19, no. 17, pp. 1325–1327, 2007.

[15] F. Demaria, S. Lorch, S. Menzel, M. C. Riedl, F. Rinaldi, R. Rösch, and P. Unger, "Design of highly-efficient high-power optically-pumped semiconductor disk lasers," accepted for publication in *IEEE J. Select. Topics Quantum Electron*, May/June, 2009.

Development of VCSELs for Atomic Clock Applications

Dietmar Wahl, Daniel Steffen Setz, and Ahmed Al-Samaneh

This article describes the process of transferring an 850 nm VCSEL structure to devices emitting at 895 nm, a wavelength required for cesium-based atomic clocks. We discuss all the effects to be considered and present photoluminescence measurements of the modified quantum well structure. In addition, the influence of δ-doping in distributed Bragg reflectors on VCSEL characteristics, namely threshold current, maximum output power, and differential quantum efficiency, is investigated.

1. Introduction

The miniaturization of classical atomic clocks is limited by the size of the microwave resonator. The only way to achieve a further volume reduction is to move to a clock concept which does not rely on such a resonator. Concepts of miniaturized atomic clocks (MACs) based on the effect of *coherent population trapping* (CPT) have been discussed since 1993 [1] and demonstrated in the last few years [2]. The effect of CPT is based on the quantum mechanical phenomenon that the population probability of the highest energy level in a three-level system can be drastically reduced if the atom is illuminated by two coherent light sources whose emission wavelengths match the transition energies between the two lower states and the upper state [3]. A gas of atoms in this condition shows reduced absorption or increased transparency, therefore this phenomenon is also called *electromagnetically induced transparency*. Normally two separate lasers are used to achieve this effect. If the energy levels of the two lower states are very close, it is also possible to produce light with the two required wavelengths by modulating a single laser source with a frequency that corresponds to half of the energy gap between the two lower states. One then makes use of the modulation sidebands.

Vertical-cavity surface-emitting lasers (VCSELs) are of great interest for this application because of various reasons. The most important advantages of VCSELs for MAC applications are the excellent modulation capability (up to more than 10 GHz), high temperature stability, and the small power consumption of just a few mW. For a MAC, the same gases as in classical atomic clocks, namely Rb and Cs, are favored, requiring laser wavelengths of 780 nm (Rb D_2 transition), 795 nm (Rb D_1), 852 nm (Cs D_2), or 895 nm (Cs D_1) [4]. In what follows we will focus on Cs-based clocks. Because of a higher figure of merit, the D_1 transition is preferred [5]. VCSELs emitting at the required wavelength of 895 nm can be easily produced with the well-known InGaAs/AlGaAs material system. An application in MACs presumes polarization-stable laser sources which can also be fulfilled by VCSELs. Devices with monolithic surface gratings for polarization control have been recently demonstrated and investigated [6].

2. Transferring a VCSEL Design From 850 to 895 nm

In order to fabricate VCSELs with a wavelength of 895 nm for MAC applications, there are some subjects to consider if, like in our case, a design for a different wavelength already exists.

Firstly the quantum well structure in the active region of the laser has to be adjusted in a way that the energy level of the ground state of the quantum well fits to the new emission wavelength. Because the desired wavelength is larger than the wavelength corresponding to the bandgap energy of GaAs, the AlGaAs material system used so far has to be expanded by introducing indium into the quantum wells in order to achieve a reduction of the bandgap energy. In contrast to the nearly lattice-matched growth of AlGaAs, InGaAs grown on GaAs is compressively strained. This has to be considered for calculations as well as the effect of bandgap renormalization which is a many-body effect and depends on the carrier density. Finally also the influence of the band offset of the InGaAs/AlGaAs junction has to be regarded. Calculations of the quantum well energy levels for a well width of 8 nm and a barrier material of $Al_{0.27}Ga_{0.73}As$ result in a required indium content of 6 % for achieving the desired emission wavelength of 895 nm.

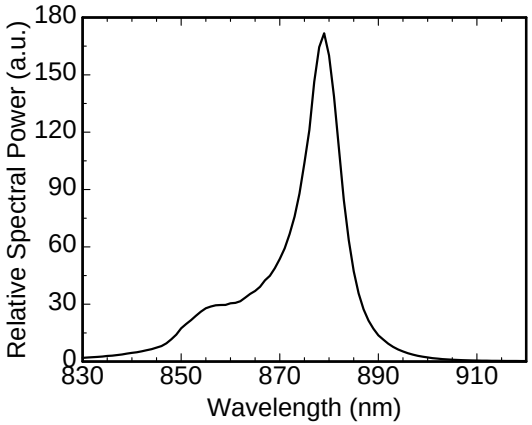

Fig. 1: Photoluminescence spectrum of an $In_{0.06}Ga_{0.94}As/Al_{0.27}Ga_{0.73}As$ quantum well, taken at room temperature.

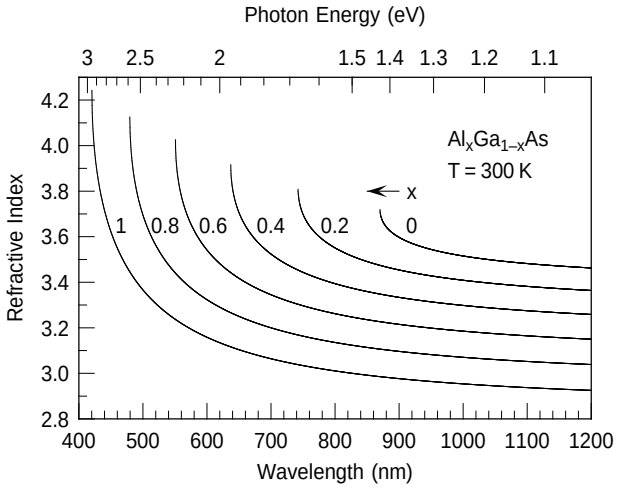

Fig. 2: Refractive index of $Al_xGa_{1-x}As$ in dependence of the aluminum concentration x and the wavelength.

In order to check the emission wavelength of the designed quantum well structure, a sample with several $In_{0.06}Ga_{0.94}As/Al_{0.27}Ga_{0.73}As$ quantum wells was grown by molecular beam epitaxy (MBE). Figure 1 depicts the photoluminescence (PL) spectrum of this sample, obtained at room temperature. The intensity maximum is found at a wavelength of 879 nm. At first glance this seems to be too small for the target wavelength of 895 nm. However, one has to consider that the carrier density in a laser is some orders of magnitude larger than that in PL experiments. For typical carrier densities in a lasing VCSEL, the effect of bandgap renormalization red-shifts the emission wavelength by about 15 nm. So, under lasing conditions, a quantum well structure like in this sample leads to an emission wavelength in the desired wavelength range.

The second step of redesigning the device is the adjustment of the layer thicknesses so that, for instance, one period of a Bragg mirror remains one half of the target wavelength in the material. The thicknesses of all layers have to be increased because of two effects: the longer wavelength itself and the reduced refractive index (Fig. 2).

Figure 3 depicts the light–current–voltage characteristics of a fabricated VCSEL with an active diameter of 4.4 µm after the above-mentioned adjustments have been made. Its threshold current is lower than 0.5 mA. The spectrum of this VCSEL operating in continuous-wave mode at a current of 2.38 mA is illustrated in Fig. 4. The fundamental transverse mode is lasing at 894.6 nm, which is the required emission wavelength for Cs-based MACs. A higher-order transverse mode is located on the short-wavelengths side with a side-mode suppression ratio of more than 25 dB, which is high enough for the present application.

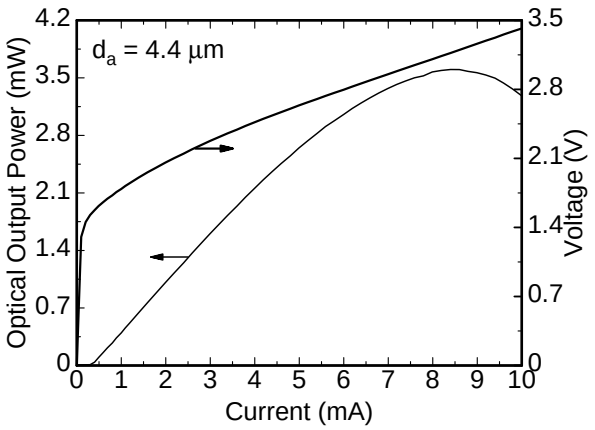

Fig. 3: Operation characteristics of an 895 nm VCSEL with 4.4 µm active diameter.

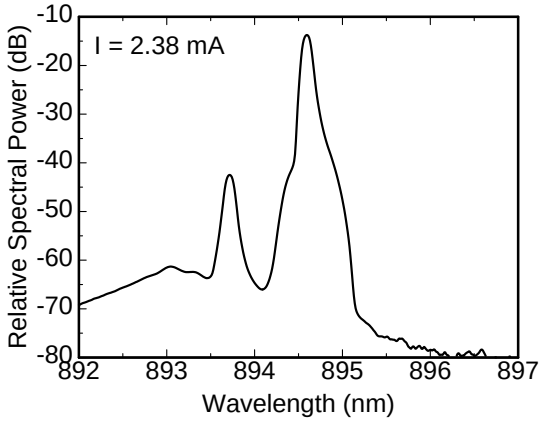

Fig. 4: Spectrum of the VCSEL from Fig. 3 at 2.38 mA current and $T = 300$ K ambient temperature.

3. Investigations Into δ-Doping of Distributed Bragg Reflectors

3.1 Composition of DBRs in VCSELs

Distributed Bragg reflectors (DBRs) of VCSELs contain several periods of layers, each of them having a thickness of half the material wavelength of the laser emission. In each period the aluminum composition of AlGaAs layers changes between low and high values in order to create a refractive index profile which gives a high reflectivity. Figure 5 shows such an aluminum composition profile of a Bragg mirror for an 895 nm VCSEL and the position of the δ-doping. The δ-doping is incorporated into the rising slope of the energy profile of the DBR (referring to the flow direction of the corresponding carriers) to reduce the ohmic resistance of the mirror.

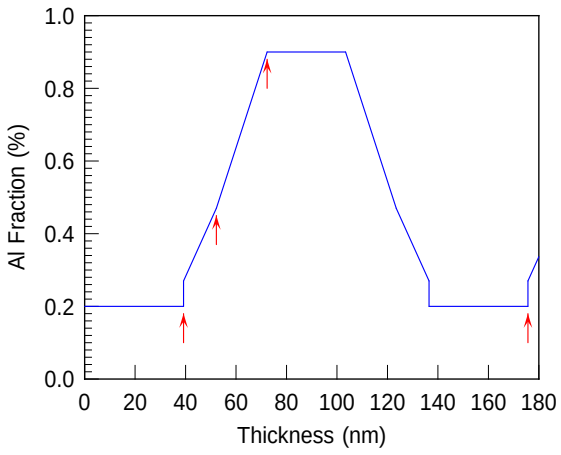

Fig. 5: Al composition profile of a Bragg mirror period. The vertical arrows indicate the positions of δ-doping.

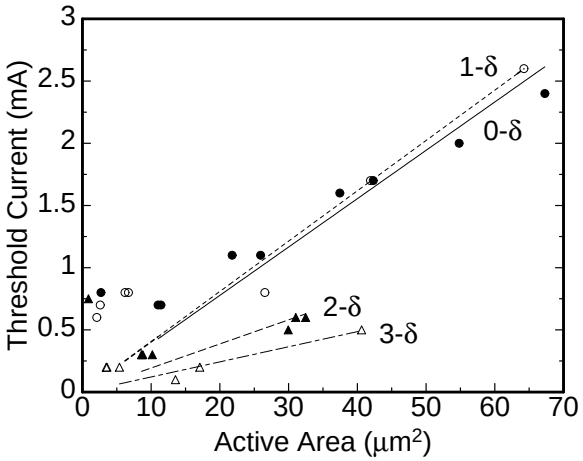

Fig. 6: Threshold current over the active area for the four investigated samples.

3.2 Influence on the electrical and optical properties

In order to investigate the influence of δ-doping in the DBRs on the laser properties, samples with different levels of δ-doping were grown by molecular beam epitaxy. All parameters except the doping level of the δ-doping were held constant within the investigated sample series. Samples without δ-doping and doping levels of 1×, 2×, and 3× a reference level of $1 \cdot 10^{12}\,\mathrm{cm}^{-2}$ for n-type material and $2 \cdot 10^{12}\,\mathrm{cm}^{-2}$ for p-type material were produced. Processing into oxide-confined VCSELs after epitaxial growth involves mesa etching, oxidation of the current aperture, and metallization of the electric contacts. The VCSELs were tested "on-wafer" without separation, i.e., all measurements were performed by contacting the lasers using contact needles. The examined parameters are threshold current, maximum output power, and differential quantum efficiency.

Concerning the threshold current in dependence of the active area, the samples without and with normal δ-doping concentrations show nearly the same behavior, as can be noticed from Fig. 6. With 2-δ concentration, the threshold current decreases drastically, and even a further reduction was achieved by tripling the doping level. The maximum output powers plotted in Fig. 7 versus the active diameter show only small deviations with variations in the δ-doping level. Highest output powers are achieved with double δ-doping concentration. No δ-doping and normal δ-doping devices show nearly the same lowest output power characteristics. The behavior of 3-δ VCSELs having a lower maximum output power than the optimum case might be due to increased optical losses induced by the higher doping concentration. As for the threshold current and output power, the differential quantum efficiencies of 0-δ and 1-δ samples show no big difference. As noticable in Fig. 8, they are nearly constant at a value of 37 % for a wide range of active diameters. Double-δ VCSELs have the highest efficiencies of more than 40 %, increasing with active diameter. This behavior is even enhanced in the 3-δ sample, as indicated by the higher slope in Fig. 8. Depending on the active size, the efficiency can be smaller than that of the low-doped samples or exceed 40 %.

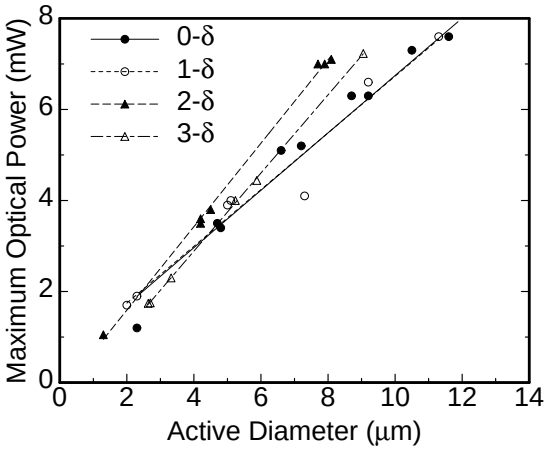

Fig. 7: Maximum VCSEL output power over the active diameter for all samples.

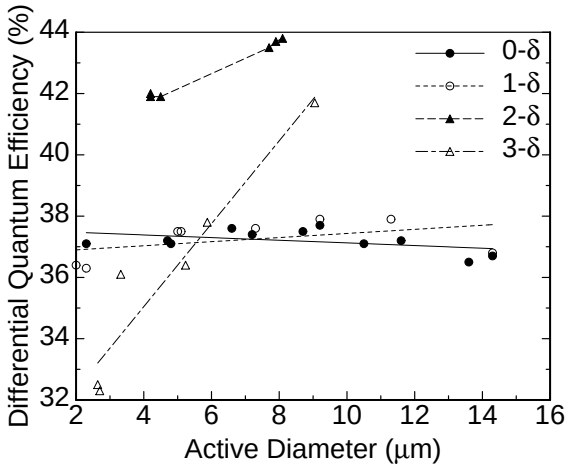

Fig. 8: Differential quantum efficiencies of the VCSELs from Fig. 7.

4. Conclusion

The transfer of an 850 nm VCSEL design to a wavelength of 895 nm has been achieved by introducing indium into the quantum wells to adjust the emission wavelength and by scaling all layer thicknesses to the new wavelength. Despite the small amount of indium in the active region, VCSELs for MAC applications can be produced within the well-known and well-controllable AlGaAs material system. First generation 895 nm wavelength VCSELs were presented to show the feasibility of this approach.

The investigation of the effect of δ-doping in the DBRs reveals that samples with no δ-doping and samples doped with the reference value show nearly no difference in threshold current, maximum output power, and differential quantum efficiency. If the level of δ-doping is doubled, the threshold current strongly decreases and higher maximum output powers as well as higher differential quantum efficiencies are achieved. For tripled δ-doping concentration, the results show inconsistent behavior. Although the threshold current is further decreased, the maximum output powers fall below those of the double-doped sample. A large variation of differential quantum efficiency with active diameter is obtained. In particular, the efficiency is drastically reduced for VCSELs with small active diameter. It seems that a doubling of the δ-doping concentration in the Bragg mirrors brings advantages to the VCSEL characteristics, however, increasing the concentration beyond this value appears not to be beneficial for future optimizations of VCSELs. Since the investigated 895 nm samples are conceptually identical to conventional 850 nm VCSELs, the results can also be transferred to other wavelengths.

Acknowledgments

We sincerely thank Fernando Rinaldi for his help with the quantum mechanical calculations and general advice as well as Susanne Menzel and Rudolf Rösch for their help with processing and metallization of the samples.

References

[1] N. Cyr, M. Têtu, and M. Breton, "All-optical microwave frequency standard: a proposal", *IEEE Transactions on Instrumentation and Measurement*, vol. 42, no. 2, pp. 640–649, 1993.

[2] S. Knappe, V. Shah, P.D.D. Schwindt, L. Hollberg, and J. Kitching, "A microfabricated atomic clock", *Appl. Phys. Lett.*, vol. 85, no. 9, pp. 1460–1462, 2004.

[3] E. Arimondo and G. Orriols, "Nonabsorbing atomic coherences by coherent two-photon transitions in a three-level optical pumping", *Lettere al nuovo cimento*, vol. 17, no. 10, pp. 333–338, 1976.

[4] D.K. Serkland, G.M. Peake, K.M. Geib, R. Lutwak, R.M. Garvey, M. Varghese, and M. Mescher, "VCSELs for atomic clocks", in Vertical-Cavity Surface-Emitting Lasers X, C. Lei, K.D. Choquette (Eds.), Proc. SPIE 6132, pp. 613208-1–11, 2006.

[5] R. Lutwak, D. Emmons, T. English, W. Riley, A. Duwel, M. Varghese, D.K. Serkland, and G.M. Peake, "The chip-scale atomic clock – recent development progress", in Proc. *35th Annual Precise Time and Time Interval (PTTI) Meeting*, pp. 467–478. San Diego, CA, USA, Dec. 2003.

[6] R. Michalzik, J.M. Ostermann, and P. Debernardi, "Polarization-stable monolithic VCSELs" (invited), in Vertical-Cavity Surface-Emitting Lasers XII, C. Lei, J.K. Guenter (Eds.), Proc. SPIE 6908, pp. 69080A-1–16, 2008

Single Transverse Mode VCSELs with High Output Power Emitting in the 980 nm Wavelength Range

Ihab Kardosh and Fernando Rinaldi

We report high single-mode output powers up to 15.0 mW from vertical-cavity surface-emitting lasers (VCSELs) with curved dielectric mirrors. The VCSELs are characterized on wafer under continuous-wave operation at room temperature and show average beam quality factors $M^2 \approx 1.7$.

1. Introduction

In recent years, vertical-cavity surface-emitting lasers (VCSELs) operating in a single transverse mode have gained a growing interest in many optical fields like spectroscopy, imaging and sensing. Usually, to achieve single-mode emission in conventional oxide-confined VCSELs, the active diameter is typically scaled down to a few micrometers ($\leq 4\,\mu$m) which limits the optical output power. Furthermore, small devices suffer from ohmic heating and high current densities and thus a reduction in lifetime. Several approches including coupled resonators [1], surface etching [2], [3], and Zn-diffusion [4] have been demonstrated to control and stabilize the transverse mode emission in large ($> 4\,\mu$m) oxide-confined VCSELs. However, the maximum output power from 850 nm VCSELs is 7.5 mW with a side-mode suppression ratio of 30 dB [3]. One successful approach towards higher power is the use of an extended cavity configuration with a dielectric micromirror. Single-mode output powers of 5 mW have been achieved from monolithic 980-nm VCSELs with flat mirrors on GaAs substrates [5]. Hybrid integration of curved micromirrors on glass substrates with 980-nm VCSELs mounted on AlN heatsinks has been demonstrated with single-mode output powers of about 7 mW [6]. In this article, we present a method for the fabrication of compact vertical extended-cavity surface-emitting lasers with monolithic integration of dielectric distributed Bragg reflector (DBR) micromirrors, which is suited for wafer-scale fabrication. The single-mode bottom-emitting VCSELs have up to 15.0 mW output power in the 980 nm wavelength range.

2. Device Structure and Design

The VCSEL structures are grown by solid-source molecular beam epitaxy on a semi-insulating (SI) GaAs substrate and are designed for emission wavelengths near 980 nm. The active region contains two stacks of three 8 nm thick InGaAs/GaAs quantum wells (with half-wavelength distance) surrounded by two 30 nm thick GaAsP layers for strain compensation. The active diameter is defined by selective oxidation of a 30 nm thick AlAs

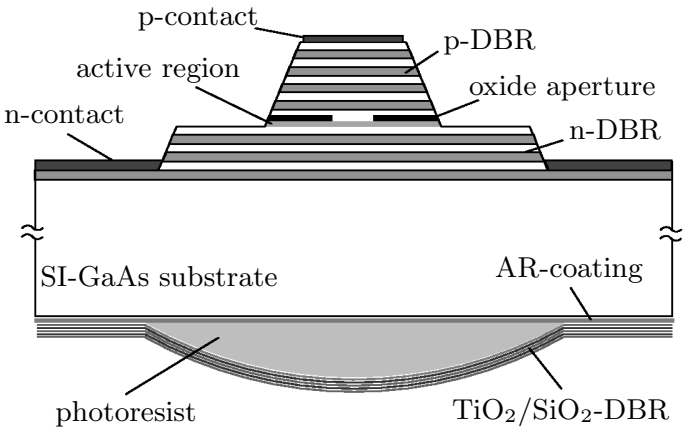

Fig. 1: Schematic cross-section of the monolithically integrated VCSEL.

layer above the active region, located in a node of the standing-wave pattern. The VCSEL contains a 30 pairs p-doped DBR and a 3 pairs n-doped DBR for wavelength selection. A schematic cross-section of the device is shown in Fig. 1. The spherical shape of the photoresist surface is designed to fit the radius of curvature R of the output beam which is calculated as

$$R = \frac{n_2}{n_1} L \left[1 + \left(\frac{Z_\mathrm{R}}{L} \right)^2 \right] \text{ with } Z_\mathrm{R} = \frac{\pi W_0^2 n_1}{M^2 \lambda} \tag{1}$$

additionally considering the refractive indexes $n_1 = 3.52$ and $n_2 = 1.53$ of GaAs and photoresist, respectively. Z_R is the Rayleigh length, L the substrate thickness, W_0 the radius of the beam waist, λ the vacuum wavelength and M^2 the beam quality factor. To avoid beam clipping, the diameter of the micromirror should be larger than the output beam diameter. In case of an extended cavity length of 150 µm, the Rayleigh length of the fabricated devices approximately ranges from L to $3L$ depending on W_0, hence the beam diameter at the output mirror is not much larger than in the active region. The dielectric DBR consists of 9 layers of TiO_2 and SiO_2 which are deposited on the photoresist using an ion-beam sputter deposition system. The mirror is designed to provide a high reflectivity of 97 % near 970 nm wavelength.

3. Device Fabrication

The fabricated VCSELs are bottom emitters with circular p-type contacts on the top of the mesa and have active diameters from 9 to 16 µm. The semi-insulating substrate that is used to minimize the free-carrier optical loss demands the fabrication of intracavity n-contacts on the epitaxial side. Large-area n-metallization layers are evaporated on the partly etched n-DBR as illustrated in Fig. 1. The substrate is thinned to approximately 150 µm before depositing a TiO_2 anti-reflection (AR) coating. The curved micromirrors are fabricated by using a technology known from microlenses. Polyimide and PMGI photoresists have been used for microlens formation on GaAs substrates of 980 nm VCSELs for decreasing the beam divergence [7, 8]. We have chosen PMGI photoresist due to its optical transparency in the near infrared and its excellent reflow properties. The PMGI

is patterned into round disks using a two-step lithographical process, followed by thermal reflow at 290 °C that transforms the disks into spherical lenses. The radius of curvature of the lens depends on the diameter and the thickness of the initial disk. Microlens diameters from 100 to 150 µm are used, resulting in radii of curvature of about 0.8 to 2 mm.

4. Experimental Results and Discussions

The output characteristics of monolithically integrated VCSELs with different active diameters D_a are shown in Fig. 2.

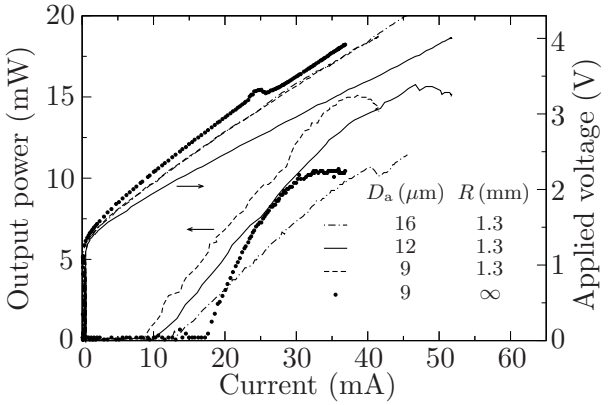

Fig. 2: Output characteristics of VCSELs with different active diameters D_a and radii of curvature R, measured on wafer at room temperature.

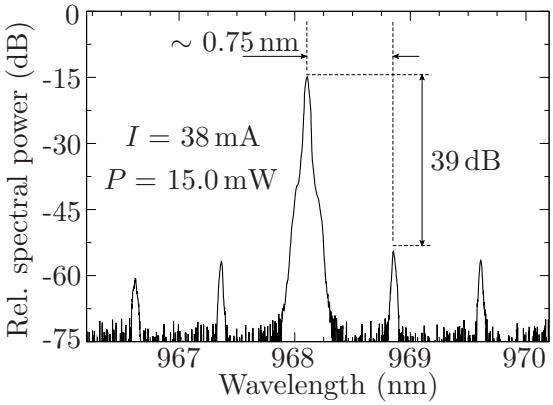

Fig. 3: Emission spectrum of the 9 µm diameter VCSEL ($R = 1.3$ mm) in Fig. 2 measured at 38 mA (15.0 mW).

The 9 µm diameter device ($R = 1.3$ mm) has a threshold current I_th of 7.5 mA and shows stable single transverse and longitudinal mode operation from threshold to rollover with a maximum single-mode output power $P_\mathrm{max,SM}$ of 15.0 mW and a side-mode suppression ratio of 39 dB, as evidenced by the optical spectrum in Fig. 3. The separation of 0.75 nm between the modes corresponds to the longitudinal mode spacing of a 150 µm long Fabry–Pérot resonator. All spectra were taken with a resolution of 0.01 nm. The ripples in the output curves, especially for small devices, can be attributed to laser heating, namely a varying temperature alters both the emission wavelength and the optical path length between the partial n-DBR and the dielectric mirror. In general, on-wafer measurements of bottom emitters induce strong device heating, owing to the lack of a direct contact with a heatsink. Almost all VCSELs with larger active diameter also exhibit single-mode operation, however, with higher threshold current and reduced differential quantum effeciency η_d, resulting in a lower output power compared to the 9 µm diameter device with the same radius of curvature. Independent of the device size, the VCSELs can show longitudinal multimode oscillation. In Fig. 2, this occurs mainly close to rollover. The small drop observed in the output power curve of the 16 µm diameter VCSEL is due to such a second mode which appears around 41 mA, as can be seen in Fig. 4 (right). In addition to the curved output mirrors, flat mirrors have also been fabricated.

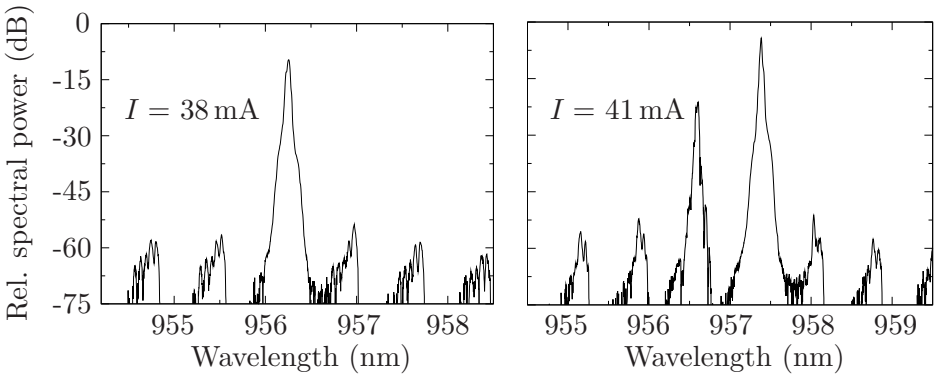

Fig. 4: Emission spectra of the 16 µm diameter device in Fig. 2 measured at 38 mA (left) and 41 mA (right). The transverse mode behavior of the longitudinal side modes is clearly observed.

The output characteristics of a 9 µm diameter device with a flat mirror ($R \to \infty$) are included in Fig. 2. The VCSEL shows single-mode emission but has a higher threshold current compared to the corresponding device with curved mirror. Increasing the radius of curvature decreases the optical feedback into the active region, which leads to higher threshold currents. Simultaneously, higher differential quantum efficiencies are observed. This behavior can be attributed to thermal lensing, which reduces the diffraction losses with increasing current. Experimental parameters of the VCSELs in Fig. 2 are listed in Table 1. In Fig. 5, calculated beam quality factors M^2 according to (1) are plotted against the radius of curvature of the output mirror. The symbols indicate averaged M^2 values obtained from beam quality measurements performed on several comparable single-mode devices. The observed range of M^2 can be attributed to beam waist diameters between 17 and 22 µm, as shown in Fig. 5, where thermal lensing is not considered. The beam profile of the 16 µm diameter device with $M^2 = 1.58$ is shown in Fig. 6. In general, VCSELs with small active diameters around 9 µm show stable single-mode operation with radii of curvature $\geq$ 0.8 mm. For active diameters of 16 µm or larger, radii of curvature $\geq$ 1.3 mm are required to obtain comparable beam quality factors and stable single-mode emission. The extended cavity length limits the maximum active diameter that allows single-mode emission. With increasing length of the extended cavity, a reduction of beam quality factors is expected from (1) for $L < n_1 R/(2n_2)$. For a 300 µm thick substrate, we have obtained average $M^2 = 1.5$ instead of 1.7 (with $L = 150$ µm) for comparable devices.

Table 1: Experimental parameters of VCSELs in Fig. 2.

D_a (µm)	I_{th} (mA)	$P_{max,SM}$ (mW)	η_d (%)	R (mm)
9	7.5	15.0	41	1.3
9	16.0	10.0	66	∞
12	10.2	13.9	40	1.3
16	12.3	10.0	32	1.3

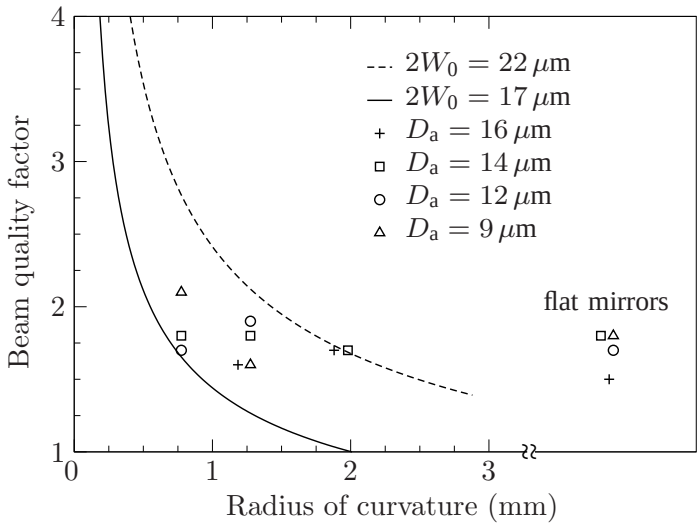

Fig. 5: Calculated beam quality factors versus the radius of curvature of the mirror for different beam waist diameters $2W_0$, where a substrate thickness of 150 µm and a wavelength of 965 nm are assumed. Measurement results obtained from various single-mode devices are shown as symbols.

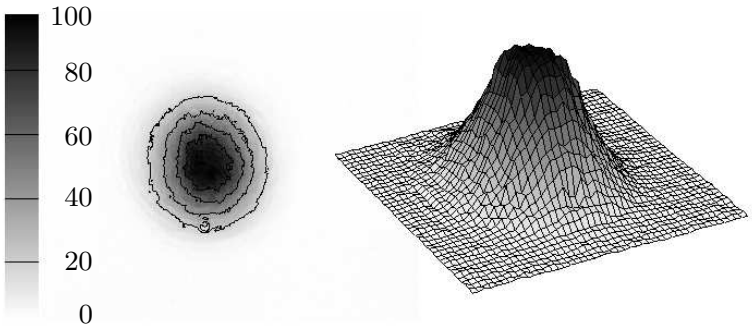

Fig. 6: Contour plot and three-dimensional plot of the beam profile of the 16 µm diameter VCSEL measured at 38 mA (10.0 mW) with $M^2 = 1.58$.

5. Conclusion

Monolithic integration of micromirrors with InGaAs VCSELs is demonstrated. The compact lasers operate at room temperature in a stable single mode with continuous wave output powers up to $P = 15.0$ mW. The combination of the epitaxial VCSEL cavity with the extended cavity allows the filtering of a single longitudinal mode together with fundamental transverse mode operation. Beam quality measurements yield an average M^2 of 1.7 and a radiance $P/(\lambda M^2)^2$ of more than 5×10^5 W/(cm^{2}sr). The structure and design presented here demonstrates the feasibility to realize single-mode VCSELs with maximum output powers exceeding those reported so far. Furthermore, the small device dimension is compatible with standard packaging. In an alternative approach which simplifies the device structure, the shape of the photoresist can be transformed into the substrate by applying an adequate dry-etching technique. Finally, we expect a higher performance with a more appropriate mounting technique that ensures efficient cooling.

References

[1] A.J. Fischer, K.D. Choquette, W.W. Chow, A.A. Allerman, D.K. Serkland, and K.M. Geib, "High single-mode power observed from a coupled-resonator vertical-cavity laser diode," *Appl. Phys. Lett.*, vol. 79, no. 25, pp. 4079–4081, Dec. 2001.

[2] A. Kroner, F. Rinaldi, J.M. Ostermann, and R. Michalzik, "High-performance single fundamental mode AlGaAs VCSELs with mode-selective mirror reflectivities," *Opt. Commun.*, vol. 270, no. 2, pp. 332–335, Feb. 2007.

[3] A. Furukawa, S. Sasaki, M. Hoshi, A. Matsuzono, K. Moritoh, and T. Baba, "High-power single-mode vertical-cavity surface-emitting lasers with triangular holey structure," *Appl. Phys. Lett.*, vol. 85, no. 22, pp. 5161–5163, Nov. 2004.

[4] J.-W. Shi, C.-C. Chen, Y.-S. Wu, S.-H. Guol, C. Kuo, and Y.-J. Yang, "High-power and high-speed Zn-diffusion single fundamental-mode vertical-cavity surface-emitting lasers at 850-nm wavelength," *IEEE Photon. Technol. Lett.*, vol. 20, no. 13, pp. 1121–1123, Jul. 2008.

[5] E.M. Strzelecka, J.G. McInerney, A. Mooradian, A. Lewis, A.V. Shchegrov, D. Lee, J.P. Watson, K.W. Kennedy, G.P. Carey, H. Zhou, W. Ha, B.D. Cantos, W.R. Hitchens, D.L. Heald, V.V. Doan, and K.L. Lear, "High power, high brightness 980 nm lasers based on the extended cavity surface emitting lasers concept," *Proc. SPIE*, vol. 4993, pp. 57–67, Jan. 2003.

[6] M.W. Wiemer, R.I. Aldaz, D.A.B. Miller, and J.S. Harris, "A single transverse-mode monolithically integrated long vertical-cavity surface-emitting laser," *IEEE Photon. Technol. Lett.*, vol. 17, no. 7, pp. 1366–1368, Jul. 2005.

[7] O. Blum, S.P. Kilcoyne, M.E. Warren, T.C. Du, K.L. Lear, R.P. Schneider, Jr., R.F. Carson, G. Robinson, and F.H. Peters, "Vertical-cavity surface-emitting lasers with integrated refractive microlenses," *Electron. Lett.*, vol. 31, no. 1, pp. 44–45, Jan. 1995.

[8] E.M. Strzelecka, G.D. Robinson, M.G. Peters, F.H. Peters, and L.A. Coldren, "Monolithic integration of vertical-cavity laser diodes with refractive GaAs microlenses," *Electron. Lett.*, vol. 31, no. 9, pp. 724–725, Apr. 1995.

A Fabrication Approach for Hybrid-Integrated Electrically Pumped VECSELs

Wolfgang Schwarz

We report on a fabrication approach for hybrid-integrated electrically pumped vertical-extended-cavity surface-emitting lasers (VECSELs). The fabrication involves parallel processing steps while maintaining reasonable alignment tolerances. An output power of more than 0.4 mW is achieved for an output coupler with a transmission of 5 %.

1. Introduction

Unlike a vertical-cavity surface-emitting laser (VCSEL), which comprises two highly reflecting distributed Bragg reflectors (DBRs), the extended cavity in VECSELs employs a third mirror. The fabrication of such a device requires a long process chain, including the patterning of the VCSEL structures, definition of the extended optical resonator, mirror coating and die bonding. While VCSELs have matured to be used in commonplace applications like optical computer mice necessitating volume production [1], products incorporating VECSELs are still rare.

Laborious and delicate steps like substrate removal reduce the process yield [2]. Wafer-scale approaches lack an economic utilization of the epitaxial material [3], because the electrical connections occupy valuable wafer area, whereas the demand for mass production prohibits any non-wafer-scale processing steps. The method presented here features a compromise between producibility and area efficiency.

2. Fabrication Steps

The cross-section of the complete device is depicted in Fig. 1. The extended plano-concave resonator consists of the VCSEL DBR, an air gap, the glass substrate and the curved surface of the microlens with a second DBR mirror. The fabrication of the VECSELs includes four steps, which are in the proper order: (i) fabrication of top-emitting VCSELs with solder bumps, (ii) patterning of fanout tracks and microlenses on the anti-reflection coated glass substrate, (iii) flip-chip solder connection of the latter with the VCSEL, and (iv) coating of the microlenses with the DBR.

The available GaAs/AlGaAs-based top-emitting VCSELs have a dominant emission wavelength which ranges from 785 to 830 nm due to a layer thickness gradient within the wafer sample. The VCSELs employ optical and carrier confinement by a thin AlAs layer which is selectively oxidized in water vapor. The resulting apertures range from 6 to 20 µm.

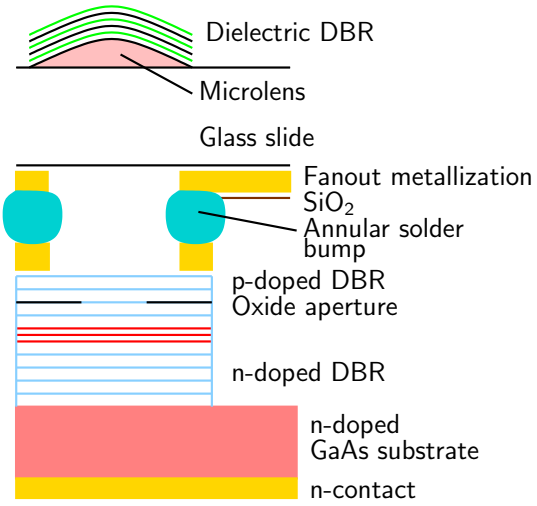

Fig. 1: Schematic cross-sectional view of the VECSEL.

The top mirror is thick enough to support laser emission without any extended resonator. On each annular p-contact on top of the mesas, a 4 µm thick ring-shaped indium solder bump is deposited. The indium facilitates both electrical connection and mechanical self-alignment during the soldering process. The extended cavity consists of a 100 µm thick boron-doped glass slide which is anti-reflection coated on one side. As illustrated in Fig. 2 (left), the measured reflectivity of this surface is less than 0.1 % in the wavelength range from 780 to 840 nm. The coated side is metallized with the fanout tracks and 180 nm thick SiO_2 is selectively deposited on the areas where wetting of the solder is undesired. The neccessary radii of curvature r_c were calculated by the transfer-matrix method [4]. Assuming no volume loss during reflow, the lens diameter D can be calculated from

$$D = \sqrt{(6t + r_c)\sqrt{9r_c^2 - 6tr_c + 9t^2} - 6r_c^2 - 18t^2}$$

with t being the photoresist thickness. Too small apertures of the microlens or the annular ring contact would result in beam aberrations due to beam cutoff. For this reason, the aperture diameter was chosen at least 3.4 times the beam diameter. Under this condition, the aperture loss is expected to be less than 1 %, assuming a circular Gaussian beam. The microlenses are made from Microchem PMGI SF17 photoresist which is reflown at 360 °C, resulting in radii of curvature between 100 and 2800 µm. The high transparency of the glass substrate allows checking the alignment under a light-optical microscope. The measurement with an atomic force microscope reveals a smooth surface of the lens, as shown in Fig. 2 (right). The surface can be fitted to a general sphere according to $(x/\varrho_x)^2 + (y/\varrho_y)^2 + (z/\varrho_z)^2 = 1$ with radii of curvature $\varrho_x = 102.9\,\mu m$, $\varrho_y = 103.3\,\mu m$, and $\varrho_z = 103.1\,\mu m$.

After a coarse pre-alignment using a silicon CCD camera, the VCSEL and extended cavity parts are solder-joined in a formic acid saturated atmosphere. The peak temperature in this step is critical and is approximately 170 °C in order to suppress the formation of indium whiskers and diffusion of indium into the fanout. In a final step, 3.5 pairs of TiO_2/SiO_2 are deposited on the microlenses by ion beam sputter deposition using 1 keV energy argon ions. The DBR transmits about 5 % of the incident light at the operation wavelength.

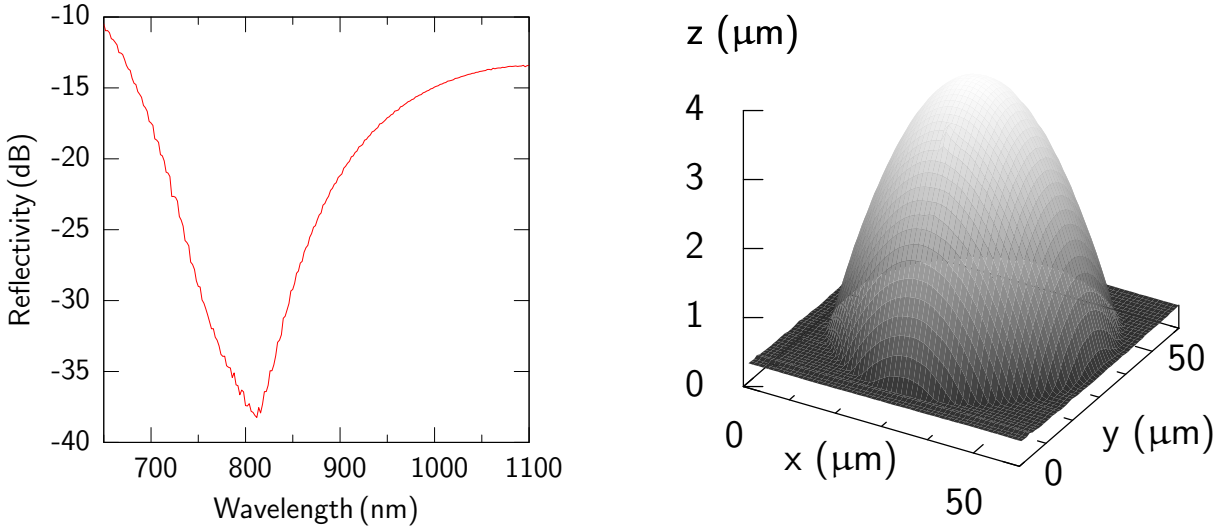

Fig. 2: Measured reflectivity spectrum of a four-layer anti-reflection coated glass slide (left) and surface topology of a microlens aquired by atomic force microscopy (right).

3. Characterization of the VECSELs

The processed VCSELs show smooth light–current–voltage (LIV) characteristics. As depicted in Fig. 3, the threshold current I_{th} of a reference device with 10 µm active diameter is 6.8 mA, whereas the threshold currents of all fabricated VECSELs (Fig. 4) are lower by 10 to 20 %. The LI characteristics of the VECSELs show multiple kinks, which can be attributed to transverse or longitudinal mode hops. The maximum output power of more than 400 µW corresponds to an incident power of 8 mW on the output coupler, which is much more than in the VCSEL. This is a clear indication that light is oscillating in the extended resonator, however, the quality factor of this resonator is lower than expected. A possible reason could be an improper alignment of the extended cavity or losses induced by the GaAs cap layer on the VCSEL surface. The differential electrical resistance R_{d} of the VCSELs and VECSELs is less than 150 Ω.

4. Conclusion

We have successfully introduced a fabrication approach for electrically pumped VECSELs. It supports wafer-scale processing while making efficient use of the wafer surface. A process yield of 75 % was achieved. The function of the extended cavity was demonstrated, but the quality of the external resonance is still to be improved. A possible way to minimize the losses in the extended cavity could be a shift in emission wavelength above 850 nm which would result in a suppression of fundamental absorption in the GaAs cap layer. In future work, the loss mechanism could be studied in lasers with a thinner p-doped DBR which allows better coupling of the generated light into the extended cavity.

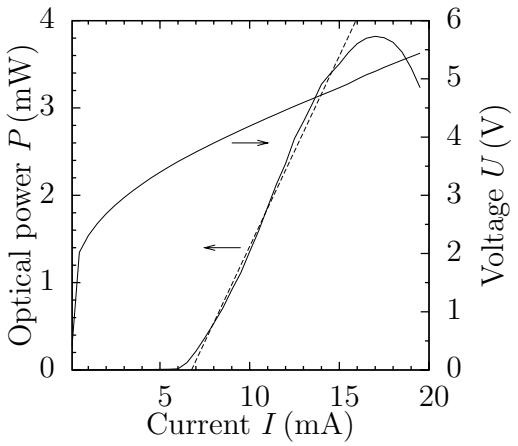

Fig. 3: LIV characteristics of a 10 µm active diameter reference VCSEL.

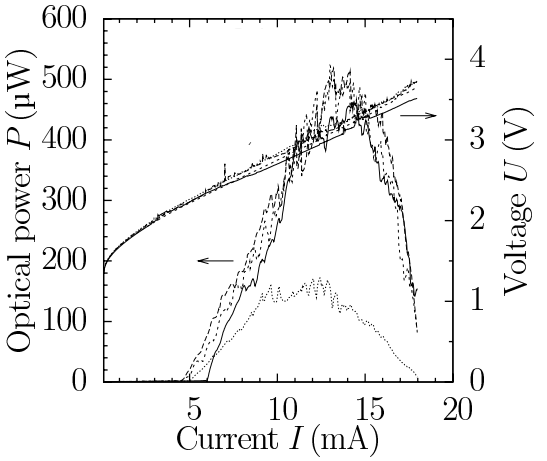

Fig. 4: LIV characteristics of several VECSELs with 10 µm active diameter. The devices differ in the radius of curvature of the microlens.

Acknowledgments

The author would like to thank Ahmed Al-Samaneh and Dieter Rimpf for their help with the processing. Their many contributions are much appreciated. The author would like to express his sincere thanks to Matthias Wiora and Arnaud Caron from the Institute of Micro and Nanomaterials, Ulm University, and Manuel Rodriguez Gonçalves from the Institute of Experimental Physics, Ulm University, for fruitful discussions and the atomic force microscopical measurements.

References

[1] M. Grabherr, R. King, R. Jäger, D. Wiedenmann, P. Gerlach, D. Duckeck, and C. Wimmer, "Volume production of polarization controlled single-mode VCSELs," in *Vertical-Cavity Surface-Emitting Lasers XII,* C. Lei and J.K. Guenter (Eds.), Proc. SPIE 6908, pp. 690803-1–8, 2008.

[2] L.A. Coldren, E.M. Strzelecka, B.J. Thibeault, and D.A. Louderback, "Flip-chip bonded VCSELs with integrated microlenses for free-space optical interconnects," in Proc. *IEEE Lasers and Electro-Opt. Soc. Ann. Meet., LEOS 1997*, vol. 1, pp. 343–344. San Francisco, CA, USA, Nov. 1997.

[3] G.A. Keeler, D.K. Serkland, K.M. Geib, G.M. Peake, and A. Mar, "Single transverse mode operation of electrically pumped vertical-external-cavity surface-emitting lasers with micromirrors," *IEEE Photon. Technol. Lett.*, vol. 17, pp. 522–524, 2005.

[4] B.E.A. Saleh and M.C. Teich, *Fundamentals of Photonics*. New York, NY, USA: John Wiley & Sons, Inc., 1991.

Investigations into Matrix-Addressable VCSEL Arrays

A. Gadallah

We report on fabrication and characterization of densely packed top-emitting 16×16 *elements wire-bonded matrix-addressable vertical-cavity surface-emitting laser (VCSEL) arrays, which may find future applications such as non-mechanical particle movement with optical multi-tweezers, confocal microscopy or free-space communications with beam steering capability. The factors that control packing density such as layer structure, mask design and VCSEL processing are investigated aiming to minimize the pitch between VCSELs in the array.*

1. Introduction

The impressive performance of VCSELs such as low power consumption, circular beam output perpendicular to the wafer surface, on-wafer testing before packaging, and efficient high-frequency modulation is providing the motivation for a continued search for new device types. Besides, VCSELs are ideally suited to form two-dimensional arrays of compact optical sources owing to their low threshold currents and high packing density. Such two-dimensional VCSEL arrays are attractive for display technology [1], [2], optical scanners [3], optical interconnects and confocal microscopy. All of these applications require convenient addressing of VCSELs in these arrays. In order to allow operation with high packing density, it is important to decrease the number of contact pads required to address the elements in the array. Figure 1 shows how the elements in 4×4 two- dimensional arrays can be addressed using two different architectures. It becomes clear that individual addressing requires a lot of metallic traces. This increases the connection complexity and limits the packing density compared with the matrix addressing scheme. Matrix addressing [4] has the advantage of requiring only $M + N$ contact pads for an $M \times N$ element array, unlike its individually addressable counterpart, which requires $M \times N$ contacts. In addition, when such arrays are monolithically integrated with resonant-cavity photodetectors [5], this will enable a variety of applications such as high-density interconnects, position sensors, and imaging devices. A recent trend in VCSEL arrays is to obtain a coherent laser emission by utilizing photonic crystal VCSELs [6]– [10] as a way to increase the emitted power from a single transverse mode.

This article is organized as follows: In Sect. 2, the layer structure needed to fabricate the laser elements in the array is described. In Sect. 3, the processing is explained and discussed. In Sect. 4, the laser characteristics are evaluated. Finally conclusions are made in Sect. 5.

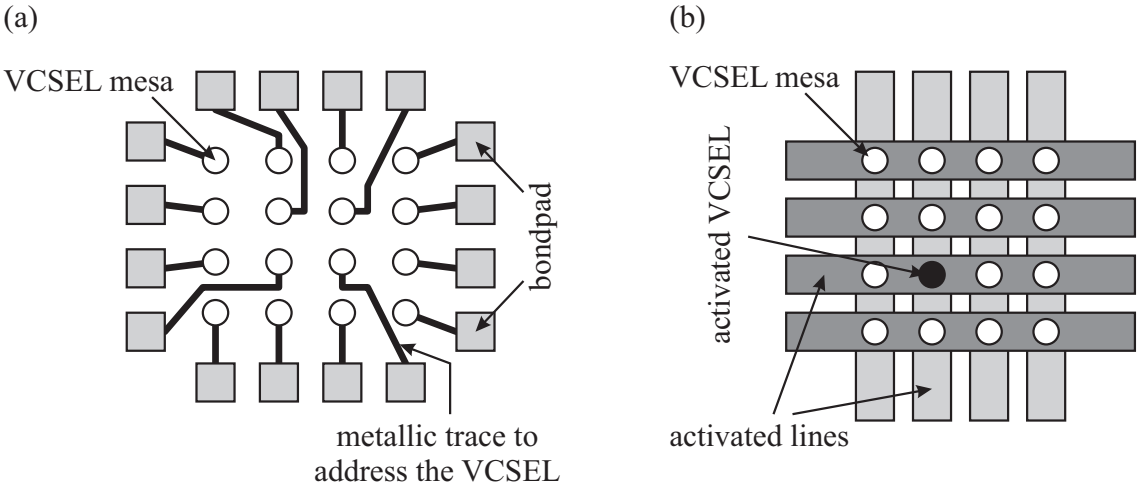

Fig. 1: Sketches of 4×4 VCSEL arrays with (a) independent addressing and (b) matrix addressing schemes.

2. Layer Structure

In order to fabricate matrix-addressable VCSEL arrays, there are some differences in the layer structure compared with common n-contact arrays. For instance, in matrix-addressable arrays the epitaxial structure is grown on an undoped GaAs substrate to allow electrical isolation of columns, in contrast to the common n-contact scheme, which requires an n-doped GaAs substrate. Above the undoped GaAs substrate, there is a 2.5 µm thick heavily n-doped GaAs layer to allow n-metallization. The n- and p-type distributed Bragg reflectors (DBRs) consist of 38.5 Si-doped $Al_{0.2}Ga_{0.8}As/Al_{0.9}Ga_{0.1}As$ DBR pairs and 23 C-doped $Al_{0.2}Ga_{0.8}As/Al_{0.9}Ga_{0.1}As$ pairs, respectively. The DBRs are graded in composition and doping concentration for minimizing the free-carrier absorption and decreasing the electrical resistance. The active region composed of three 7.9 nm thick GaAs quantum wells (QWs) separated by 9.9 nm thick $Al_{0.27}Ga_{0.73}As$ barriers is positioned in an optical cavity with a thickness of one material wavelength. The laser emission wavelength using these materials together with the cavity design is in the vicinity of 850 nm. A 32 nm thick AlAs oxidation layer is placed above the QWs. The function of this layer is twofold: When a part of it is oxidized to form the active aperture, not only the excitation current is confined but also optical guiding of the laser radiation occurs.

3. Fabrication Processes

Firstly, the VCSEL mesas have been defined by photolithography followed by reactive ion etching (RIE). In order to obtain a high packing density it is not possible to use wet-chemical etching, because the mesa side walls will not be vertical but instead have a slope. In addition, wet etching causes an undercut of the AlAs layer for long etching times, as indicated in the scanning electron micrograph in Fig. 2 (left). This is due to the higher etching rate of this layer compared with that of GaAs/AlGaAs. Such an undercut causes stress in the layer structure and makes planarization difficult. For these reasons, RIE has

been utilized. Figure 2 (right) shows a scanning electron micrograph of the RIE- etched mesa. A radio frequency power of 35 W has been used and the gas pressure was 9 mTorr. $SiCl_4$ and Ar with gas flow rates of 10 sccm and 6 sccm, respectively have been employed. Etching was done down to the depth of the n-buffer layer. Amongst the most challenging processes in two-dimensional VCSEL arrays is the separation of columns. The distance between these columns can be as small as 5 µm and the photolithography resolution is not sufficient for the topology resulting from the first etching process. For this reason two different pitches have been chosen to guarantee the success of processing. The fabrication was successful when the separation between columns was 12 µm instead of 5 µm. After column isolation had been carried out, n-metallization was applied on the buffer layer. In order to planarize the etched regions, four polyimide planarization steps were made to allow evaporation of p-metallization through the rows. After this, an 800 nm thick Ni/Au metallic layer was evaporated to serve as bondpads for wire bonding in an integrated chip package. To allow higher packing density, alternating bondpads have been utilized on all sides of the chip. Figure 3 shows a scanning laser microscope top view of a fabricated VCSEL array after wire bonding. A photo of the packaged chip is displayed in Fig. 4

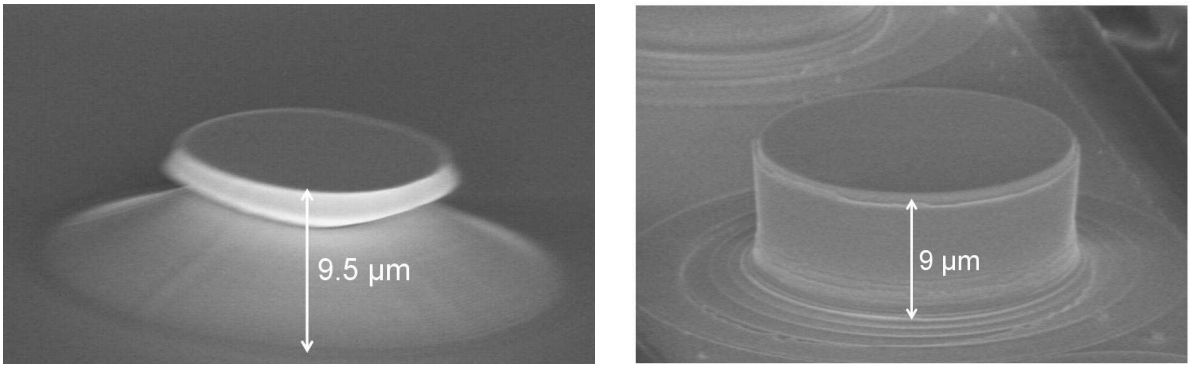

Fig. 2: Scanning electron micrographs of an etched mesa using wet-chemical etching (left) and reactive ion etching (right).

4. Laser Characteristics of Matrix-Addressable VCSEL Arrays

The light–current–voltage (LIV) characteristics of some devices in a fully processed 16×16 elements VCSEL array are displayed in Fig. 5. The distance between centers of two neighboring VCSELs is 84 µm. The active diameter of the aperture is 10 µm. The threshold current varies from 0.5 mA to 1.6 mA and the maximum output power at thermal rollover is between 2.4 and 4 mW. Such variation is due to a gradient in layer thicknesses during crystal growth by molecular beam epitaxy which causes variations in the reflectivities of n- and p-type DBRs and the gain throughout the wafer. The difference in voltage drop from one VCSEL to another is due to a change in the parasitic resistance, namely the longer is the distance from the bondpad to the VCSEL, the higher is the corresponding resistance. A simple analysis of this resistance has been done, based on measuring the resistances of the p-row, n-column and the mesa separately. These individual components

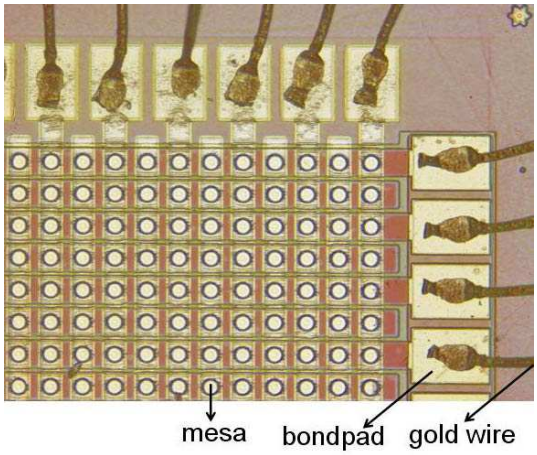

Fig. 3: Scanning laser micrograph of part of a 16 × 16 elements matrix-addressable VCSEL array.

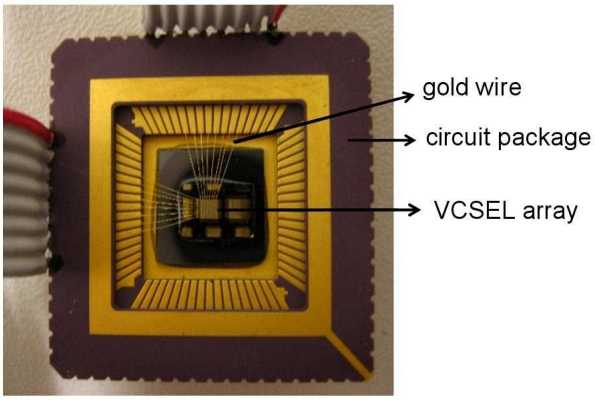

Fig. 4: Photograph of the processed VCSEL array.

were summed up (since the resistors are connected in series) and compared to the resistances extracted from the current–voltage curves. From the measurements, the average p-row resistance is 22 Ω and the n-column resistance is 27.5 Ω. In this analysis, the mesa resistance is assumed to be the resistance of the VCSEL when the nearest electrodes are activated. This resistance varies throughout the wafer due to different etch depths caused by the gradient in layer thickness. Table 1 summarizes the resistances for different mesas.

5. Conclusion

In this article, fabrication and characterization of densely packed (84 µm pitch) top-emitting 16 × 16 elements matrix-addressable VCSEL arrays have been reported. A simple analysis of the parasitic line resistances has been made.

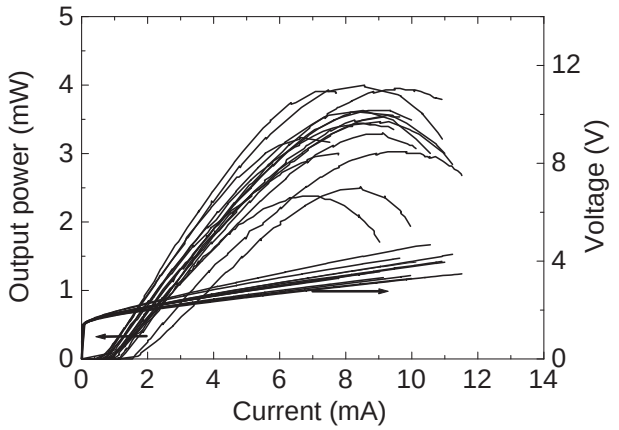

Fig. 5: Light–current–voltage characteristics of some devices within a processed matrix-addressable VCSEL array.

Table 1: Resistances extracted from the IV curves and accumulated measured resistances at different positions within the VCSEL array, where the mesa resistance varies.

Resistance from IV curve (Ω)	Accumulated resistance (Ω)	Mesa resistance (Ω)
174	178	128
153	154	104
144	146	97
138	142	93

References

[1] R.A. Morgan, G.D. Guth, C. Zimmer, R.E. Leibenguth, M.W. Focht, J.M. Freund, K.G. Glogovsky, T. Mullally, F.F. Judd, and M.T. Asom, "Two-dimensional matrix addressed vertical cavity top-surface emitting laser array display", *IEEE Photon. Technol. Lett.*, vol. 6, no. 8, pp. 913–917, 1994.

[2] A. Von Lehmen, C. Chang-Hasnain, J. Wullert, L. Carrion, N. Stoffel, L. Florez, and J. Harbison, "Independently addressable InGaAs/GaAs vertical-cavity surface-emitting laser arrays", *Electron. Lett.*, vol. 27, no. 7, pp. 583–585, 1991.

[3] E.G. Paek, J.R. Wullert, M. Jain, A. Von Lehmen, A. Scherer, J. Harbison, L.T. Florez, H.J. Yoo, R. Martin, J.L. Jewell, and Y.H. Lee, "Compact and ultrafast holographic memory using a surface-emitting microlaser diode array", *Opt. Lett.*, vol. 15, no. 6, pp. 341–343, 1990.

[4] M. Orenstein, A.C. Von Lehmen, C. Chang-Hasnain, N.G. Stoffel, J.P. Harbison, and L.T. Florez, "Matrix addressable vertical cavity surface emitting laser array", *Electron. Lett.*, vol. 27, no. 5, pp. 437–438, 1991.

[5] K.M. Geib, K.D. Choquette, D.K. Serkland, A.A Allerman, and T.W. Hargett, "Fabrication and performance of two-dimensional matrix addressable arrays of integrated vertical-cavity lasers and resonant cavity photodetectors", *IEEE J. Select. Topics Quantum Electron.*, vol. 8, no. 4, pp. 943–947, 2002.

[6] A.J. Danner, J.C. Lee, J.J. Raftery, N. Yokouchi, and K.D. Choquette, "Coupled-defect photonic crystal vertical cavity surface emitting lasers", *Electron. Lett.*, vol. 39, no. 18, pp. 1323–1324, 2003.

[7] L. Bao, N.-H. Kim, L.J. Mawst, N.N. Elkin, V.N. Troshchieva, D.V. Vysotsky, and A.P. Napartovich, "Near-diffraction-limited coherent emission from large aperture antiguided vertical-cavity surface-emitting laser arrays", *Appl. Phys. Lett.*, vol. 84, no. 3, pp. 320–322, 2004.

[8] A.C. Lehman, J.J. Raftery, Jr., A.J. Danner, P.O. Leisher, and K.D. Choquette, "Relative phase tuning of coupled defects in photonic crystal vertical-cavity surface-emitting lasers", *Appl. Phys. Lett.*, vol. 88, no. 2, pp. 021102-1–2, 2006.

[9] J.J. Raftery, Jr., A.J. Danner, J.C. Lee, and K.D. Choquette, "In-phase evanescent coupling of two-dimensional arrays of defect cavities in photonic crystal vertical cavity surface emitting lasers", *Appl. Phys. Lett.*, vol. 89, no. 8, pp. 081119-1–3, 2006.

[10] A.C. Lehman, J.J. Raftery, Jr., P.S. Carney, and K.D. Choquette, "Coherence of photonic crystal vertical-cavity surface-emitting laser arrays", *IEEE J. Quantum Electron.*, vol. 43, no. 1, pp. 25–30, 2007.

Polarization Division Multiplexed Data Transmisison Using Surface Grating VCSELs

Johannes Michael Ostermann and Pierluigi Debernardi[†]

We demonstrate free-space transmission of an aggregate data rate of 16 Gbit/s using polarization division multiplexing with two multimode VCSELs, their polarization being stabilized by monolithic surface gratings.

1. Introduction

Polarization stability of vertical-cavity surface-emitting lasers (VCSELs) is of crucial importance in particular for single-mode devices used in optical communications and optical sensing such as in computer mice.

In recent years, we have shown that an unprecedented level of polarization stability can be reached with surface gratings, which provide a monolithically integrated type of polarization-dependent feedback. Single-mode as well as multimode grating VCSELs have been fabricated in large quantity and have been shown to be polarization-stable with high orthogonal polarization suppression ratio not only for static operation but also under digital and analog modulation, temperature variation, optical feedback, as well as externally applied stress [1]. As a design example, Fig. 1 displays the light outcoupling facet of a manufactured grating VCSEL.

In this article we discuss an application of grating VCSELs in optical communications which we targeted some years ago [2], namely free-space data transmission employing polarization division multiplexing.

2. Free-Space Optics for Interconnection

Full polarization control of surface grating VCSELs is also maintained under high-frequency modulation [3], [4]. Such devices thus also lend themselves to applications in optical communications. Multimode VCSELs with emission in the 850 nm wavelength range are widely used for multimode fiber-based data transmission, where, however, no requirements are put on the polarization behavior. Single-mode fiber transmission demands transverse single-mode VCSEL emission, where polarization switches are very detrimental to the dynamics and noise characteristics. Thus, polarization stability is an important issue in long-wavelength 1.31 and 1.55 μm VCSELs. On the other hand, short-wavelength

[†]Pierluigi Debernardi is with the IEIIT-CNR c/o Politecnico di Torino, Torino, Italy

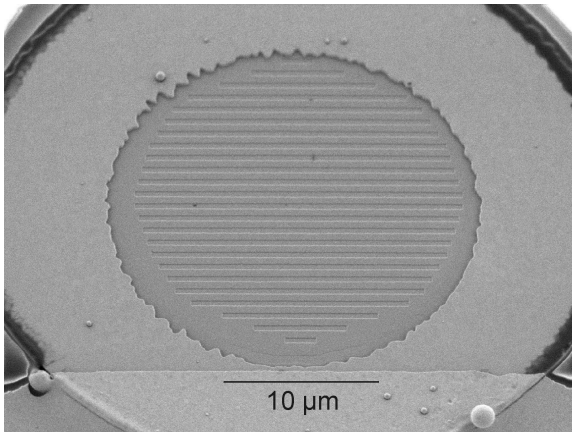

Fig. 1: Scanning electron micrograph of a fully processed VCSEL incorporating a surface grating (from [2]).

850 nm devices are widely used in free-space optics (FSO) equipment [5] for optical interconnection over distances of about 100 m to a few kilometers. In these cases, multimode VCSELs are preferred due to higher output power and thus a more favorable link power budget [6], [7].

Dynamically polarization-stable multimode VCSELs enable polarization division multiplexed data transmission. In this approach, two VCSELs with orthogonal polarizations serve as independently modulated sources of an optical link. The data are sent over a common, ideally polarization-maintaining medium, which is simply air in the case of free-space communication. A particularly compact setup would comprise two orthogonally polarized VCSELs that are monolithically integrated on a single chip and whose emissions are collimated by individual microlenses. At the receiver side, the light is focused on two photodetectors, in front of which two polarizers select the corresponding polarization channel. Applying this technique, the data throughput over a given link can be doubled.

3. Experimental Setup

The functionality of a free-space optics system is demonstrated with the setup shown in Fig. 2. Two grating VCSELs with orthogonal polarization are modulated with the data signal and the inverted data signal of a pattern generator, where the inverted signal is delayed by $(m + 1/2)$ bit periods with m being an integer. The emitted light of the two VCSELs is combined with a polarization-independent beamsplitter, transmitted through a polarizer, and then coupled to a fiber-pigtailed photodetector. The eye diagrams are measured with a sampling oscilloscope. The 860 nm VCSELs used in this experiment have an active diameter of 7 µm, a grating period of 0.75 µm, and a grating depth of 76 nm.

4. 8 Gbit/s Data Transmission

Figure 3 (top left) shows the optical eye diagram of one of these grating VCSELs without the polarizer in the optical link and with the second laser switched off. The data rate of

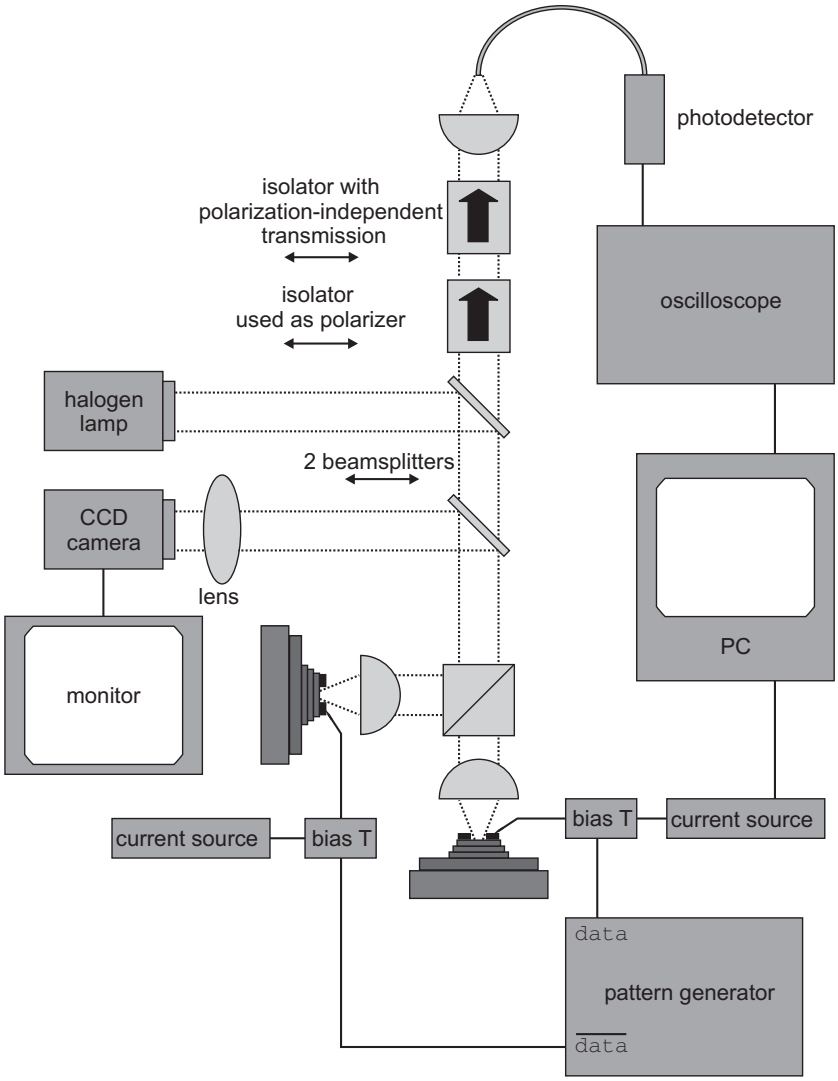

Fig. 2: Measurement setup used to demonstrate polarization division multiplexing. Double arrows indicate components that can be removed from the optical path.

the pseudorandom bit sequence is 8 Gbit/s at a word length of $2^{31} - 1$, the modulation amplitude is $0.7\,V_{pp}$, and the bias current is 9 mA. The eye is wide open and its quality does not degrade when a polarizer (oriented for maximum transmission) is inserted into the optical path (Fig. 3, bottom left). Even when the second VCSEL with an orthogonal polarization is switched on and is modulated, the optical eye is not distorted (Fig. 3, bottom right), since the signal of the second VCSEL is attenuated by more than 50 dB at the polarizer in front of the detector. The fact that the second VCSEL does not interfere with the original data transmission can also be seen from the bit error rate measurements in Fig. 3 (top right).

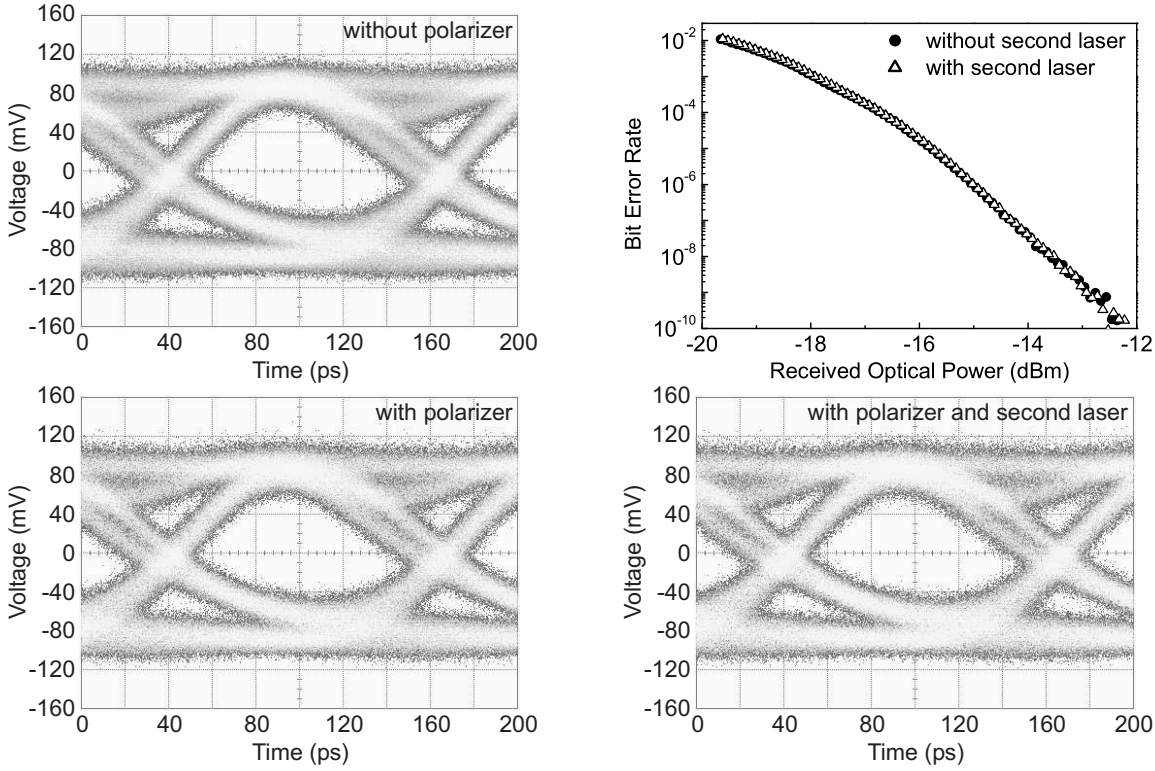

Fig. 3: Optical eye diagrams of surface grating VCSELs at a data rate of 8 Gbit/s. Channel 1 VCSEL before (top left) and after (bottom left) the insertion of the polarizer in Fig. 2 as well as with the orthogonally polarized channel 2 VCSEL switched on (bottom right). Bit error rate characteristics corresponding to the bottom left and right eye diagrams (top right).

5. Polarization Channel Selection

In the setup described above, just one detector and one polarizer are used. One of the two polarization channels is selected by rotating the polarizer, as can be seen in Fig. 4. The orientation of the polarizer is varied between 0° and 90° with respect to the [011] crystal axis. Comparing the eye diagrams for 0° and 90°, one can see the displacement of the two polarization channels by half a bit period, as mentioned above. The eye diagrams in both channels are clearly open. An aggregate data rate of 16 Gbit/s could be easily achieved by adding a second detector. Likewise, this experiment would also work with two adjacent (e.g., 250 µm distance) grating VCSELs on a single chip. It has been shown before that orthogonal grating orientations of such devices result in orthogonal light output polarization [8]. This approach was not chosen here because of the lack of appropriate optics that — in a practical system — has to shape the output into a joint free-space beam with a given divergence angle.

6. Conclusion

We have demonstrated the feasibility of using transverse multimode surface grating VCSELs for free-space data transmission over independent data channels with orthogonal

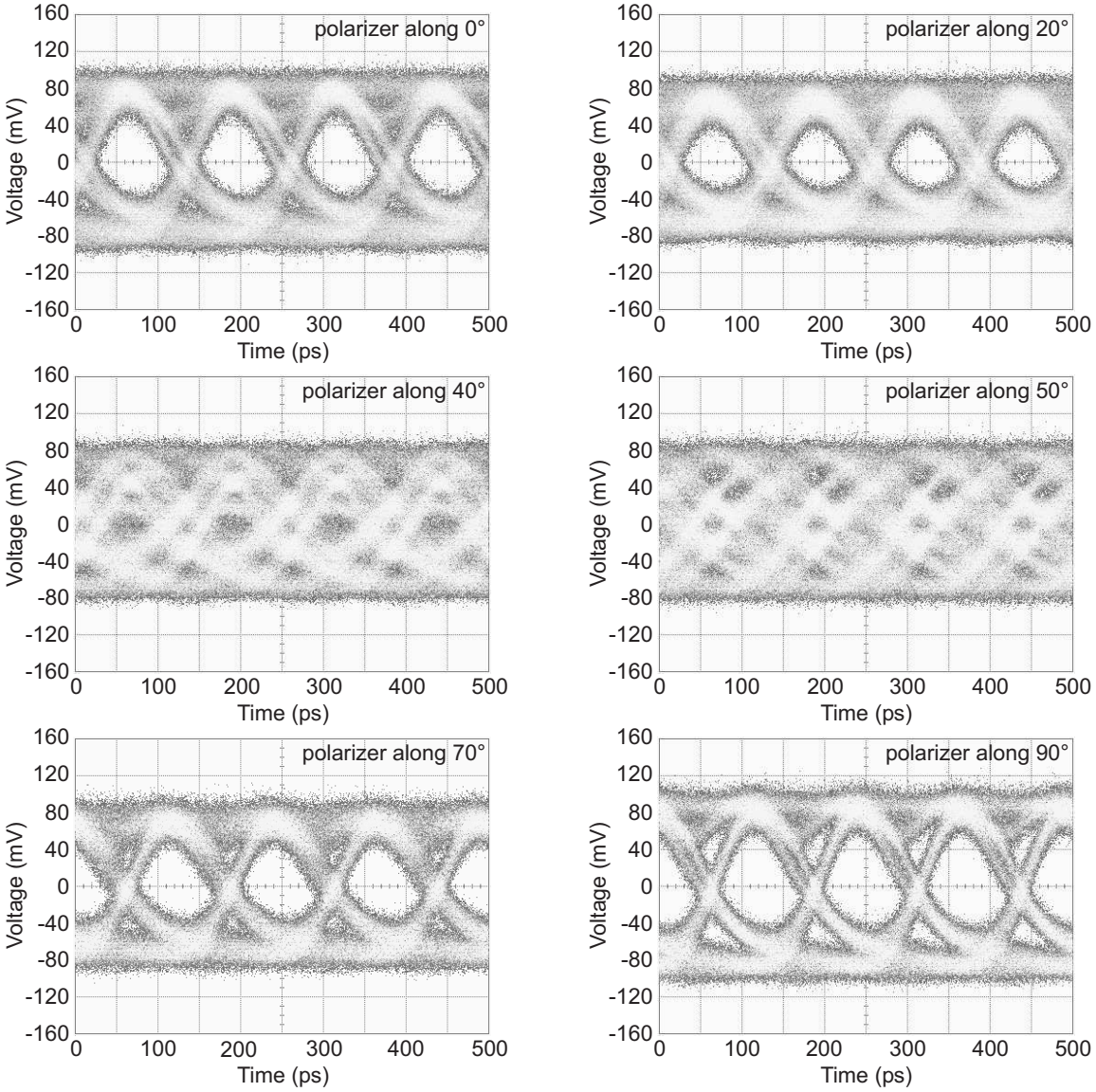

Fig. 4: Optical eye diagrams recorded for a free-space polarization division multiplexed optical link using two orthogonally polarized grating VCSELs that are simultaneously modulated at 8 Gbit/s data rate. The orientation of the polarizer is indicated in each graph. The VCSELs and the modulation conditions are the same as in Fig. 3.

polarization. The aggregate data rate of 16 Gbit/s was limited by the particular chip design of the VCSELs and not by the surface grating technique. For practical applications in existing VCSEL-based FSO transceivers, beam combination optics adapted to an integrated two-laser transmitter chip need to be developed. On the receiver side, two detection units behind a shared main collimation lens have to be used. The induced power penalties due to the finite orthogonal polarization suppression of low-cost polarizer foils or due to static or dynamic rotational misalignment between both transceiver units must also be investigated.

References

[1] R. Michalzik, J.M. Ostermann, and P. Debernardi, "Polarization-stable monolithic VCSELs" (invited), in *Vertical-Cavity Surface-Emitting Lasers XII*, C. Lei, J.K. Guenter (Eds.), Proc. SPIE 6908, pp. 69080A-1–16, 2008.

[2] R. Michalzik, J.M. Ostermann, P. Debernardi, C. Jalics, A. Kroner, M. Feneberg, and M. Riedl, "Polarization-controlled monolithic oxide-confined VCSELs", in *Micro-Optics, VCSELs and Photonic Interconnects*, H. Thienpont, K.D. Choquette, M.R. Taghizadeh (Eds.), Proc. SPIE 5453, pp. 182–196, 2004.

[3] J.M. Ostermann, P. Debernardi, and R. Michalzik, "Surface-grating VCSELs with dynamically stable light output polarization", *IEEE Photon. Technol. Lett.*, vol. 17, no. 12, pp. 2505–2507, 2005.

[4] C. Fuchs, T. Gensty, P. Debernardi, G.P. Bava, J.M. Ostermann, R. Michalzik, A. Haglund, A. Larsson, and W. Elsäßer, "Spatiotemporal turn-on dynamics of grating relief VCSELs", *IEEE J. Quantum Electron.*, vol. 43, no. 12, pp. 1227–1234, 2007.

[5] H. Willebrand and B.S. Ghuman, *Free-Space Optics: Enabling Optical Connectivity in Today's Networks*, Indianapolis, IN, USA: Sams Publishing, 2001.

[6] R. Michalzik, F. Mederer, H. Roscher, M. Stach, H. Unold, D. Wiedenmann, R. King, M. Grabherr, and E. Kube, "Design and communication applications of short-wavelength VCSELs", in *Materials and Devices for Optical and Wireless Communications*, C.J. Chang-Hasnain, Y. Xia, and K. Iga (Eds.), Proc. SPIE 4905, pp. 310–321, 2002.

[7] R. Michalzik, H. Roscher, M. Stach, D. Wiedenmann, M. Miller, J. Broeng, A. Petersson, N.A. Mortensen, H.R. Simonsen, and E. Kube, "Recent progress in short-wavelength VCSEL-based optical interconnections", in *Semiconductor Optoelectronic Devices for Lightwave Communication*, J. Piprek (Ed.), Proc. SPIE 5248, pp. 117–126, 2003.

[8] J.M. Ostermann, P. Debernardi, C. Jalics, and R. Michalzik, "Shallow surface gratings for high-power VCSELs with one preferred polarization for all modes", *IEEE Photon. Technol. Lett.*, vol. 17, no. 8, pp. 1593–1595, 2005.

Integrated Optoelectronic Chips for Bidirectional Optical Interconnection at Gbit/s Data Rates

Martin Stach and Alexander Kern

We report on the fabrication and properties of 850 nm wavelength AlGaAs–GaAs-based transceiver chips, in which vertical-cavity surface-emitting lasers (VCSELs) and metal–semiconductor–metal (MSM) photodiodes are monolithically integrated. Various types of devices allow half- and full-duplex bidirectional optical interconnection at up to 2.5 Gbit/s data rate using butt-coupled glass or polymer-clad optical fibers with diameters in the 100 to 200 µm range.

1. Introduction

Bidirectional transmission is a largely neglected technique in optical interconnection despite obvious advantages like lower volume and weight and potentially lower system cost. We have conceived and fabricated monolithic transceiver (Tx/Rx) chips that specifically target optical links with Gbit/s data rates. The chips are designed for 850 nm wavelength operation and consist of a vertical-cavity surface-emitting laser diode (VCSEL) and a metal–semiconductor–metal photodiode (MSM PD). For lowest assembly and packaging cost, they should be butt-coupled to the transmission fiber without any external optics. First generation devices had a light-sensitive diameter of slightly more than 200 µm, thus fitting to step-index polymer-clad silica (PCS) fibers which are attractive for automotive network incorporation. Data rates of 1 Gbit/s could be transmitted over a distance of 5 m with very large eye opening [1]. The versatility of the PCS fiber is much enhanced with a so-called semi-graded-index profile. Over the 200 µm diameter doped glass core, the refractive index is graded but has an additional step between the core and the surrounding polymer cladding. The fiber is a product of OFS (URL http://www.ofsoptics.com/), has a numerical aperture of 0.38 and an attenuation coefficient of less than 6 dB/km at 850 nm wavelength. Its bandwidth–distance product is larger than 40 GHz × m and is thus more than an order of magnitude higher than that of the step-index PCS fiber. In [2], bidirectional optical data transmission over such a 50 m-long fiber is reported at 1 Gbit/s data rate. The semi-GI PCS fiber has thus the potential to serve as a future-proof waveguiding medium in automotive optical networks, where multiple Gbit/s data streams are expected to be generated by, e.g., high-resolution real-time video equipment used for extensive road surveillance.

A further increase of data throughput is obtained with smaller core diameter graded-index glass fibers. In [1] we have reported half-duplex bidirectional interconnect experiments

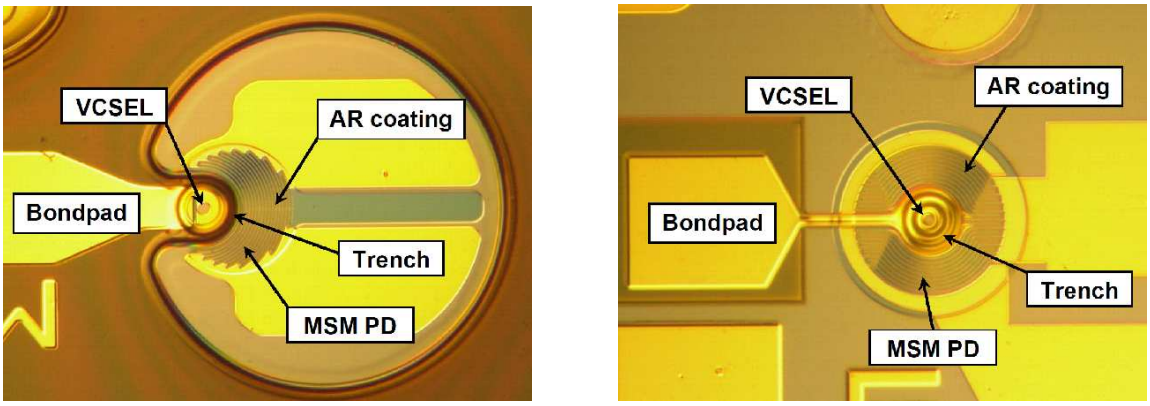

Fig. 1: Previous transceiver chip design (left) and modified version containing a centered VCSEL (right), both with 110 µm MSM photodiode diameter (from [5]).

with 110 µm diameter transceiver chips. Clearly open 1 Gbit/s eye diagrams are obtained for transmission over a 100 µm core diameter graded-index silica fiber with 100 m length. As with the PCS fiber, butt-coupling is applied at both ends of the link. The data throughput is in accordance with the fiber's bandwidth–distance product of about 100 GHz × m. The much increased fiber bandwidth allows extended reach applications, e.g., in home, industrial, or in-building networks as well as within computer clusters or central offices.

A photograph of the optoelectronic chips that were used so far is shown in Fig. 1 (left). It is seen that the laser is offset with respect to the PD center. The VCSEL position is a compromise between high fiber coupling efficiency and high quantum efficiency. For full illumination of the fiber cross-section, the area occupied by the VCSEL effectively reduces the responsivity of the PD. In a new design [3], the size of the VCSEL mesa is much reduced, such that the laser can be centered with respect to the photodiode without excessive consumption of light-sensitive area. Such a device is depicted in Fig. 1 (right). Higher coupling tolerances to the optical fiber are the main advantage of this approach. With an offset VCSEL, the coupling tolerances are asymmetric for displacements along the direction defined by the centers of laser and photodiode. This issue is investigated in detail in [4] and [1] for the 200 µm step-index PCS fiber and the 100 µm graded-index multimode fiber, respectively.

Optimized MSM photodiodes with highest bandwidths are grown on semi-insulating substrates in order to avoid capacitive coupling between the electrodes and doped semiconductor regions. Because of the presence of the electrically driven VCSEL, this approach cannot be easily followed in the integrated transceiver chips. As a consequence, the bandwidths of the photodiodes do not exceed 1.5 GHz even for small diameters of 110 µm. Since the intrinsic photodiode layers are rather thin, there is a large capacitive coupling between the PD metallization and the highly conductive VCSEL layers. Increasing the thickness of the absorption layer reduces the bandwidth due to longer transit times of photo-generated carriers. In this article, we present a new approach which increases the bandwidths of the MSM PDs by about 80 % through the incorporation of a 1 µm-thick undoped $Al_{0.3}Ga_{0.7}As$ layer between both devices (Fig. 2). The improvements are demonstrated by error-free full-duplex 2.5 Gbit/s bidirectional data transmission over a

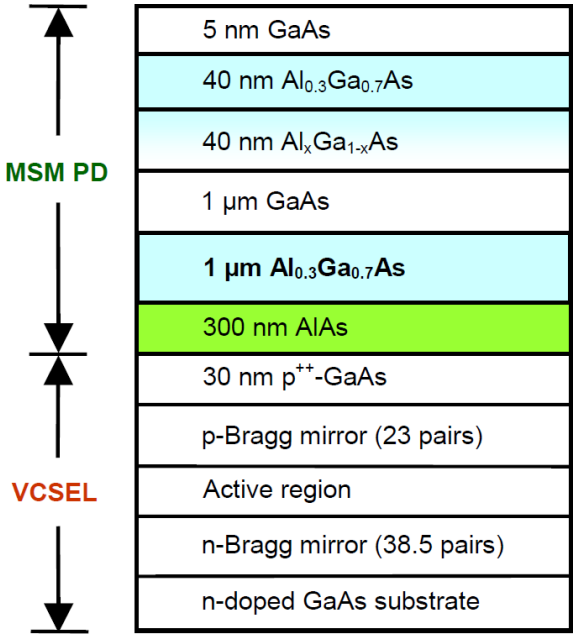

Fig. 2: Layer structure of monolithically integrated transceiver chips with enhanced bandwidth (from [5]).

50 m-long graded-index multimode fiber (MMF) with 100 µm core diameter, fully utilizing its specified bandwidth–distance product.

2. Transceiver Chip Fabrication

The monolithic transceiver chips contain all layers necessary for signal generation and reception. The MSM PD has a 1 µm-thick GaAs absorption layer and is grown on top of the VCSEL layers (Fig. 2). The lithographic process is similar to the one formerly described in [4], but an important difference arises due to the implementation of the additional 1 µm-thick $Al_{0.3}Ga_{0.7}As$ layer. To access the highly p-doped cap layer of the centered VCSEL (Fig. 1) homogeneously, a dry-etch process is applied followed by wet etching with a suitable citric acid solution. This step quickly and selectively removes residual $Al_{0.3}Ga_{0.7}As$ and stops reliably at the 300 nm-thick AlAs layer which is subsequently removed by hydrofluoric acid.

3. Static and Dynamic Characteristics

Figure 3 shows the photocurrents of MSM PDs with 110 µm diameter, 1 µm finger width, and 2 µm finger spacing as a function of the optical power for a number of bias voltages. The slope of the curves is constant for voltages exceeding 2 V. The corresponding responsivity amounts to 0.38 A/W and is independent of the light intensity. Both light reflection at the VCSEL layers and an antireflection (AR) coating contribute to the high responsivity.

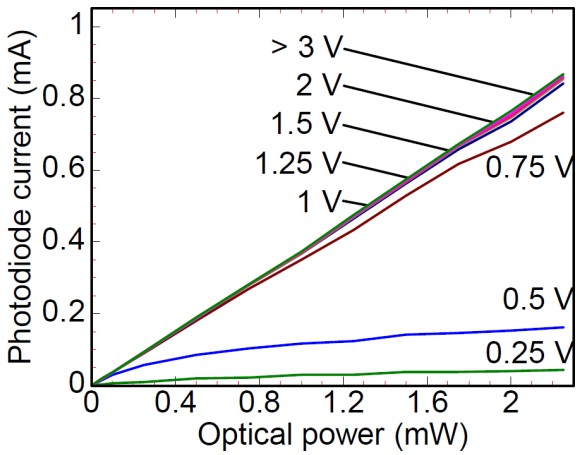

Fig. 3: Photocurrent of a transceiver MSM photodiode with 110 µm diameter as a function of incident optical power for various bias voltages (from [5]).

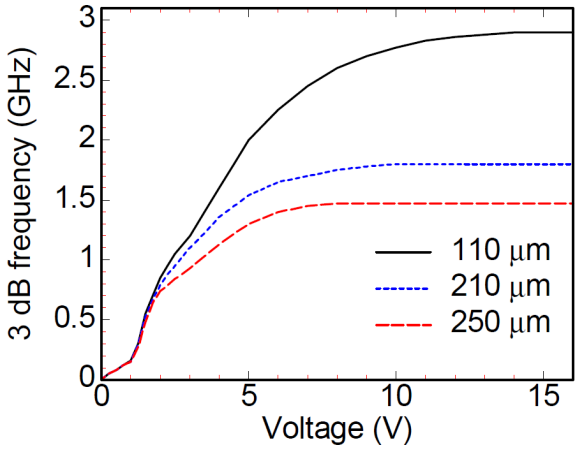

Fig. 4: Bandwidths of transceiver MSM PDs with different diameters on the new layer structure according to Fig. 2 (from [5]).

Typical bandwidths of transceiver MSM PDs with the improved layer structure and the same electrode configuration are depicted in Fig. 4. For photodiodes with 110 µm diameter of the light-sensitive area, the bandwidths saturate at 2.9 GHz. Larger diodes with 210 and 250 µm diameter have 3-dB bandwidths of 1.8 and 1.5 GHz, respectively. The increase of the corner frequency is about 80 % compared to Tx/Rx MSM PDs based on the previous layer structure.

The transceiver chips incorporate standard multimode 850 nm top-emitting oxide-confined VCSELs with 10 µm active diameter. Transverse multimode operation is preferred to single-mode emission due to more favorable modal noise properties in combination with a multimode fiber. As seen in Fig. 5, the lasers have minimum threshold currents of 1.4 mA at room temperature and still deliver optical output powers exceeding 3 mW at 100 °C. Typical small-signal 3 dB-frequencies are around 7 GHz (Fig. 6). Thus, the 110 µm diameter transceiver PDs still limit the maximum data rate despite of their enhanced bandwidths.

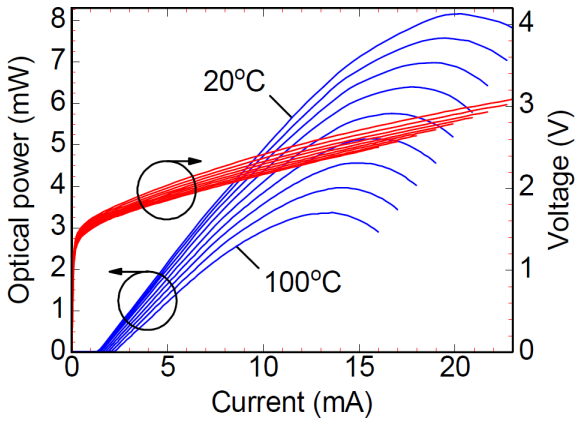

Fig. 5: Temperature-dependent operation characteristics of a transverse multimode transceiver VCSEL in steps of 10 °C (from [5]).

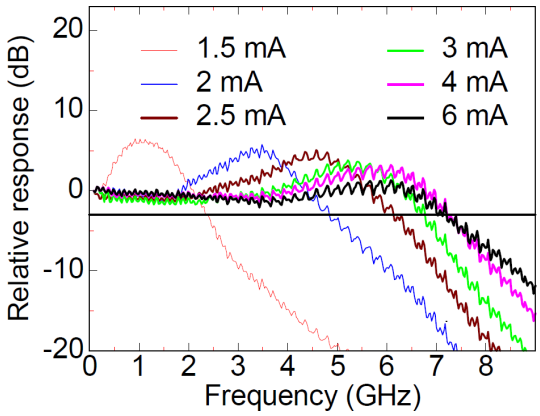

Fig. 6: Small-signal response curves of a transceiver VCSEL for various bias currents above threshold.

4. Digital Data Transmission

We first consider data transmission in the so-called back-to-back (BTB) mode, i.e., without the optical fiber. This is useful to determine the maximum system data rate without the influence of fiber dispersion. The transmission is established between a reference VCSEL and a circular PD (where no space is cut out for the VCSEL) on a transceiver-type layer structure according to Fig. 2 using two lenses for collimation and focusing. We employ a photodiode with 210 µm diameter, which has 1 µm finger width and 2 µm spacing. Its responsivity is 0.4 A/W and its 3-dB bandwidth amounts to 1.8 GHz. An amplifier with 10 GHz bandwidth and 50 Ω input impedance is used, and the signal is low-pass filtered, matched to the chosen data rate. Quasi error-free (10^{-11} bit error rate) 2.5 Gbit/s transmission of a non-return-to-zero coded pseudorandom bit sequence with 2^7–1 word length is achieved at –14.6 dBm received optical power (Fig. 7). The eye diagram is wide open even at 4 Gbit/s. For the transmission of still higher data rates using direct detection without signal processing, smaller photodiodes with lower capacitance and higher bandwidth must be used. This is illustrated with the good eye openings in

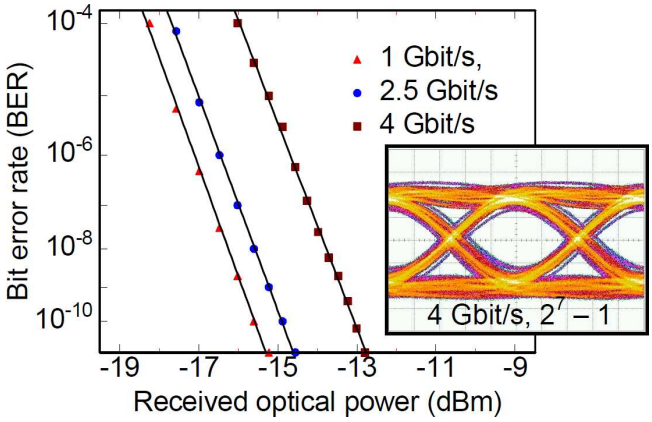

Fig. 7: Bit error rate curves for back-to-back (BTB) data transmission between VCSEL and transceiver photodiode with 210 µm diameter for various data rates as well as 4 Gbit/s eye diagram (from [5]).

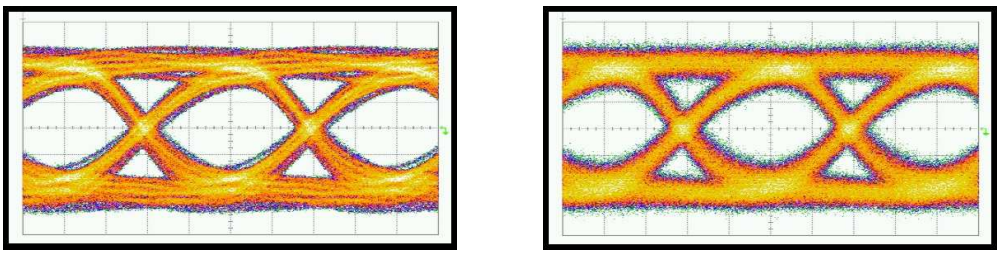

Fig. 8: 5 Gbit/s eye diagrams for BTB transmission between VCSEL and high-bandwidth PD with 110 µm diameter at word lengths of 2^7–1 (left) and 2^{31}–1 (right) (from [5]).

Fig. 8, where 5 Gbit/s data are received by 110 µm MSM PDs with otherwise identical finger structure. In this case, a low-pass filter with 5 GHz corner frequency was used.

For bidirectional data transmission, one butt-coupled transceiver chip is used at each fiber end at a distance of about 50 µm. In addition to the bidirectional nature of the chip, the lack of additional optics would greatly simplify the design of packaged modules. Each Tx/Rx chip consists of a 110 µm MSM PD according to Fig. 4 and an oxide-confined VCSEL similar to the one in Fig. 6. Both chips are nominally identical, however, due to a thickness gradient over the epitaxial wafer, the actual emission wavelengths (and threshold currents) are 852 nm (1.5 mA) and 839 nm (2.0 mA). For data transmission experiments in half-duplex mode, only one VCSEL is modulated, while the other one is biased above threshold. Low-pass filters with 3-dB bandwidths of 2000 and 2400 MHz help to reduce effects of electric on-chip crosstalk. The eye diagrams for transmission of a non-return-to-zero pseudorandom bit sequence with 2^7–1 word length at 2.5 Gbit/s data rate over 50 m MMF with 100 µm core diameter and 100 GHz × m bandwidth–distance product are wide open, indicating error-free transmission (Fig. 9 top left and right). The data transmission remains error-free also in full-duplex mode at the same bit rate using a second (3.0 vs. 12.5 Gbit/s maximum data rate) pattern generator (Fig. 9 bottom). Bias (and modulation) conditions are 9 mA (250 mV_{pp}) and 6 mA (500 mV_{pp}), where the minimum available peak-to-peak voltages have been used. Despite of the low-pass filters

and antireflection-coated Tx/Rx PDs, the eye openings are still slightly reduced, caused by both the remaining on-chip electrical crosstalk and the optical crosstalk chiefly arising from reflections at the far-end chip. The eye diagrams of channels 1 and 2 deviate somewhat, mainly due to different modulation and power levels. Error-free operation has also been achieved at 500 Mbit/s transmitted over a 300 m-long fiber. Data rates and fiber lengths are close to the limit imposed by the bandwidth–distance product of the fiber. Operation at the high data rate was only possible with the low-capacitance chips. Full-duplex transmission at 2.5 Gbit/s over several tens of meters is a very attractive option for many interconnect application areas.

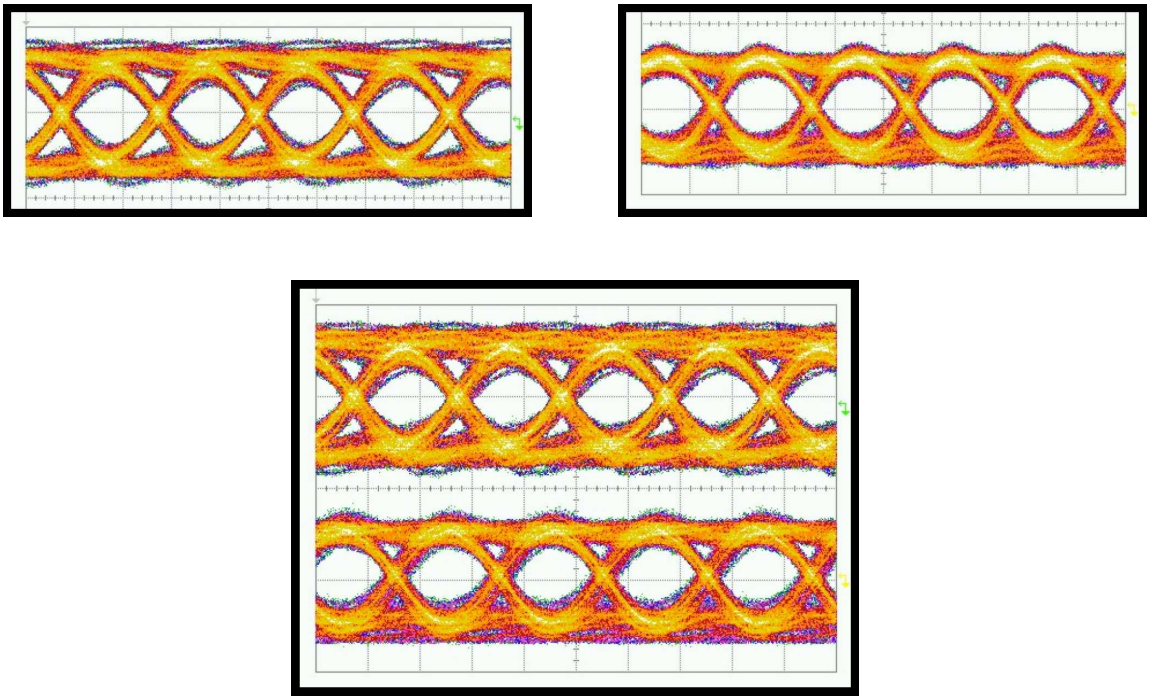

Fig. 9: Eye diagrams for bidirectional data transmission at 2.5 Gbit/s data rate over 50 m of 100 µm core diameter MMF in half-duplex mode for channel 1 (top left) and for channel 2 (top right) and full-duplex mode for channel 1 (bottom up) and channel 2 (bottom down).

5. Conclusion

A new generation of VCSEL–MSM transceiver chips was shown to be well suited for 100 µm core MMF data transmission at 2.5 Gbit/s owing to optimized PDs with bandwidths approximating those of solitary devices. Chips with smaller PDs adapted to standard MMFs are expected to offer even larger bandwidth–distance products of bidirectional optical data links.

References

[1] R. Michalzik, M. Stach, F. Rinaldi, and S. Lorch, "Monolithic integration of VCSELs and MSM photodiodes for bidirectional multimode fiber communications" (invited), in *Vertical-Cavity Surface-Emitting Lasers XI*, K.D. Choquette, J.K. Guenter (Eds.), Proc. SPIE 6484, pp. 648409-1–10, 2007.

[2] M. Stach, F. Rinaldi, J. Scharpf, S. Lorch, and R. Michalzik, "1 Gbit/s bidirectional optical data transmission over 50 m semi-GI PCS fiber with monolithically integrated transceiver chips", in Proc. *EOS Conf. on Trends in Optoelectronics, Sub-conf. on Information and Communication*, pp. 61–62. Munich, Germany, June 2007.

[3] M. Stach, F. Rinaldi, D. Wahl, D. Rimpf, S. Lorch, and R. Michalzik, "1 Gbit/s full-duplex bidirectional optical data transmission over 500 m of 50 µm-core graded-index multimode fiber with novel monolithically integrated transceiver chips, in Proc. *33rd Europ. Conf. on Opt. Commun., ECOC 2007*, vol. 5, pp. 127–128. Berlin, Germany, Sept. 2007.

[4] M. Stach, F. Rinaldi, M. Chandran, S. Lorch, and R. Michalzik, "Bidirectional optical interconnection at Gb/s data rates with monolithically integrated VCSEL-MSM transceiver chips", *IEEE Photon. Technol. Lett.*, vol. 18, pp. 2386–2388, 2006.

[5] M. Stach, F. Rinaldi, D. Wahl, D. Rimpf, S. Lorch, and R. Michalzik, "Monolithically integrated miniaturized transceiver chips for bidirectional graded-index fiber systems" (in German: "Monolithisch integrierte miniaturisierte Transceiver-Chips für bidirektionale Gradientenindexfaser-Systeme"), *14th ITG Symposium on Communication Cable Networks*, Köln, Germany, Dec. 2007. In *ITG-Fachbericht Kommunikationskabelnetze*, vol. 204, pp. 115–119, 2007.

Miniaturized Particle Manipulation With an Integrated Optical Trap Module

Andrea Kroner and Anna Bergmann

The combination of microfluidics and optical manipulation offers new possibilities for particle handling in the field of biophotonics. VCSELs with small dimensions and low power consumption allow such a combination at potentially low cost. The circular laser output beam is shaped by an etched surface relief and an integrated photoresist microlens. Thus the output beam is weakly focused with a beam waist of some micrometers in the microfluidic channel. The microfluidic chips are based on polydimethylsiloxane (PDMS). With this configuration we were able to demonstrate particle deflection with a linear VCSEL array integrated with a microfluidic chip.

1. Introduction

Optical tweezers open up the possibility of handling single particles with sizes in the nanometer to micrometer range while avoiding any mechanical contact [1]. The working principle is based on the momentum conservation of photons incident on a transparent particle [2]. Reflection and refraction lead to a scattering force pushing the particle forward, and also to a gradient force pulling the particle to the maximum of intensity, that is to say toward the optical axis. With these two forces a two-dimensional optical trap is generated. By using for example a tightly focused laser beam, a three-dimensional trap can be achieved [3], also called optical tweezers.

Another important research topic in recent years is the utilization of lab-on-a-chip systems for the biological and chemical analysis of samples. With such a system smallest particles can be isolated and investigated, combining several analysis steps, e. g., mixing, heating, and detection. The microfluidic channels used in these systems have widths of some ten micrometers.

For the selective manipulation of particles in microfluidic channels, the combination of microfluidics and optical manipulation has gained increasing interest. The use of vertical-cavity surface-emitting lasers (VCSELs) provides several advantages [4]. They have small dimensions with typical active diameters of less than ten micrometers, are inexpensive, and their symmetric structure supports a circular high-quality output beam. Their surface emission allows the comparatively easy fabrication of arbitrary-shaped two-dimensional arrays of optical tweezers, rendering techniques unnecessary like beam steering or holography. The dimensions can be additionally decreased by directly integrating microlenses on the laser surfaces. Avoiding any external optics allows the connection of laser source and microfluidic chip, resulting in a small and light weight portable system.

2. Integration of Laser Array and Microfluidic Channel

The operation of an integrated optical trap demands a minimized distance between the laser surface and the microfluidic chip to prevent strong beam expansion. At the same time, electrical contacts to the p-metalization at the top side of the laser chip must be realized. These requirements can be met by flip-chip bonding the laser chip to the microfluidic chip. Figure 1 shows a schematic of the module. The VCSEL array is located directly under a thin glass slide which seals the microfluidic channel. Indium solder bumps connect the p-contact pad to a metalization layer on the glass, which extends to the edges of the microfluidic chip. With this fan-out, the p-side of the lasers can be easily contacted, while the n-side is accessible by the common back side metalization.

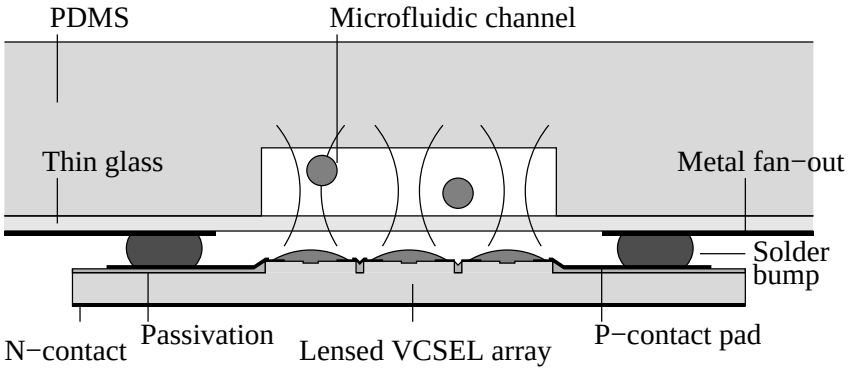

Fig. 1: Schematic of the integrated trap array module. The laser chip is directly connected to the microfluidic chip by indium solder bumps, which serve both as mechanical and electrical contact. The Gaussian-like output beams are shaped by integrated microlenses, thus generating weakly focused laser beams for particle manipulation at the sample stage [5].

Instead of using external optics, we have proposed the laser output beam to be shaped by a photoresist microlens, which is integrated directly on the laser output facet, as described above.

To fabricate this structure, lithography, metalization, and lift-off processes must be performed on the glass side of the microfluidic chip. After completion, the glass contains the metal fan-out as well as small islands of indium, by which a good alignment of the fan-out structure to the channel can be attained. For soldering, the laser chip is flipped and placed on the metalized glass side. When heated, the indium melts and alloys with the p-contact pad on the laser chip. After cool-down, a stable electrical and mechanical contact is formed.

Figure 2 shows a photograph of a complete module. It has a size of about $3.5 \times 3\,\mathrm{cm}^2$. The fan-out on the $30\,\mu\mathrm{m}$ thick glass and the VCSEL array chip soldered to its center are clearly visible. Directly below the laser chip with integrated microlenses, the PDMS layer contains a microfluidic T-junction, which ends in reservoirs for the generation of hydrostatic pressure.

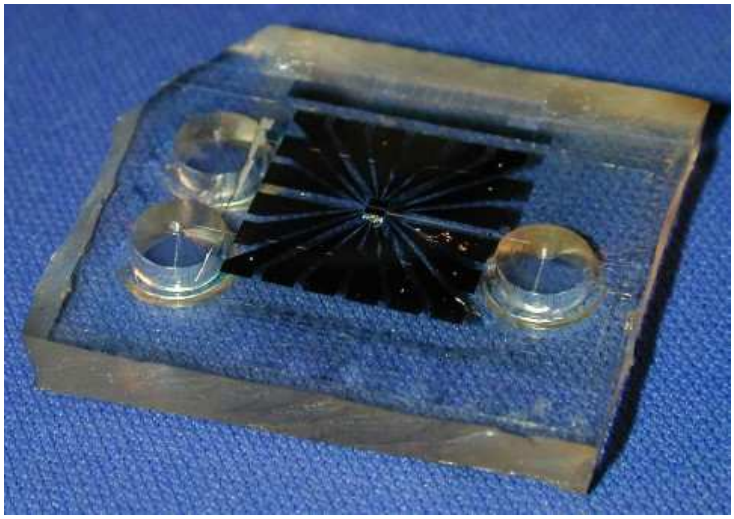

Fig. 2: Photograph of an integrated trap module (placed upside down) with a metal fan-out on the glass slide and a flip-chip-mounted VCSEL array chip in the center. The fluid reservoirs according to Fig. 7 can be seen in the PDMS layer.

3. Components of an Integrated Trap Module

3.1 Microlensed surface relief VCSELs

For the integrated optical trap module, a Gaussian-like beam profile is essential and can be attained with the inverted surface relief technique. In this process an additional $\lambda/4$-antiphase layer increases the threshold gain of the structure. By removing the layer selectively in the center of the laser output facet the transverse fundamental mode is being preferred.

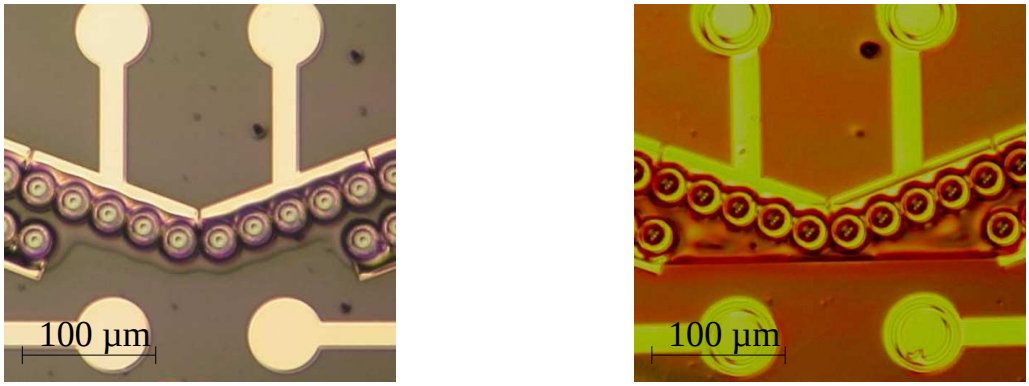

Fig. 3: Microscope images of laser arrays with five lasers connected in parallel. The laser facets are shown before (left) and after (right) the fabrication of microlenses.

The first step towards the miniaturization of the trap setup is the fabrication of integrated microlenses on the laser surfaces (Fig. 3). Figure 4 shows the fabrication of these lenses. In the first step, islands of PMGI photoresist are structured by optical lithography. In a

thermal reflow process the cylindrical islands assume spherical shapes. A variation of the radius of curvature can be achieved by changing the photoresist thickness.

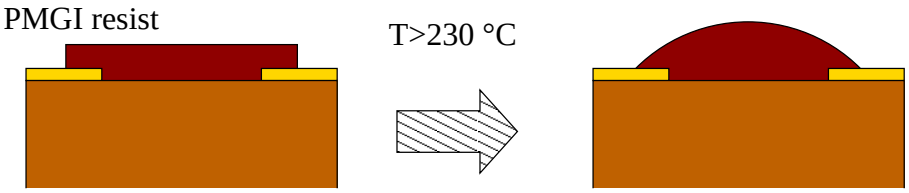

Fig. 4: Fabrication of a PMGI microlens on a laser surface. First a cylindrical island is lithographically structured (left). In a thermal reflow step this island assumes a spherical shape (right).

Figure 5 depicts the beam diameter with increasing distance from the laser surface. Whereas the standard VCSEL shows strong divergence, the device with surface relief and microlens features delayed divergence up to about 25 µm distance to the laser surface.

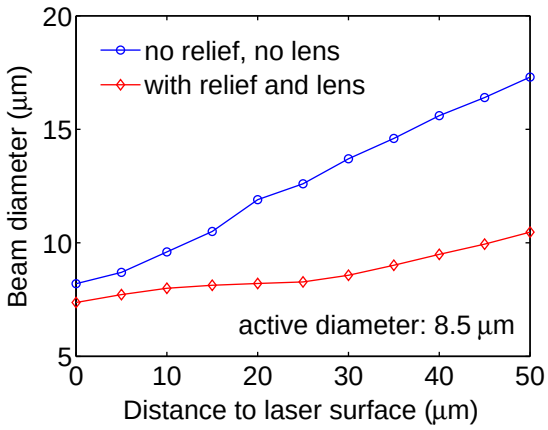

Fig. 5: Beam diameter versus the distance to the laser surface for both the standard and the relief VCSEL, the latter with an integrated microlens. The diameters of the oxide aperture and the relief are 8.5 and 4 µm, respectively.

The laser characteristics before and after the fabrication of the microlenses are compared in Fig. 6. The microlensed devices have lower threshold currents and increased maximum output powers. The polymer material of the lenses effectively reduces the phase detuning between relief and unetched region of the output facet, such that the laser characteristics tend to approach that of a standard VCSEL.

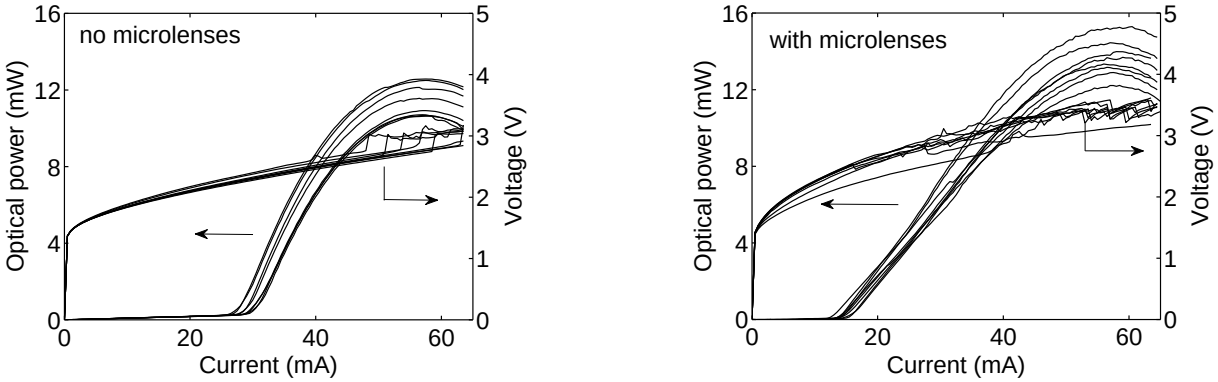

Fig. 6: Operation characteristics of eight VCSEL arrays according to Fig. 3 on a given sample, each array having five lasers driven in parallel. Measurements are done before (left) and after (right) the fabrication of microlenses. The VCSEL dimensions are as in Fig. 5.

3.2 Microfluidic chip

The microfluidic channels are made of polydimethylsiloxane (PDMS), a transparent and inert polymer. It is often used for prototyping due to straightforward fabrication based on a molding technique [6], as illustrated in Figure 7. At first, thick and stable SU8 resist is structured via lithography on a silicon wafer. It contains the negative image of the channel structure and serves as a master. The viscous PDMS is then poured over this mold and cured at 65 °C for one hour. Afterwards, the elastic PDMS can be peeled from the master wafer without damage. To close the channels, the PDMS is sealed with a cover glass. A prior treatment of both surfaces with oxygen plasma renders this connection irreversible. The fabricated microchannels contain T- and Y-junctions and have widths of 30 to 150 µm and a height of 50 µm. Inlet and outlets of the channels are connected to reservoirs containing polystyrene particles solved in water. The fluid levels can be adjusted, and the resulting difference in hydrostatic pressure leads to a controllable fluid flow inside the channels. The particle velocity can be varied from only a few µm/s to more than 100 µm/s.

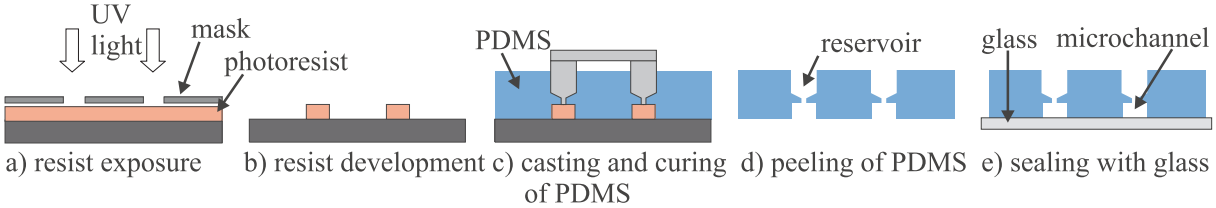

Fig. 7: Fabrication of microfluidic channels by a PDMS molding technique. With a custom-made metal tool, fluid reservoirs are incorporated during the casting step (c).

4. Deflection Experiments With the Integrated Trap

In this section we show continuous microparticle deflection and trapping with the integrated module from Fig. 2, in which the VCSEL array is tilted with respect to the flow direction of the microfluidic channel.

Figure 8 illustrates sequences of a deflection experiment with 15 µm diameter polystyrene particles at an optical power of about 5 mW. Besides the 100 µm wide microfluidic channel, also two linear VCSEL arrays are visible, where only the one at the upper half of the channel is operated. It is tilted by an angle of about 20°. The particles are moving from right to left with velocities of about 10 µm/s, depending on their position in the channel. In Fig. 8a, one 15 µm particle approaches the optical lattice and is attracted by the laser beams. The particle is deflected by the tilted optical lattice (Figs. 8b to h) and deviated from its initial path. While being laterally deflected, orthogonal to its flow direction, the particle is simultaneously lifted by the scattering force when moving from one trap to the next. This is indicated by a blurring of the particle image in the experiment. As seen in Fig. 8, the particle movement is rather slow and the deflection is not complete. These present shortcomings will be resolved in future with higher-power VCSEL sources.

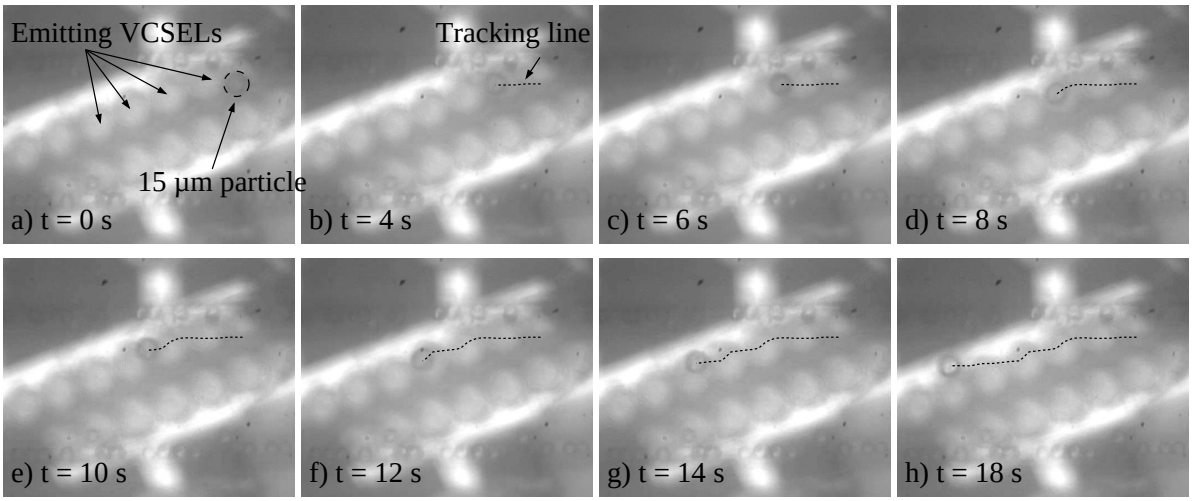

Fig. 8: Snapshots of a continuous deflection experiment with an optical power of 5 mW. A 15 µm polystyrene particle is redirected to the lower part of the channel while passing the optical lattice.

Particle trapping instead of deflection is achieved either with a reduced flow velocity or with an increased optical power. With the former method, the traps in Fig. 9 have been successively filled with 10 µm diameter polystyrene particles. Since the particles are lifted by the scattering force as described before, even multiple trapping can occur. Figure 9 shows four laser traps being occupied by up to three particles.

By increasing the size of the tilted VCSEL arrays, efficient optical particle separation in microfluidics should be achievable without external intervention. With similar schemes, where the optical lattice was generated with a single-beam source by interference or beam

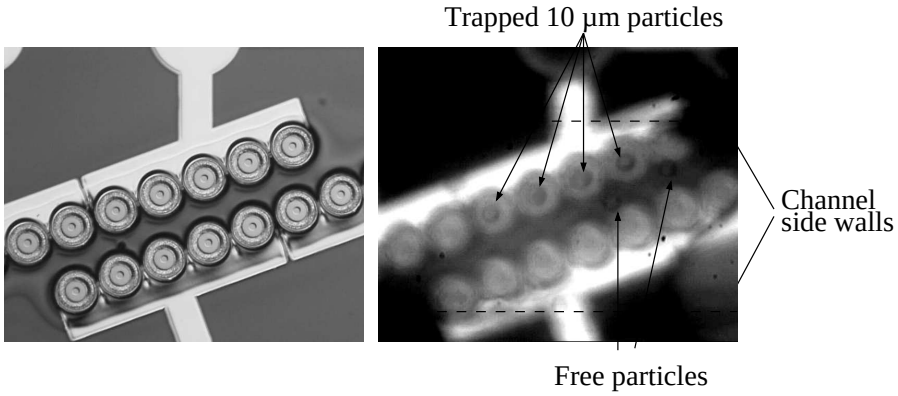

Fig. 9: Tilted VCSEL array with four laser traps occupied by up to three 10 µm particles. The optical output power in the trapping experiment was 5 mW. The photo on the left shows the surface relief VCSELs before the formation of microlenses.

splitting, also particle sorting was demonstrated by other groups. The sorting functionality relies on the fact that the interaction of particle and optical lattice is dependent on the material and geometrical properties of the particles [7]– [9]. In our approach, since the position of the optical lattice is fixed and no moving parts are necessary, the array can be connected to the chip, making this scheme attractive for direct integration.

5. Conclusion

We have shown our recent progress on VCSEL-based optical trapping combined with microfluidics. This work aims to demonstrate novel ultra-compact modules suited for microparticle analysis. It underlines the suitability of VCSELs as laser sources in optical manipulation systems. The small dimensions of VCSELs allow a drastic miniaturization by means of integrating the laser directly underneath the microfluidic channel. Microlenses are corporated on the laser output facets.

With a tilted linear VCSEL array in combination with a microfluidic chip, continuous particle deflection was demonstrated. In future work VCSEL output characteristics must be further improved by epitaxial design and heat sinking. Particle and finally biological cell sorting should then be possible in an efficient way.

References

[1] K. Dholakia, P. Reece, and M. Gu, "Optical manipulation," *Chem. Soc. Rev.*, vol. 37, pp. 42–55, 2008.

[2] A. Ashkin, "Acceleration and trapping of particles by radiation pressure," *Phys. Rev. Lett.*, vol. 24, pp. 156–159, 1970.

[3] A. Ashkin, J.M. Dziedzic, J.E. Bjorkholm, and S. Chu, "Observation of a single-beam gradient force optical trap for dielectric particles," *Opt. Lett.*, vol. 11, pp. 288–290, 1986.

[4] A. Kroner, J.F. May, I. Kardosh, F. Rinaldi, H. Roscher, and R. Michalzik, "Novel concepts of vertical-cavity laser-based optical traps for biomedical applications," in *Biophotonics and New Therapy Frontiers*, R. Grzymala and O. Haeberlé, eds., *Proc. SPIE*, vol. 6191, pp. 619112-1–12, 2006.

[5] A. Kroner, C. Schneck, F. Rinaldi, R. Rösch, and R. Michalzik, "Application of vertical-cavity laser-based optical tweezers for particle manipulation in microfluidic channels," in *Nanophotonics II*, D.L. Andrews, J.-M. Nunzi, A. Ostendorf, eds., *Proc. SPIE*, vol. 6988, pp. 69881R-1–12, 2008.

[6] J. Cooper McDonald and G.M. Whitesides, "Poly(dimethylsiloxane) as a material for fabricating microfluidic devices," *Acc. Chem. Res.*, vol. 35, pp. 491–499, 2002.

[7] M.P. MacDonald, G.C. Spalding, and K. Dholakia, "Microfluidic sorting in an optical lattice," *Nature*, vol. 426, pp. 421–424, 2003.

[8] K. Ladavac, K. Kasza, and D.G. Grier, "Sorting mesoscopic objects with periodic potential landscapes: optical fractionation," *Phys. Rev. E*, vol. 70, pp. 010901-1–4, 2004.

[9] Y.Y. Sun, L.S. Ong, and X.-C. Yuan, "Composite-microlens-array-enabled microfluidic sorting," *Appl. Phys. Lett.*, vol. 89, 141108-1–3, 2006.

Habilitation and Ph.D. Theses

1. Rainer Michalzik,
   Advanced Short-Wavelength Vertical-Cavity Surface-Emitting Lasers for Optical Interconnection.
   Habilitation Thesis, July 2008,
   Scientific presentation on *Effiziente LEDs (Efficient LEDs)*,
   February 2009.

2. Frank Demaria,
   Schicht- und Resonatordesign von Halbleiterscheibenlasern,
   Ph.D. Thesis, April 2008.

3. Fernando Rinaldi,
   MBE Growth and Characterization of Multilayer Structures for Vertically Emitting Laser Devices,
   Ph.D. Thesis, April 2008

4. Daniel Supper,
   Neuartige hybride 1300 nm VCSEL für die optische Übertragungstechnik,
   Ph.D. Thesis, June 2008.

5. Barbara Monika Neubert,
   GaInN/GaN LEDs auf semipolaren Seitenfacetten mittels selektiver Epitaxie hergestellter GaN-Streifen,
   Ph.D. Thesis, September 2008.

6. Peter Brückner,
   Herstellung freistehender Galliumnitrid-Schichten,
   Ph.D. Thesis, December 2008.

Diploma and Master Theses

1. Shamsul Arafin,
   Investigations Into Matrix-Addressable VCSEL Arrays,
   Master Thesis, March 2008.

2. Ahmed Al-Samaneh,
   Hybrid-Integrated Vertical Extended Cavity Surface-Emitting Lasers,
   Master Thesis, April 2008.

3. Dimitrios Marinos,
   Optical Communications in Aircraft Cabin Environment,
   Master Thesis, June 2008.

4. Mohamed Fikry,
   Epitaxy and Processing of AlGaInN Heterostructures for Light Emitting Diode Applications,
   Master Thesis, July 2008.

5. Frank Hesmer,
   Prozess- und Messplatzentwicklung zur Lebensdaueruntersuchung von Vertikallaserdioden auf einer Trägerplatte,
   Diploma Thesis, September 2008.

6. Dieter Rimpf,
   Hybrid-integrierte oberflächenemittierende Laser mit verlängertem Vertikalresonator,
   Diploma Thesis, September 2008.

7. Anna Bergmann,
   Miniaturisierte VCSEL-basierte Systeme zur optischen Partikelmanipulation in mikrofluidischen Kanälen,
   Diploma Thesis, September 2008.

8. Daniel Setz,
   Entwicklung und Herstellung von Vertikallaserdioden zur Nutzung in Atomuhren,
   Diploma Thesis, September 2008.

9. Kamran Forghani,
   Investigations on MOVPE Growth of AlGaN Heterostructures for UV LED Application,
   Master Thesis, November 2008.

10. Dong Zhang,
    Fabrication and Characterization of Densely Packed Matrix-Addressable VCSEL Arrays,
    Master Thesis, December 2008.

Semester Projects

1. Meike Slocinski,
   Particle Separation Module for Particles Between 0.5 and 2 μm,
   July 2008.

2. Martin Klein,
   Experimentelle Untersuchung der spektralen Eigenschaften und Polarisation von Halbleiterscheibenlasern,
   September 2008.

3. Meijie Li,
   Optically-Pumped Semiconductor Disk Lasers and Their Front Reflection Characteristics,
   September 2008.

Talks and Conference Contributions

[1] F. Demaria, S. Lorch, S. Menzel, M.C. Riedl, F. Rinaldi, R. Rösch, and P. Unger, "Design of highly-efficient high-power optically-pumped semiconductor disk lasers", *21st IEEE International Semiconductor Laser Conference, ISLC2008*, Sorrento, Italy, Sept. 2008.

[2] A. Gadallah, A. Kroner, I. Kardosh, F. Rinaldi, and R. Michalzik, "Oblong-shaped VCSELs with pre-defined mode patterns", *SPIE Photonics Europe*, Conf. on *Semiconductor Lasers and Laser Dynamics III*, Strasbourg, France, Apr. 2008.

[3] J. Hertkorn F. Lipski P. Brückner, S.B. Thapa, T. Wunderer, F. Scholz, A. Chuvilin, U. Kaiser, M. Beer, and J. Zweck, "Process optimization for the effective reduction of threading dislocations in MOVPE grown GaN using in situ deposited SiN_x", poster at *14th Int. Conf. on MOVPE* (ICMOVPE XIV), Metz, France, June 2008.

[4] A. Kroner, F. Rinaldi, R. Rösch, I. Kardosh, and R. Michalzik, "Towards a compact particle manipulation system based on arrays of vertical-cavity laser diodes", *Nonlinear Microscopy and Optical Control, NMOC 2008*, Münster, Germany, Feb. 2008.

[5] A. Kroner, C. Schneck, F. Rinaldi, R. Rösch, and R. Michalzik, "Application of vertical-cavity laser-based optical tweezers for particle manipulation in microfluidic channels", *SPIE Photonics Europe*, Conf. on *Nanophotonics*, Strasbourg, France, Apr. 2008.

[6] A. Kroner, F. Rinaldi, R. Rösch, I. Kardosh, and R. Michalzik, "Ultra-miniaturized optical particle manipulation using densely integrated laser arrays", *1st Int.'l Sympos. on Optical Tweezers in Life Sciences*, Berlin, Germany, May 2008.

[7] F. Lipski, S.B. Thapa, J. Hertkorn, T. Wunderer, S. Schwaiger, F. Scholz, M. Feneberg, K. Thonke, H. Hochmuth, M. Lorenz, and M. Grundmann, "Studies towards freestanding GaN in hydride vapor phase epitaxy by in-situ etching of a sacrificial ZnO buffer layer", poster at *5th International Workshop on Nitride Semiconductors* (IWN2008), Montreux, Switzerland, Oct. 2008.

[8] R. Michalzik, J.M. Ostermann, and P. Debernardi, "Polarization-stable monolithic VCSELs" (invited), *SPIE Photonics West 2008, Vertical-Cavity Surface-Emitting Lasers XII*, San Jose, CA, USA, Jan. 2008.

[9] F. Rinaldi, "HRXRD characterization of highly complex MBE grown multilayer structure for optoelectronics applications", *17th European Heterostructure Technology Workshop*, HETECH 2008, Venice, Italy, Nov. 2008.

[10] F. Scholz, S.B. Thapa, J. Hertkorn, T. Wunderer, F. Lipski, A. Reiser, Y. Xie, M. Feneberg, K. Thonke, R. Sauer, M. Dürrschnabel, L.D. Yao, and D. Gerthsen, "Epitaxial growth of ZnO-GaN Hetero-Nanorods and GaN Nanotubes", *3rd Nanowire Growth Workshop*, Duisburg, Germany, Sept. 2008.

[11] F. Scholz, "Epitaxial growth of high quality GaN and AlN by MOVPE", *Workshop "Quantum cascade lasers: Intersubband transitions–physics and technology"*, University of Göteborg, Sweden, Oct. 2008.

[12] F. Scholz, K. Forghani, F. Lipski, S. Schwaiger, S.B. Thapa, T. Wunderer, R.A.R. Leute, I. Tischer, M. Feneberg, K. Thonke, O. Klein, and U. Kaiser, "Untersuchungen zur MOVPE von AlGaN direkt auf Saphir", *DGKK-Workshop III-V-Epitaxie*, Braunschweig, Germany, Dec. 2008.

[13] F. Scholz, F. Lipski, P. Brückner, S. Schwaiger, J. Hertkorn, and T. Wunderer, "Hydrid-Gasphasenepitaxie von GaN: Der Weg zum GaN-Substrat?", *DGKK-Workshop III-V-Epitaxie*, Braunschweig, Germany, Dec. 2008.

[14] S. Schwaiger, F. Lipski, T. Wunderer, and F. Scholz, "Wachstum unpolarer a-orientierter GaN-Schichten mittels MOVPE", *DGKK-Workshop III-V-Epitaxie*, Braunschweig, Germany, Dec. 2008.

[15] S.B. Thapa, J. Hertkorn, F. Scholz, G.M. Prinz, M. Feneberg, M. Schirra, K. Thonke, R. Sauer, O. Klein, J. Biskupek, and U. Kaiser, "Growth and studies of Si doped AlN layer", *14th Int. Conf. on MOVPE* (ICMOVPE XIV), Metz, France, June 2008.

[16] S.B. Thapa, J. Hertkorn, T. Wunderer, F. Scholz, A. Reiser, G.M. Prinz, M. Schirra, K. Thonke, and R. Sauer, "MOVPE growth of GaN around ZnO nanopillars", poster at *14th Int. Conf. on MOVPE* (ICMOVPE XIV), Metz, France, June 2008.

[17] T. Wunderer, J. Hertkorn, F. Lipski, P. Brückner, F. Scholz, M. Feneberg, M. Schirra, K. Thonke, A. Chuvilin, and U. Kaiser, "Bluish-green semipolar GaInN/GaN light emitting diode on $\{1\bar{1}01\}$ GaN side facets", *SPIE Photonics West*, San Jose, USA, Jan. 2008.

[18] T. Wunderer, J. Hertkorn, F. Lipski, P. Brückner, M. Feneberg, M. Schirra, K. Thonke, I. Knoke, E. Meissner, A. Chuvilin, U. Kaiser, and F. Scholz, "Semipolar GaInN/GaN LEDs on $\{1\bar{1}01\}$ GaN side facets", *Philips Lumileds*, San Jose, CA, USA, Jan. 2008.

[19] T. Wunderer, J. Hertkorn, F. Lipski, P. Brückner, M. Feneberg, M. Schirra, K. Thonke, I. Knoke, E. Meissner, A. Chuvilin, U. Kaiser, and F. Scholz, "Semipolar GaInN/GaN LEDs on $\{1\bar{1}01\}$ GaN side facets", *USCB,* Santa Barbara, CA, USA, Feb. 2008.

[20] T. Wunderer, F. Lipski, J. Hertkorn, P. Brückner, F. Scholz, M. Feneberg, R. Sauer, and K. Thonke, "Semipolar $\{1\bar{1}01\}$ GaInN quantum wells for green light emitting diodes", *DPG-Tagung*, Berlin, Germany, Feb. 2008.

[21] T. Wunderer, F. Lipski, J. Hertkorn, S. Schwaiger, and F. Scholz, "Fabrication of 3D InGaN/GaN structures providing semipolar GaN planes for efficient green light emission", *5th International Workshop on Nitride Semiconductors* (IWN2008), Montreux, Switzerland, Oct. 2008.

[22] T. Wunderer, F. Lipski, S. Schwaiger, J. Hertkorn, F. Scholz, M. Wiedenmann, M. Feneberg, and K. Thonke, "Herstellung von 3D GaInN/GaN Strukturen mit semipolaren Oberflächen für effiziente grüne Licht-Emission", *DGKK-Workshop III-V-Epitaxie*, Braunschweig, Germany, Dec. 2008.

[23] T. Wunderer, M. Fikry, J. Hertkorn, S. Schwaiger, F. Lipski, and F. Scholz, "Einfluss der Mg-Dotierung nahe der aktiven Zone auf die Effizienz von GaN-basierten LEDs und Lasern", *DGKK-Workshop III-V-Epitaxie*, Braunschweig, Germany, Dec. 2008.

[24] P. Debernardi, A. Kroner, F. Rinaldi, and R. Michalzik, "Hot-cavity model for non-circular VCSELs", *21st IEEE Int.'l Semicond. Laser Conf.*, Sorrento, Italy, Sept. 2008.

[25] M. Feneberg, T. Wunderer, F. Lipski, P. Brückner, F. Scholz, R. Sauer, and K. Thonke, "Semipolar $\{10\bar{1}1\}$ GaInN quantum wells for green light emitting diodes", *DPG-Tagung*, Berlin, Germany, Feb. 2008.

[26] O. Klein, J. Biskupek, U. Kaiser, S.B. Thapa, and F. Scholz, "Quantitative dislocation analysis of 2H AlN:Si grown on {0001} sapphire", *14th European Microscopy Congress* (EMC 2008), Aachen, Germany, Sept. 2008.

[27] A.V. Lobanova, E.V. Yakovlev, R.A. Talalaev, S.B. Thapa, and F. Scholz, "Growth conditions and surface morphology of AlN MOVPE", poster at *14th Int. Conf. on MOVPE* (ICMOVPE XIV), Metz, France, June 2008.

[28] T. Malinauskas, K. Jarasiunas, F. Scholz, and P. Brückner, "Diffusion and recombination of degenerate carrier plasma in GaN", poster at *5th International Workshop on Nitride semiconductors* (IWN2008), Montreux, Switzerland, Oct. 2008.

[29] S. Metzner, F. Bertram, T. Hempel, J. Christen, T. Wunderer, and F. Scholz, "Hochortsaufgelöste Kathodolumineszenzuntersuchungen an grün-emittierenden InGaN QWs auf $\{10\bar{1}1\}$-GaN-Facetten", *DGKK-Workshop III-V-Epitaxie*, Braunschweig, Germany, Dec. 2008.

[30] G.M. Prinz, I. Tischer, M. Schirra, M. Feneberg, S.B. Thapa, F. Scholz, Y. Taniyasu, M. Kasu, R. Sauer, and K. Thonke, "Optical investigation of doped and undoped AlN layers", *DPG-Tagung*, Berlin, Germany, Feb. 2008.

[31] I. Tischer, M. Schirra, M. Feneberg, G.M. Prinz, R. Sauer, K. Thonke, T. Wunderer, J. Hertkorn, F. Lipski, P. Brückner, F. Scholz, A. Chuvilin, U. Kaiser, I. Knoke, and E. Meissner, "Spatial distribution of structural defects in GaN", *DPG-Tagung*, Berlin, Germany, Feb. 2008.

Publications

[1] F. Demaria, S. Lorch, S. Menzel, M.C. Riedl, F. Rinaldi, R. Rösch, and P. Unger, "Design of highly-efficient high-power optically-pumped semiconductor disk lasers", in Proc. *21st IEEE Int.'l Semicond. Laser Conf.*, pp. 139–140. Sorrento, Italy, Sept. 2008.

[2] A. Gadallah, A. Kroner, I. Kardosh, F. Rinaldi, and R. Michalzik, "Oblong-shaped VCSELs with pre-defined mode patterns", in *Semiconductor Lasers and Laser Dynamics III*, K.P. Panayotov, M. Sciamanna, A.A. Valle, R. Michalzik (Eds.), Proc. SPIE 6997, pp. 69971R-1–9, 2008.

[3] J. Hertkorn, P. Brückner, C. Gao, F. Scholz, A. Chuvilin, U. Kaiser, U. Wurstbauer, and W. Wegscheider, "Transport properties in n-type AlGaN/AlN/GaN superlattices", *phys. stat. sol. (c)*, vol. 5, pp. 1950–1952, 2008.

[4] J. Hertkorn, F. Lipski, P. Brückner, T. Wunderer, S.B. Thapa, F. Scholz, A. Chuvilin, U. Kaiser, M. Beer, and J. Zweck, "Process optimization for the effective reduction of threading dislocations in MOVPE grown GaN using in situ deposited SiN_x masks", *J. Crystal Growth*, vol. 310, pp. 4867–4870, 2008.

[5] I. Kardosh, F. Demaria, F. Rinaldi, M.C. Riedl, and R. Michalzik, "Electrically pumped frequency-doubled surface emitting lasers operating at 485 nm emission wavelength", *Electron. Lett.*, vol. 44, pp. 524–525, 2008.

[6] I. Kardosh, F. Demaria, F. Rinaldi, S. Menzel, and R. Michalzik, "High-power single transverse mode vertical-cavity surface-emitting lasers with monolithically integrated curved dielectric mirrors", *IEEE Photon. Technol. Lett.*, vol. 20, pp. 2084–2086, 2008.

[7] A. Kroner, F. Rinaldi, R. Rösch, I. Kardosh, and R. Michalzik, "Towards a compact particle manipulation system based on arrays of vertical-cavity laser diodes", in Proc. *Nonlinear Microscopy and Optical Control, NMOC'2008*, p. 47. Münster, Germany, Feb. 2008.

[8] A. Kroner, F. Rinaldi, R. Rösch, and R. Michalzik, "Optical particle manipulation by application-specific densely packed VCSEL arrays", *Electron. Lett.*, vol. 44, pp. 353–354, 2008.

[9] A. Kroner, C. Schneck, F. Rinaldi, R. Rösch, and R. Michalzik, "Application of vertical-cavity laser-based optical tweezers for particle manipulation in microfluidic channels", in *Nanophotonics II*, D.L. Andrews, J.-M. Nunzi, A. Ostendorf (Eds.), Proc. SPIE 6988, pp. 69881R-1–12, 2008.

[10] A. Kroner, F. Rinaldi, R. Rösch, I. Kardosh, and R. Michalzik, "Ultra-miniaturized optical particle manipulation using densely integrated laser arrays", in Digest *1st Int.'l Sympos. on Optical Tweezers in Life Sciences*, poster 26, one page. Berlin, Germany, May 2008.

[11] R. Michalzik, J.M. Ostermann, and P. Debernardi, "Polarization-stable monolithic VCSELs" (invited), in *Vertical-Cavity Surface-Emitting Lasers XII*, C. Lei, J.K. Guenter (Eds.), Proc. SPIE 6908, pp. 69080A-1–16, 2008.

[12] S.B. Thapa, J. Hertkorn, T. Wunderer, F. Lipski, F. Scholz, A. Reiser, Y. Xie, M. Feneberg, K. Thonke, R. Sauer, M. Dürrschnabel, L.D. Yao, D. Gerthsen, H. Hochmuth, M. Lorenz, and M. Grundmann, "MOVPE growth of GaN around ZnO nanopillars", *J. Crystal Growth*, vol. 310, pp. 5139–5142, 2008.

[13] S.B. Thapa, J. Hertkorn, F. Scholz, G.M. Prinz, R.A.R. Leute, M. Feneberg, K. Thonke, R. Sauer, O. Klein, J. Biskupek, and U. Kaiser, "Growth and studies of Si-doped AlN layers", *J. Crystal Growth*, vol. 310, pp. 4939–4941, 2008.

[14] S.B. Thapa, J. Hertkorn, F. Scholz, G.M. Prinz, M. Feneberg, M. Schirra, K. Thonke, R. Sauer, J. Biskupek, and U. Kaiser, "MOVPE growth of high quality AlN layers and effects of Si doping", *phys. stat. sol. (c)*, vol. 5, pp. 1774–1776, 2008.

[15] T. Wunderer, F. Lipski, J. Hertkorn, P. Brückner, F. Scholz, M. Feneberg, M. Schirra, K. Thonke, A. Chuvilin, and U. Kaiser, "Bluish-green semipolar GaInN/GaN light emitting diodes on $\{1\bar{1}01\}$ GaN side facets", *phys. stat. sol. (c)*, vol. 5, pp. 2059–2062, 2008.

[16] T. Wunderer, J. Hertkorn, F. Lipski, P. Brückner, M. Feneberg, M. Schirra, K. Thonke, I. Knoke, E. Meissner, A. Chuvilin, U. Kaiser, and F. Scholz, "Optimization of semipolar GaInN/GaN blue/green light emitting diode structures on $\{1\bar{1}01\}$ GaN side facets", Gallium Nitride Materials and Devices III, H. Morkoc, C.W. Litton, J.-I. Chyi, Y. Nanishi, E. Yoon (Eds.), Proc. SPIE, vol. 6894, pp. 68940V-1–9, 2008.

[17] P.L. Bonanno, S.M. O'Malley, A.A. Sirenko, A. Kazimirov, Z.-H. Cai, T. Wunderer, P. Brückner, and F. Scholz, "Intrafacet migration effects in InGaN/GaN structures grown on triangular GaN ridges studied by submicron beam x-ray diffraction", *Appl. Phys. Lett.*, vol. 92, pp. 123106-1–3, 2008.

[18] P. Debernardi, A. Kroner, F. Rinaldi, and R. Michalzik, "Hot-cavity model for non-circular VCSELs", in Proc. *21st IEEE Int.'l Semicond. Laser Conf.*, pp. 91–92. Sorrento, Italy, Sept. 2008.

[19] P. Debernardi, J.M. Ostermann, and R. Michalzik, "VCSEL polarization control by monolithic surface gratings: a survey of modelling and experimental activities", in *Second International Conference on Advanced Optoelectronics and Lasers*, I.A. Sukhoivanov, V.A. Svich, Y.S. Shmaliy (Eds.), Proc. SPIE 7009, pp. 700903-1–10, 2008.

[20] M. Feneberg, F. Lipski, M. Schirra, R. Sauer, K. Thonke, T. Wunderer, P. Brückner, and F. Scholz, "High quantum efficiency of semipolar GaInN/GaN quantum wells", *phys. stat. sol. (c)*, vol. 5, pp. 2089–2091, 2008.

[21] S. Hövel, A. Bischoff, N.C. Gerhardt, M.R. Hofmann, T. Ackemann, A. Kroner, and R. Michalzik, "Optical spin manipulation of electrically pumped vertical-cavity surface-emitting lasers", *Appl. Phys. Lett.*, vol. 92, pp. 041118-1–3, 2008.

[22] O. Klein, J. Biskupek, U. Kaiser, S.B. Thapa, and F. Scholz, "Quantitative dislocation analysis of 2H AlN:Si grown on {0001} sapphire", in Proc. *14th European Microscopy Congress*, vol. 2: *Materials Science*, pp. 655–656, Springer, Berlin, 2008.

[23] M.V. Klymenko, I.M. Safonov, O.V. Shulika, I.A. Sukhoivanov, and R. Michalzik, "Effective-mass superlattice as an injector in quantum cascade lasers", *Opt. Quantum Electron.*, vol. 40, pp. 197–204, 2008.

[24] A.V. Lobanova, E.V. Yakovlev, R.A. Talalaev, S.B. Thapa, and F. Scholz, "Growth conditions and surface morphology of AlN MOVPE", *J. Crystal Growth*, vol. 310, pp. 4935–4938, 2008.

[25] S.M. O'Malley, P.L. Bonanno, T. Wunderer, P. Brückner, B. Neubert, F. Scholz, A. Kazimirov, and A.A. Sirenko, "X-ray diffraction studies of selective area grown InGaN/GaN multiple quantum wells on multi-facet GaN ridges", *phys. stat. sol. (c)*, vol. 5, pp. 1655–1658, 2008.

[26] G.M. Prinz, M. Feneberg, M. Schirra, R. Sauer, K. Thonke, S.B. Thapa, and F. Scholz, "Silicon doping induced strain of AlN layers: a comparative luminescence and Raman study, *phys. stat. sol. (RRL)*, vol. 2, pp. 215–217, 2008.

[27] B. Santic and F. Scholz, "On the evaluation of optical parameters of a thin semiconductor film from transmission spectra, and application to GaN films", *Meas. Sci. Technol.*, vol. 19, pp. 105303-1–7, 2008.

[28] B. Scherer, J. Wöllenstein, M. Weidemüller, W. Salzmann, J.M. Ostermann, F. Rinaldi, and R. Michalzik, "Measurement of the pressure broadening coefficients of the oxygen A-band using a low cost, polarization stabilized, widely tunable vertical-cavity surface-emitting laser", *Microsyst. Technol.*, vol. 14, pp. 607–614, 2008.

Ulm University | Institute of Optoelectronics | Annual Report 2008

ulm university universität ulm

Ulm University
Institute of Optoelectronics
Albert-Einstein-Allee 45
89081 Ulm | Germany